

# Control of Porphyrin Planarity and Aggregation by Covalent Capping: Bissilyloxy Porphyrin Silanes

Burhan A. Hussein, Zainab Shakeel, Andrew T. Turley, Aisha N. Bismillah, Kody Wolfstadt, Julia Pia, Melanie Pilkington, Paul R. McGonigal, **Marc Adler**

Submitted date: 24/04/2020 • Posted date: 27/04/2020

Licence: CC BY-NC-ND 4.0

Citation information: Hussein, Burhan A.; Shakeel, Zainab; Turley, Andrew T.; Bismillah, Aisha N.; Wolfstadt, Kody; Pia, Julia; et al. (2020): Control of Porphyrin Planarity and Aggregation by Covalent Capping: Bissilyloxy Porphyrin Silanes. ChemRxiv. Preprint. <https://doi.org/10.26434/chemrxiv.12195084.v1>

Porphyrins are cornerstone functional materials that are useful in a wide variety of settings ranging from molecular electronics to biology and medicine. Their applications are often hindered, however, by poor solubilities that result from their extended, solvophobic aromatic surfaces. Attempts to counteract this problem by functionalizing their peripheries have been met with only limited success. Here, we demonstrate a versatile strategy to tune the physical and electronic properties of porphyrins using an axial functionalization approach. Porphyrin silanes (PorSils) and bissilyloxy PorSils (SOPS) are prepared from porphyrins by operationally simple  $\kappa^4\text{N}$ -silylation protocols, introducing bulky silyloxy “caps” that are central and perpendicular to the planar porphyrin. While porphyrins typically form either J- or H-aggregates, SOPS do not self-associate in the same manner: the silyloxy axial substituents dramatically improve solubility by inhibiting aggregation. Moreover, axial porphyrin functionalization offers convenient handles through which optical, electronic, and structural properties of the porphyrin core can be modulated. We observe that the identity of the silyloxy substituent impacts the degree of planarity of the porphyrin in the solid state as well as the redox potentials.

## File list (2)

PorSil paper final.pdf (2.97 MiB)

[view on ChemRxiv](#) • [download file](#)

PorSil SI final.pdf (18.18 MiB)

[view on ChemRxiv](#) • [download file](#)

# Control of Porphyrin Planarity and Aggregation by Covalent Capping: Bissilyloxy Porphyrin Silanes

Burhan A. Hussein,<sup>†,‡</sup> Zainab Shakeel,<sup>†</sup> Andrew T. Turley,<sup>‡</sup> Aisha N. Bismillah,<sup>‡,§</sup> Kody M. Wolfstadt,<sup>†</sup> Julia E. Pia,<sup>†</sup> Melanie Pilkington,<sup>‡</sup> Paul R. McGonigal,<sup>‡</sup> and Marc J. Adler<sup>†,\*</sup>

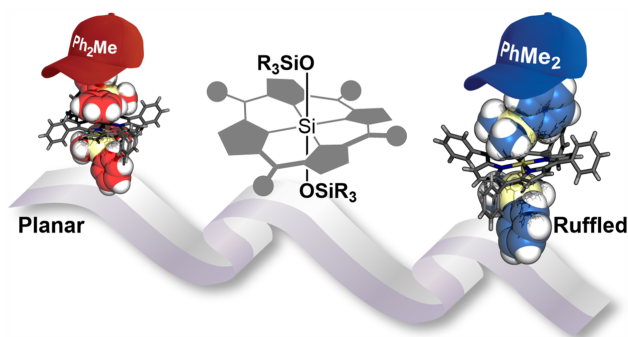
<sup>†</sup> Department of Chemistry & Biology, Ryerson University, 350 Victoria St., Toronto, ON, M5B 2K3, Canada

<sup>‡</sup> Department of Chemistry, Durham University, Lower Mountjoy, Stockton Road, Durham, DH1 3LE, United Kingdom

<sup>§</sup> Department of Chemistry, Dartmouth College, Hanover, New Hampshire, 03755, USA

<sup>‡</sup> Department of Chemistry, Brock University, 1812 Sir Isaac Brock Way, St. Catharines, ON, L2S 3A1, Canada

*Supporting Information Placeholder*



**ABSTRACT:** Porphyrins are cornerstone functional materials that are useful in a wide variety of settings ranging from molecular electronics to biology and medicine. Their applications are often hindered, however, by poor solubilities that result from their extended, solvophobic aromatic surfaces. Attempts to counteract this problem by functionalizing their peripheries have been met with only limited success. Here, we demonstrate a versatile strategy to tune the physical and electronic properties of porphyrins using an axial functionalization approach. Porphyrin silanes (PorSils) and bissilyloxy PorSils (SOPS) are prepared from porphyrins by operationally simple  $\kappa^4N$ -silylation protocols, introducing bulky silyloxy “caps” that are central and perpendicular to the planar porphyrin. While porphyrins typically form either J- or H-aggregates, SOPS do not self-associate in the same manner: the silyloxy axial substituents dramatically improve solubility by inhibiting aggregation. Moreover, axial porphyrin functionalization offers convenient handles through which optical, electronic, and structural properties of the porphyrin core can be modulated. We observe that the identity of the silyloxy substituent impacts the degree of planarity of the porphyrin in the solid state as well as the redox potentials.

## INTRODUCTION

Porphyrins are a long-known and well-studied class of compounds.<sup>1</sup> Naturally occurring variants are vital for the biochemistry of both plants (e.g. chlorophyll, a photoredox catalyst for photosynthesis) and animals (e.g. heme, an oxygen carrier).<sup>2</sup> Accordingly, significant efforts have been dedicated to establishing laboratory syntheses of this class of compounds.<sup>3</sup> Both porphyrins and  $\kappa^4N,N',N'',N'''$ -porphyrin–metal complexes (i.e. metalloporphyrins)<sup>4</sup> possess optical, electronic, and chemical properties that make them useful in a range of applied fields, including photodynamic therapy,<sup>5,6</sup> biological imaging,<sup>7</sup> organic photovoltaics,<sup>8</sup> photoredox catalysis,<sup>9</sup> and analytical chemistry.<sup>10</sup> However, their applications can be hindered by their suboptimal physical properties. A constraining drawback of working with porphyrins is that they are difficult to handle and process owing to their poor solubilities, which can be ascribed to the favorable J- or H-aggregation of their exposed aromatic surfaces.<sup>11</sup> Efforts have been made to prepare derivatives that exhibit improved solubilities in aqueous<sup>12</sup> and organic<sup>13</sup> solutions. Inhibition of aggregation has generally been

accomplished through peripheral functionalization of the porphyrin with i) hydrophilic or non-conjugated lipophilic groups to interact favorably with the solvent medium and/or ii) bulky groups that sterically disfavor intermolecular association. In nature, porphyrins are buried in biomolecular hydrophobic clefts which circumvents the solubility obstacle; synthetic systems mimicking this approach have recently been explored to improve photophysical and electrochemical performance.<sup>14</sup>

Phthalocyanines (Pcs)<sup>15</sup> have been used for many of the same applications as porphyrin compounds.<sup>16</sup> Like porphyrins, Pcs are planar and suffer from poor solubilities. However, an elegant approach to improve their physical properties has been to silylate the center of the Pc, introducing axially oriented groups that shield the aromatic surface. Beyond its effect on solubility, silylation modifies the optical and electronic profiles of Pcs, which has led to over 1000 papers discussing the synthesis, properties, and applications of silylated Pcs (Si-Pcs).<sup>17</sup> Curiously, however, there is a relative dearth of literature describing such functionalization of the parent porphyrin compounds, which is presumably due to the relatively harsh conditions and operationally complex protocols used to incorporate the central silicon atom. While Si-Pcs are formed in the presence of  $\text{SiCl}_4$

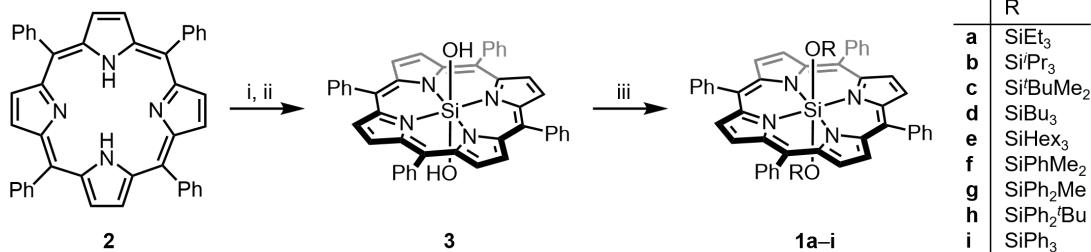
to i) template the macrocyclization and ii) silylate in situ, porphyrin silanes (PorSils) have been synthesized by first making the porphyrin and then inserting the silicon by forming the [porphyrin]<sup>2-</sup> species with a strong and difficult-to-handle amide base under strictly anhydrous conditions.<sup>18,19</sup> Sun and co-workers were able to silylate two porphyrins using HSiCl<sub>3</sub> and a tertiary amine base. However, purification of the resulting PorSil dichloride requires chromatography on neutral alumina,<sup>20</sup> which makes the protocol too inefficient and expensive to be applied as a general method on a large scale. Furthermore, this protocol can be difficult to reproduce as the PorSil dichloride can react with the alumina sorbent via nucleophilic substitution of a chloride.

This lack of development of PorSils is unfortunate given that peripheral ring functionalization – allowing for useful tuning of the electronic properties – is much easier to achieve for PorSils than for Si-Pcs. There have been relatively few reports of peripherally functionalized Si-Pcs.<sup>21</sup> The substituted pyrroles and phthalic acids required as starting materials are synthetically challenging and scarcely commercially available. Porphyrins, on the other hand, possess bridging methines connecting their pyrrole rings that serve as convenient handles for *meso* substitution. This *meso* substitution is readily achieved by simply forming the porphyrin from commercially available aldehydes, of which there are many. Therefore, a robust procedure for  $\kappa^4N$ -silylation of porphyrin derivatives is an appealing target that would provide access to PorSil materials that combine the electronic tuneability of porphyrins with the improved physical properties of Si-Pcs.

Here, we describe a straightforward and general synthetic approach to PorSils (Scheme 1), which has allowed us to elaborate them into a new class of porphyrins, bissilyloxy PorSils (SOPS). Investigation of this series of SOPS (**1a-i**) based on 5,10,15,20-tetraphenylporphyrin (TPP, **2**) revealed that the axial substituents not only serve to solubilize the porphyrin but also to tune their optical and electronic properties.

## RESULTS AND DISCUSSION

**Synthesis and Reactivity of PorSils and SOPS.** Tetraphenylporphyrin (TPP, **2**) was synthesized by the Adler–Longo method.<sup>3b</sup> Previous methodology for accessing PorSils relied on the use of a highly reactive lithium amide to deprotonate the porphyrin prior to reaction with HSiCl<sub>3</sub>, which was found to be a better porphyrin silylating reagent than the perhaps more intuitive building block SiCl<sub>4</sub>.<sup>18</sup> Sun and co-workers found that porphyrin silylation could be accomplished by combining the porphyrin and HSiCl<sub>3</sub> in the presence of Pr<sub>3</sub>N.<sup>20</sup> They relied on chromatography to purify the resulting TPP-Si(Cl)<sub>2</sub> (**2-SiCl<sub>2</sub>**), an inefficient approach that also notably did not work in our **Scheme 1. Synthesis of the target library of bissilyloxy porphyrin silanes (SOPS).**



Reagents and conditions: i. HSiCl<sub>3</sub>, Et<sub>3</sub>N, rt, 24 h, 85%; ii. tetrahydrofuran, water, reflux, 2 h, quantitative; iii. chlorosilane (RCl), Et<sub>3</sub>N, 1,2-dichloroethane, reflux, 16 h, 82–97%.

hands as the modified porphyrin covalently reacted with the solid support. We accomplished the silylation of **2** using HSiCl<sub>3</sub> with Et<sub>3</sub>N, a common laboratory reagent (Scheme 1). After aqueous workup, residual Et<sub>3</sub>N can be readily removed by evaporation. Using this method we were able to avoid the necessity for chromatography, and instead were able to isolate our desired product by simple liquid-liquid extraction, resulting in up to an 85% yield of **2-SiCl<sub>2</sub>**. The generalization of this reaction in combination with the simplification of the purification procedure are steps forward for the prospects of developing this class of molecules. To synthesize the SOPS, **2-SiCl<sub>2</sub>** was converted quantitatively to **3** by refluxing in a THF/water mixture, and subsequently silylated using Et<sub>3</sub>N and the respective silyl chloride (Scheme 1). These final compounds were air-stable and purified by column chromatography using silica gel and alkaline eluents (see Supporting Information); large scale purification could be accomplished by recrystallization.

It is worth commenting on the more practical aspects of this synthesis, particularly in reference to key intermediate **2-SiCl<sub>2</sub>**. While stable in open air and during neutral aqueous workup, the Si-Cl bonds in the PorSil are labile enough that reaction quickly and quantitatively occurs between **2-Si(Cl)<sub>2</sub>** and silica gel (in both column and thin-layer chromatography (TLC)). Neither the precursor (**2**) nor subsequent product (**3**) display such reactivity. This allows for facile tracking of reaction progress in either the generation of **2-SiCl<sub>2</sub>** from **2** or consumption of **2-SiCl<sub>2</sub>** to make **3**, as **2-SiCl<sub>2</sub>** is completely immobile on a silica TLC plate.<sup>22</sup>

**NMR Analysis.** The NMR spectra of the synthesized SOPS provide insight into the structural and electronic characteristics of these molecules (Figure 1). The quadrupole of the aromatic porphyrin shields the alkyl/aryl protons of the silyloxy axial substituents resulting in marked upfield shifts of these signals. This was not unexpected: N-H protons in **2** – which also lie in the shielded porphyrin core – are observed at -2.75 ppm and similar upfield shifts are observed for axial substituents in related PorSils and SiPcs.<sup>23</sup> This shielding falls off with distance from the silane (and thus the center of the quadrupole); for example, in TPP-Si(OSiPh<sub>3</sub>)<sub>2</sub> (**1i**), the signal for the *ortho* protons (H<sub>E</sub>) is visible at 4.69 ppm, significantly upfield from the usual aromatic region, and the signal for the *meta* protons (H<sub>F</sub>) is observed at 6.57 ppm (Figure 1). An additional consequence is that while phenylsilanes typically have overlapping signals for the *meta* (H<sub>F</sub>) and *para* (H<sub>G</sub>) protons, such protons in these compounds (i.e. **1f-i**) are completely resolved, with  $\Delta\delta$  of 0.26-0.32 ppm. A similar effect is observed in the <sup>13</sup>C NMR spectra, with significant upfield shifts observed for the axial silane substituents (see Supporting Information, Figures S1-18).

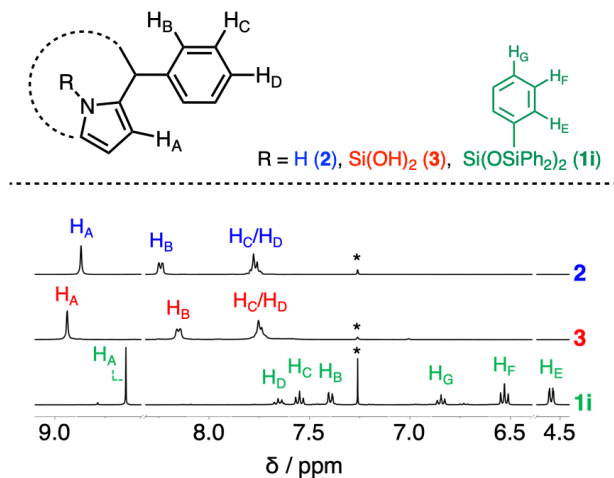


**Figure 1.** Partial  $^1\text{H}$  NMR spectra (400 MHz,  $\text{CDCl}_3$ , 298 K) of **2**, **3**, and **1i** showing i) that aromatic resonances of the axial substituent are shifted upfield by their proximity to the porphyrin ring and ii) that  $\text{H}_B$  is shifted significantly upfield in aromatic SOPS (**1i**). \*Signal from residual  $\text{CHCl}_3$  in  $\text{CDCl}_3$ .

While the proton resonance for  $\text{H}_B$  appears at approximately 8.1–8.2 ppm (Figure 1) in the spectra of **2** and alkyl capped derivatives **1a–e**, it is shifted upfield to 7.4–8.0 ppm for **1f–i**. We attribute this effect to through-space interactions between  $\text{H}_B$  and the aromatic ring(s) of the capping groups in **1f–i**; such interactions are also observed in the solid state (see Supporting Information, Figures S49–53). All NMR spectra acquired at ambient temperature were well-resolved; this evidence of rapid conformational sampling suggests that these intramolecular contacts do not restrict bond rotation. There is, however, a distinct broadening of the aromatic peaks of the silyloxy cap in **1f** at low temperatures, indicating anisotropy due to slow conformational sampling. We were unable to reach a temperature low enough to sufficiently slow the rate of interconversion such that two distinct species could be detected (see Supporting Information, Figure S19).

**Impact of Axial Substitution on Porphyrin Planarity.** PorSils have previously been observed to have distortion in the planarity of the ring system in the solid state, which is due to the small size of silicon relative to the porphyrin cavity size.<sup>24</sup> In these instances, the porphyrin core slightly contracts to allow for sufficient orbital overlap between the pyrrole nitrogen atoms and the electron-deficient silicon atom. These non-planar porphyrins<sup>25</sup> can adopt a variety of conformations, including ruffled and waved,<sup>26</sup> which each have characteristic patterns of displacement. Of the 10 previously reported porphyrin silane crystal structures, four were close to planar ( $\Delta r < 0.15 \text{ \AA}$ : TPP-Si(OH)<sub>2</sub><sup>27</sup> TPP-Si(CH<sub>2</sub>TMS)<sub>2</sub>, TPP-Si(CHCH<sub>2</sub>)<sub>2</sub>, and TPP-Si(CCPH)<sub>2</sub><sup>28</sup>) and six were clearly non-planar ( $\Delta r > 0.15 \text{ \AA}$ : [TPP-Si(THF)<sub>2</sub>]<sup>2+</sup>•2Cl<sup>-</sup>,<sup>29</sup> TPP-SiOTf<sub>2</sub>,<sup>18</sup> TPP-SiMePh,<sup>30</sup> TPP-SiPh<sub>2</sub>,<sup>28</sup> tetrakis(*p*-tolyl)porphyrin-SiF<sub>2</sub>, and tetrakis(*p*-trifluoromethylphenyl)porphyrin-SiF<sub>2</sub><sup>31</sup>).

From this set it seems as though planarity can be achieved if both i) the axial substituents are sufficiently small so as to not about the porphyrin and ii) the axial ligand is capable of  $\pi$ -back-bonding to provide the silicon with extra electron density and allow Si–N bonds to lengthen to planarity. For example, while a fluorine atom is certainly small, it does not effectively provide electron density to the silicon via unshared electrons. On the other hand, the phenyl substituents can more readily  $\pi$ -back-bond to the silicon, however the *ortho* hydrogens have a deleterious steric interaction with the macrocyclic ring, preventing porphyrin planarization. This theory is also supported by the observed Si–N and Si–X (X = first atom of axial substituent) bond lengths: planar PorSils feature longer Si–N bonds compared to non-planar structures and the Si–X bond lengths are similar to those in tetra-coordinate silanes as opposed to the elongated bonds expected in a hexa-coordinate silane.<sup>32</sup>

To systematically probe the impact of axial substitution on solid-state conformation of the PorSils, single crystals of the four species that possessed aromatic silyl caps **1f–i** were analyzed by X-ray diffraction. This data confirmed the presumed structures in all cases: in each of the four structures the hyper-coordinate silicon core adopts an octahedral structure with the two silyloxy ligands observed in a *trans* (diaxial) arrangement (Figure 2).

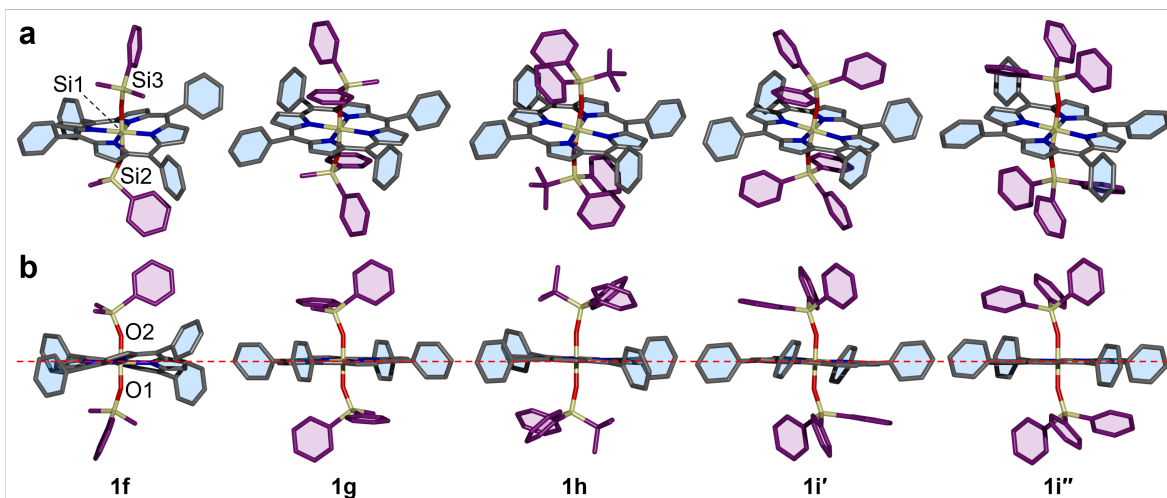


**Figure 2.** a) X-ray crystal structures of SOPS **1f–1i** confirm the presence and structure of capping groups on either face of the porphyrin units. Both independent molecules in the unit cell of **1i** are shown. b) Near-linear Si1–O–Si linkages (bond angles 150–168°) connect the bulky silyloxy caps to the PorSil. The porphyrin system of **1f** is ruffled while **1i** is slightly bent. Nitrogen atoms are shown in blue, silicon atoms in yellow, oxygen atoms in red, and carbon atoms in gray and purple. Hydrogen atoms are omitted for clarity.

**Table 1. Selected data from crystal structures of SOPS 1f-i.**

Compound	Si1-O bond lengths <sup>a</sup> (Å)	Si1-O-Si bond angles <sup>a</sup> (°)	$\Delta r^b$ (Å)	Displacement of individual <i>meso</i> carbons from N1-Si1-N2 plane <sup>a,b</sup> (Å)	
TPP-Si(OSiMe <sub>2</sub> Ph) <sub>2</sub> ( <b>1f</b> )	1.688(2) (Si1-O1)	150.8(2) (Si1-O1-Si2)	0.469	-0.431 (C5), +0.507 (C16), -0.549 (C27), +0.389 (C38)	
	1.681(2) (Si1-O2)	155.2(2) (Si1-O2-Si3)			
TPP-Si(OSiMePh <sub>2</sub> ) <sub>2</sub> ( <b>1g</b> )	1.6758(14)	157.75(10)	0.006	0 (C5), +0.011 (C16), 0 (C5), -0.011 (C16)	
TPP-Si(OSiPh <sub>2</sub> Bu) <sub>2</sub> ( <b>1h</b> )	1.6801(12)	167.57(9)	0.111	-0.152 (C5), -0.069 (C16), +0.152, (C5), +0.069 (C16)	
TPP-Si(OSiPh <sub>3</sub> ) <sub>2</sub> ( <b>1i</b> )	Pose 1 <sup>c</sup> ( <b>1i'</b> )	1.684(3)	163.9(2)	0.058	-0.006 (C5), -0.109 (C16), +0.006 (C5), +0.109 (C16)
	Pose 2 <sup>c</sup> ( <b>1i''</b> )	1.690(3)	159.8(2)	0.085	-0.025 (C45), -0.145 (C56), +0.025 (C45), +0.145 (C56)

<sup>a</sup> Atoms labeled according to designation in the crystal structure: Si1 is the central silicon atom; Si2 and Si3 are the silicon atoms in the silyloxy caps; O1 and O2 are the linking oxygens of the bisilyl ethers. N1 and N2 refer to two *cis*-coordinated nitrogens. For full numbering scheme see Supporting Information, Figures S41, 43, 45, and 47. <sup>b</sup> See reference 25; (+) and (-) designations represent relative orientation. <sup>c</sup> The asymmetric unit in **1i** contains two molecules, each in a different conformational pose (**1i'** and **1i''**).

Of the four compounds we examined (seen in Table 1), all deviated from planarity. Compound **1g** is the most planar molecule with two *meso* carbon atoms located *trans* to each other displaced above and below the plane by  $\pm 0.011$  Å. This is the most planar porphyrin silane crystal structure reported to date. The *meso* carbons in **1h** and in both poses of **1i** were each out of plane, though only slightly ( $\leq 0.152$  Å), and porphyrins maintained overall symmetry around the central silicon. Unique amongst the studied set, compound **1f** displayed the least planar structure and was surprisingly devoid of symmetry around the central silicon atom. In general, we were gratified to see that modification of the easily incorporated axial silyloxy substituents can control the degree to which the porphyrin deviates from planarity in the crystal structure. This demonstrates that axial substitution is a powerful tool for control of solid-state porphyrin conformation.

In terms of electronics, the iterative replacement of methyl for phenyl groups on the silyloxy cap (**1f** to **1g** to **1i**) should increase the electron density on the silane allowing for lengthening of the O1-Si2/O2-Si3 bond (Figure 2); the excess electron density on the oxygen could translate to a shorter Si1-O distances and allow the Si-N bonds to lengthen to accommodate the preferred return to planarity of the ring. No such effect is observed. From a steric perspective, the Si1-O-Si bond angle of the least planar porphyrin (**1f**) is the most acute so one might think the steric interaction is influencing ring structure, however i) this is also the smallest of the studied substituents and arranged in the sterically least impacting way in the solid state (with the phenyl pointing away from the porphyrin) and ii) there is no general correlation between that bond angle and planarity in the studied compounds.

There does appear to be a correlation between axial silyloxy substituent size and Si1-O-Si angle, tending towards linear as the cap size increases in this set. The SOPS bearing the largest substituent (OSi<sup>t</sup>BuPh<sub>2</sub>, **1h**) displays a remarkably wide bond angle of 168°. The Si1-O bond length also varies based on the silyl cap, though no clear trend is observed. While shorter Si1-O bond distances would be expected in the more planar SOPS, there is a complex interplay amongst these derivatives with respect to the steric and electronic demands of the silyloxy cap substituents. From this perspective the Me<sub>2</sub>Ph derivative (**1f**) is

unique amongst PorSils that have been examined by X-ray crystallography: it has an Si-X bond distance similar to that of a tetracoordinate silane, yet the porphyrin in the crystal structure is still highly ruffled. The other derivatives seem to fit into the construct derived from previous studies of porphyrin silanes (as discussed above).

One last interesting note is that while the silyloxy substituents in **1g**, **1h**, and **1i** are arranged in an *anti* configuration with respect to the Si-O(-Si1)-O-Si bond, the highly ruffled **1f** has a Si-O(-Si1)-O-Si dihedral angle of 86.72°. This may be a consequence of the unique conformation of this PorSil, or it could be that the packing in the crystal lattice impacts this arrangement.

**Influence of Axial Substitution on Solubility.** Owing to their large, three-dimensional hydrophobic surfaces, SOPS (**1a-i**) have much greater solubility in organic solvents than TPP (**2**), as seen in Table 2. There were also noticeable differences in solubility between the series of aliphatic SOPS and the series **Table 2. Solubility of TPP (2), aliphatic SOPS (1e), and aromatic SOPS (1h).**

Solvent	Limiting concentration <sup>a</sup> (mM)		
	<b>2</b>	<b>1e</b>	<b>1h</b>
Hexanes	0.0 <sup>b</sup>	8.0	1.7
Toluene	2.5	7.3	4.4
Dichloromethane	4.7	13	6.5
Ethyl acetate	0.41	6.7	1.2
Acetonitrile	0.20	0.05	0.05
Ethanol	0.11	0.70	0.28

<sup>a</sup> Limiting concentration determined by titrating 0.1 mL aliquots of solvent into samples of the porphyrins (5-15 mg) followed by sonication until full dissolution. <sup>b</sup> No dissolution observed up to 10 mg in 15 mL.

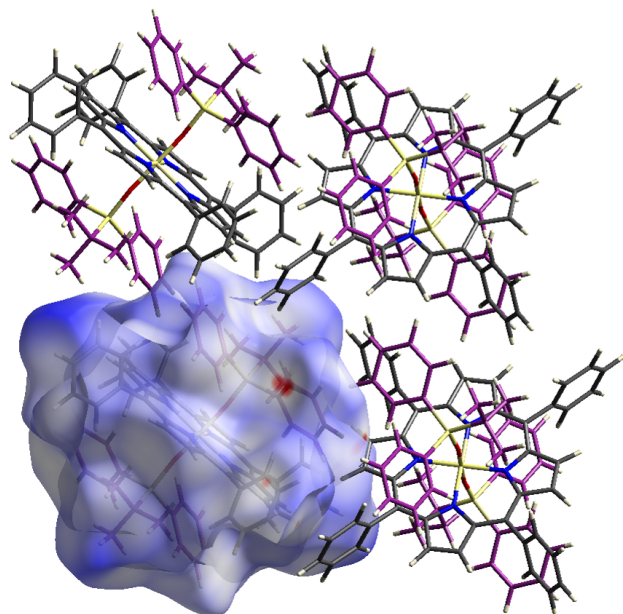


**Figure 3.** The solid-state superstructure of **1h**, which shows that the silyloxy cap shields the porphyrin core from intermolecular aromatic interactions. A Hirshfeld surface plot reveals that the interatomic distances between neighboring molecules are almost entirely at (white) or above (blue) the sum of the van der Waals radii. (Close contacts shown in red.)

of aromatic SOPS; these differences were used to our advantage in the purification process (see Supporting Information). The improved solubilities of the SOPS compared to **2** can be rationalized by considering the non-covalent interactions between the molecules in the solid state. Porphyrins that lack axial capping groups, such as **2**, are known to experience favorable face-to-face aromatic interactions between their large, exposed  $\pi$ -surfaces. These interactions cause aggregation, which in turn can red-shift absorption and quench fluorescence. On the other hand, analysis of the packing structures of **1f-i** (see Supporting Information, Figures S42, 44, 46, and 48) shows that the bulky axial caps prevent this interaction. As an illustrative example, there are three molecules near the axial cap of **1h** (Figure 3), but

**Table 3. Physicochemical data of studied porphyrins.**

Compound	Absorption <sup>a</sup> $\lambda_{\max}$ [nm]					Emission $\lambda_{\max}$ [nm] ( $\lambda_{\text{ex}}$ [nm])	$E_{1/2}$ <sup>b</sup> [V vs. NHE]	
	Soret	Q <sub>1</sub>	Q <sub>2</sub>	Q <sub>3</sub>	Q <sub>4</sub>		Oxidation	Reduction
<b>1a</b>	421	513	552	589	625	605, 643 (430)	1.33	- 1.06
<b>1b</b>	422	512	550	591	623	592, 627 (430)	1.36	- 1.21
<b>1c</b>	418	512	549	586	618	605, 646 (427)	1.34	- 1.08
<b>1d</b>	424	514	555	596	627	598, 645 (424)	1.32	- 1.18
<b>1e</b>	423	514	555	595	627	602, 649 (423)	1.32	- 1.35
<b>1f</b>	423	514	552	591	628	605, 649 (427)	1.35	- 1.10
<b>1g</b>	422	514	553	592	628	600, 648 (423)	1.36	- 1.08
<b>1h</b>	423	512	550	587	628	607, 648 (431)	1.35	- 1.11
<b>1i</b>	425	515	553	592	633	602, 645 (427)	1.33	- 1.13
<b>2</b>	417	514	549	590	646	650, 711 (418)	1.34 <sup>c</sup>	- 0.92
<b>3</b>	418, 446	514	550	590	649	600, 650, 711 (418)	1.52	- 0.93

<sup>a</sup> Low energy visible transitions from UV-Vis in dichloromethane. <sup>b</sup> Data collected using 0.1 M NBu<sub>4</sub>PF<sub>6</sub> dichloromethane solutions at 100 mV s<sup>-1</sup> and referenced to a ferrocene ([Fc]/[Fc]<sup>+</sup>) internal standard followed by conversion to NHE; [Fc]/[Fc]<sup>+</sup> = +765 mV vs. NHE in dichloromethane. <sup>c</sup> A second oxidation peak was observed for **2** at 1.63 V vs. NHE.

none come into close contact with the surface of the porphyrin ring system itself; they contact the cap instead. A Hirshfeld surface plot<sup>33</sup> of **1h** (Figure 3) and interaction energy calculations (see Supporting Information, Tables S3-12 and Figures S56-70) confirm that these interactions between the neighboring molecules are dominated by van der Waals forces. The SOPS contact one another at distances that correspond closely to the sum of the respective van der Waals radii, as can be seen by the large areas of white in the Hirshfeld surface.

**Impact of Axial Substitution on Optoelectronic Properties.** As expected, all the investigated porphyrins are UV-active compounds (Table 3, Figures 4 and 5a). Silylation of TPP (**2**) to make TPP-Si(OH)<sub>2</sub> (**3**) does not significantly impact observed  $\lambda_{\max}$  – though there is a small general red-shift – and a J-aggregation-type Soret band is observed around 450 nm. Q<sub>1</sub> is the strongest Q-band of both **2** and **3**, indicating that the dissymmetry that exists in **2** giving rise to this optical phenomenon is also present in **3**. This spectral feature lies in stark contrast to what is typically seen in two-dimensional metallated (i.e. Zn(II), Ni(II), Cu(II), and Fe(II)) porphyrins, which have only one or two Q-bands (with Q<sub>2</sub> and/or Q<sub>3</sub> persisting) due to higher levels of symmetry.<sup>34</sup> Interestingly, when the silyloxy caps are installed we observe Q-band structures more like the metallated porphyrins, with Q<sub>2</sub> being the most intense (Figure 4). There is some differentiation amongst the relative molar extinction coefficients of the Q bands for SOPS; for example, **1a** has almost no Q<sub>4</sub> band, while **1b** has a Q<sub>4</sub> band that is greater in intensity than Q<sub>1</sub>. Notably, in all SOPS some degree of dissymmetry is evidenced by the presence of all four Q bands, and the respective  $\lambda_{\max}$  (Soret and Q bands) of the SOPS are generally red-shifted compared to that of **2**, with the notable exception of Q<sub>4</sub> (Table 3). Both of these observations can be attributed to the likely ruffling of the porphyrin in solution.<sup>35</sup> This hypothesis supported by a density functional theory structural study (M06-2X/6-31G with a polarizable continuum model for dichloromethane solvent) that shows non-planarity in the calculated ground state minimized structure of SOPS in solution (see Supporting Information, Figures S54 and 55). Variance amongst the SOPS  $\lambda_{\max}$  (Soret and Q bands) is modest (Table 3); the largest range can be seen in Q<sub>4</sub>, where the lowest (TPP-Si(OSi<sup>*i*</sup>BuMe<sub>2</sub>)<sub>2</sub>, **1c**) and highest (TPP-Si(OSiPh<sub>3</sub>)<sub>2</sub>, **1i**)  $\lambda_{\max}$  are

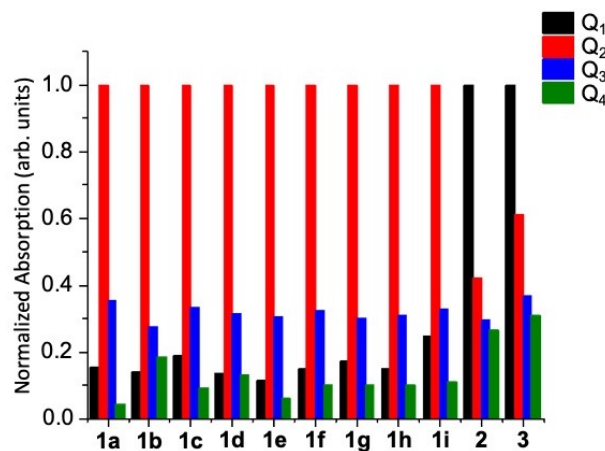


**Figure 4.** Comparison of normalized absorption for **1a-i**, **2**, and **3**.

separated by 15 nm (618 and 633 nm, respectively). This absorption data demonstrates that the selection of a particular silyloxy cap can be used to control the structure of the porphyrin ring.

The examined porphyrins were fluorescent in a dichloromethane solution (Table 3 and Figure 5b). For **2** we observed a very strong emission band at 650 nm and a much smaller emission at 711 nm. This two-emission profile is typical of porphyrins, and is attributed to two tautomeric states.<sup>36</sup> In toluene, **2** has the same  $\lambda_{\text{max}}$  as in dichloromethane but emits relatively more intensely at 711 nm.<sup>37</sup> This demonstrates that environmental effects (i.e. solvent) impact the population distribution of the two tautomers but not the energy of the individual HOMO-LUMO gaps. When the SOPS (**1a-i**) were excited at their respective Soret bands in solution, two emission signals were noted: one around 600 nm and another closer to 650 nm (Table 3 and Figure 6b). The ~50 nm blue shift of the SOPS with respect to **2** corresponds to what is seen in fluorescent metalloporphyrins such as TPP-Zn.<sup>38</sup> Interestingly, **3** fluoresces at three distinct  $\lambda_{\text{max}}$ : 600, 650, and 711 nm. This finding suggests that compound **3** either i) possesses optical character similar to both free base and metalloporphyrin and/or ii) has an additional red-shifted emission due to aggregation. The population distribution between the emission bands at ~600 and ~650 nm differs from that seen in the SOPS. It is clear that the silyloxy cap is impacting ring electronics, perhaps as a consequence of inhibition of aggregation and/or influence on porphyrin planarity.

Samples of **2**, aliphatic SOPS **1d**, and aromatic SOPS **1i** were also embedded into a ZEONEX polymer matrix and examined by fluorescence (Figure 5b). The emission spectrum of **2** was significantly red-shifted in the ZEONEX film. Given that general environmental effects do not cause such a phenomenon in **2**, this appears to be evidence of aggregation of the porphyrin in the polymer.<sup>39</sup> While the SOPS did show an altered population distribution of the two tautomeric states, as evidenced by a change in relative intensities of the two emission bands, the energies of these transitions, however, were not affected. These findings support our hypothesis that silyloxy caps discourage aggregation.

The electrochemical behavior of these compounds was studied using cyclic voltammetry (CV) for the full range of synthesized SOPS (Table 3; for CV spectra see Supporting Information, Figures S35-40). All SOPS underwent a reversible one-electron oxidation with similar oxidizing potentials regardless

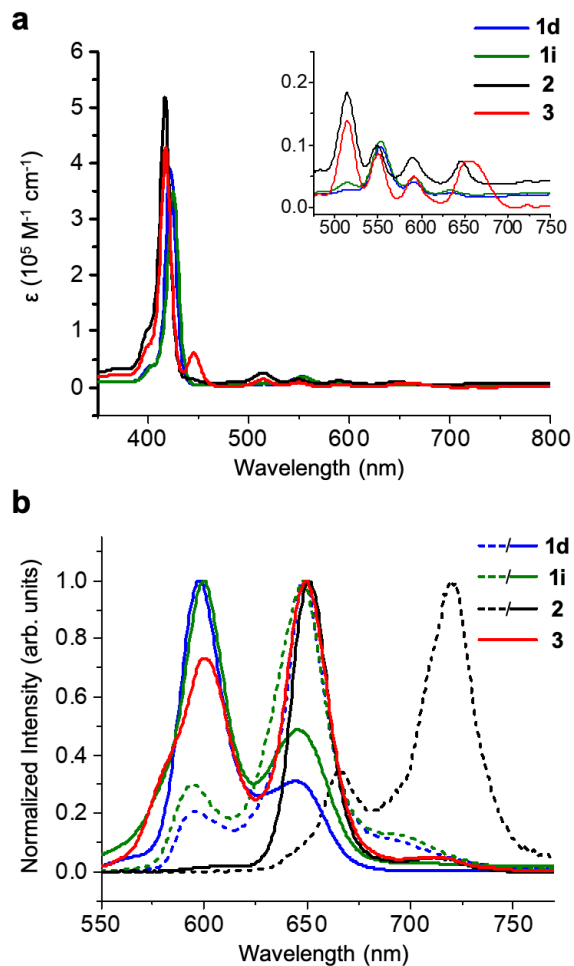


**Figure 5.** Absorption and emission spectra of a representative set of porphyrins in dichloromethane: **1d** (aliphatic SOPS), **1i** (aromatic SOPS), **2**, and **3**. a) Absorption spectra of porphyrins, with inset zoom on Q bands. b) Normalized emission profiles of porphyrins in i) dichloromethane (10  $\mu\text{M}$ , solid lines) and ii) dispersed in optically clear amorphous polymer films (0.1 wt.% ZEONEX film, dotted lines).

of the identity of the silyloxy cap. However, the SOPS have slightly higher oxidation potentials (1.31-1.35 V) that those observed for **2** (1.31 V), and significantly lower than that observed for **3** (1.52 V). This increase in the oxidation potential indicates a stabilization of the HOMO of the PorSils in solution.

There was more variance in the reduction potential of the SOPS, with values ranging from -1.35 V (**1e**) to -1.06 V (**1a**). In all cases the SOPS were reduced at potential greater than either **2** or **3**, which we observed as -0.92 and -0.93 V, respectively. A small trend was observed for the  $C_3$ -symmetrical linear trialkylsilyloxy caps (**1a**, **1d**, and **1e**), with longer chain lengths being associated with reduction potentials of greater magnitude; this could be due to electron repulsion by the silyloxy substituents. No other obvious trends were observed, however it is clear that the LUMO energies of the SOPS are sensitive to the identity of the silyloxy cap.

## CONCLUSIONS AND OUTLOOK

Edge-functionalized porphyrin derivatives are reliable and widely used building blocks for functional organic materials. We have demonstrated that the straightforward, high-yielding modification of porphyrins at their core is a viable alternative

way to tune their properties. By silylating the porphyrin and capping with axial silyloxy substituents, we have increased porphyrin solubility and prevented aggregation-induced physicochemical phenomena. The identity of the silyloxy cap can be used to tune porphyrin planarity and molecular orbital energies. This approach offers opportunities for the customization of porphyrins through axial tuning and an improvement in the processability of porphyrins via increased solubility.

## ASSOCIATED CONTENT

### Supporting Information

The Supporting Information is available free of charge on the ACS Publications website.

Experimental and synthetic details;  $^1\text{H}$ ,  $^{13}\text{C}$ , and VT-NMR spectra; UV-Vis, fluorescence, and CV spectra; X-ray crystallographic data and Hirshfeld analysis; DFT structural studies; Hirshfeld surfaces brief description; mass spectra (PDF)

## AUTHOR INFORMATION

### Corresponding Author

\* marcjadler@ryerson.ca

### Author Contributions

The manuscript was written through contributions of all authors.

## ACKNOWLEDGMENT

The authors would like to thank Ryerson University for funding. B.A.H. acknowledges the Engineering and Physical Sciences Research Council (EPSRC) Centre for Doctoral Training in Soft Matter and Functional Interfaces (SOFI) for a PhD studentship. A.T.T. and A.N.B. acknowledge EPSRC Doctoral Training Grants. MP acknowledges NSERC RTI for support. The authors also thank Profs. Bryan Koivisto and Stefania Impellizzeri (Ryerson University) for advice and support.

## REFERENCES

- a) Sessler, J.L.; Seidel, D. Synthetic Expanded Porphyrin Chemistry. *Angew. Chem. Int. Ed.* **2003**, *42*(42), 5134-75. b) da GH Vicente, M.; Smith, K.M. Syntheses and Functionalizations of Porphyrin Macrocycles. *Curr. Org. Synth.* **2014**, *11*(1), 3-28. c) Day, N.U.; Wamser, C.C.; Walter, M.G. Porphyrin Polymers and Organic Frameworks. *Polymer Int.* **2015**, *64*(7), 833-57. d) Hiroto, S.; Miyake, Y.; Shinokubo, H. Synthesis and Functionalization of Porphyrins through Organometallic Methodologies. *Chem. Rev.* **2017**, *117*(4), 2910-3043. e) Mahmood, A.; Hu, J.Y.; Xiao, B.; Tang, A.; Wang, X.; Zhou, E. Recent Progress in Porphyrin-Based Materials for Organic Solar Cells. *J. Mater. Chem. A* **2018**, *6*(35), 16769-16797.
- Giovannetti, R. The Use of Spectrophotometry UV-Vis for the Study of Porphyrins. *Macro to Nano Spectroscopy* **2012**, *1*, 87-108.
- a) Rothmund, P. A New Porphyrin Synthesis. The Synthesis of Porphin. *J. Am. Chem. Soc.* **1936**, *58*, 625-627. b) Adler, A.D.; Longo, F.R.; Finarelli, J.D.; Assour, J.; Korsakoff, L. A Simplified Synthesis for Meso-Tetraphenylporphine. *J. Org. Chem.* **1967**, *32*(2), 476. c) Lindsey, J.S.; Schreiman, I.C.; Hsu, H.C.; Kearney, P.C.; Marguerettaz, A.M. Rothmund and Adler-Longo Reactions Revisited: Synthesis of Tetraphenylporphyrins under Equilibrium Conditions. *J. Org. Chem.* **1987**, *52*(5), 827-836.
- a) Costas, M. Selective C-H Oxidation Catalyzed by Metalloporphyrins. *Coord. Chem. Rev.* **2011**, *255*(23-24), 2912-2932. b) Shanmugam, S.; Xu, J.; Boyer, C. Exploiting Metalloporphyrins for Selective Living Radical Polymerization Tunable over Visible Wavelengths. *J. Am. Chem. Soc.* **2015**, *137*(28), 9174-9185. c) Huang, X.; Groves, J.T. Oxygen Activation and Radical Transformations in Heme Proteins and Metalloporphyrins. *Chem. Rev.* **2018**, *118*(5), 2491-2553.
- Kou, J.; Dou, D.; Yang, L. Porphyrin Photosensitizers in Photodynamic Therapy and its Applications. *Oncotarget.* **2017**, *8*(46), 81591-81603.
- a) Dougherty, T. J.; Kaufman, J. E.; Goldfarb, A.; Weishaupt, K. R.; Boyle, D. G.; Mittelman, M. Photoradiation Therapy for the Treatment of Malignant Tumors. *Cancer Res.* **1978**, *38*(8), 2628-2635. b) Santoro, A.M.; Lo Giudice, M.C.; D'Urso, A.; Lauceri, R.; Purrello, R.; Milardi, D. Cationic Porphyrins are Reversible Proteasome Inhibitors. *J. Am. Chem. Soc.* **2012**, *134*(25), 10451-10457.
- a) Shi, J.; Liu, T.W.B.; Chen, J.; Green, D.; Jaffray, D.; Wilson, B.C.; Wang, F.; Zheng, G. Transforming a Targeted Porphyrin Theranostic Agent into a PET Imaging Probe for Cancer. *Theranostics* **2011**, *1*, 363-370. b) Huynh, E.; Leung, B.Y.; Helfield, B.L.; Shakiba, M.; Gandier, J.A.; Jin, C.S.; Master, E.R.; Wilson, B.C.; Goertz, D.E.; Zheng, G. In Situ Conversion of Porphyrin Microbubbles to Nanoparticles for Multimodality Imaging. *Nature Nanotech.* **2015**, *10*(4), 325-332. c) Varchi, G.; Foglietta, F.; Canaparo, R.; Ballestri, M.; Arena, F.; Sotgiu, G.; Guerrini, A.; Nanni, C.; Cicoria, G.; Cravotto, G.; Fanti, S.; Serpe, L. Engineered Porphyrin Loaded Core-Shell Nanoparticles for Selective Sonodynamic Anticancer Treatment. *Nanomedicine* **2015**, *10*(23), 3483-3494.
- a) Martinez-Diaz, M.V.; de la Torre, G.; Torres, T. Lighting Porphyrins and Phthalocyanines for Molecular Photovoltaics. *Chem. Commun.* **2010**, *46*(38), 7090-7108. b) Walter, M.G.; Rudine, A.B.; Wamser, C.C. Porphyrins and Phthalocyanines in Solar Photovoltaic Cells. *J. Porphyrins Phthalocyanines* **2010**, *14*(9), 759-792. c) Lu-Lin Li, L.-L.; Diau, E. W.-G. Porphyrin-Sensitized Solar Cells. *Chem. Soc. Rev.* **2013**, *42*(1), 291-304.
- a) Eriksson, K.; Göthelid, E.; Puglia, C.; Bäckvall, J.; Oscarsson, S. Performance of a Biomimetic Oxidation Catalyst Immobilized on Silica Particles. *J. Catal.* **2013**, *303*, 16-21. b) Sheng, W.; Jiang, Q.; Luo, W.; Guo, C. Oxidative Rearrangement of Internal Alkynes to Give One-Carbon-Shorter Ketones via Manganese Porphyrins Catalysis. *J. Org. Chem.* **2013**, *78*(11), 5691-5693. c) Rybicka-Jasińska, K.; Shan, W.; Zawada, K.; Kadish, K.M.; Gryko, D. Porphyrins as Photoredox Catalysts: Experimental and Theoretical Studies. *J. Am. Chem. Soc.* **2016**, *138*(47), 15451-15458. d) Rybicka-Jasińska, K.; König, B.; Gryko, D. Porphyrin-Catalyzed Photochemical C-H Arylation of Heteroarenes. *Eur. J. Org. Chem.* **2017**, 2104-2107.
- Biesaga, M.; Pyrzynska, K.; Trojanowicz, M. Porphyrins in Analytical Chemistry. A Review. *Talanta* **2000**, *51*(2), 209-224.
- White, W. I. Aggregation of Porphyrins and Metalloporphyrins. *In the Porphyrins*; Dolphin, D., Ed.; Academic: New York, 1978; Vol. 5, 303-339.
- a) Murashima, T.; Tsujimoto, S.; Yamada, T.; Miyazawa, T.; Uno, H.; Ono, N.; Sugimoto, N. Synthesis of Water-Soluble Porphyrin and the Corresponding Highly Planar Benzoporphyrin without Meso-Substituents. *Tet. Lett.* **2005**, *46*(1), 113-116. b) Ruzié, C.; Even, P.; Boitrel, B. Dioxygen Binding of Water-Soluble Iron(II) Porphyrins in Phosphate Buffer at Room Temperature. *Org. Biomol. Chem.* **2007**, *5*(10), 1601-1604. c) Remello, S.N.; Kuttassery, F.; Hirano, T.; Nabetani, Y.; Yamamoto, D.; Onuki, S.; Tachibana, H.; Inoue, H. Synthesis of Water-Soluble Silicon-Porphyrin: Protolytic Behaviour of Axially Coordinated Hydroxy Group. *Dalton Trans.* **2015**, *44*(46), 20011-20020.



- (13) a) Paine, J.B.; Kirshner, W.B.; Moskowit, D.W.; Dolphin, D. Improved Synthesis of Octaethylporphyrin. *J. Org. Chem.* **1976**, *41*(24), 3857-3860. b) Thamyongkit, P.; Speckbacher, M.; Diers, J.R.; Kee, H.L.; Kirmaier, C.; Holten, D.; Bocian, D.F.; Lindsey J.S. Swallowtail Porphyrins: Synthesis, Characterization and Incorporation into Porphyrin Dyads. *J. Org. Chem.* **2004**, *69*(11), 3700-3710. c) Oda, K.; Akita, M.; Hiroto, S.; Shinokubo, H. Silylethynyl Substituents as Porphyrin Protecting Groups for Solubilization and Selectivity Control. *Org. Lett.* **2014**, *16*(6), 1818-1821.
- (14) a) Liu, C.; Liu, K.; Wang, C.; Liu, H.; Wang, H.; Su, H.; Li, X.; Chen, B.; and Jiang, J. Elucidating Heterogeneous Photocatalytic Superiority of Microporous Porphyrin Organic Cage. *Nat. Commun.* **2020**, *11*(1), 1047. b) Liu, W.; Lin, C.; Weber, J.A.; Stern, C.L.; Young, R.M.; Wasielewski, M.R.; Stoddart, J.F. Cyclophane-Sustained Ultrastable Porphyrins. *J. Amer. Chem. Soc.* Just Accepted Manuscript DOI: 10.1021/jacs.0c02311.
- (15) Sakamoto, K.; Ohno-Okumura, E. Syntheses and Functional Properties of Phthalocyanines. *Materials* **2009**, *2*(3), 1127-1179.
- (16) a) Xue, J.; Uchida, S.; Rand, B.; Forrest, S. 4.2% Efficient Organic Photovoltaic Cells with Low Series Resistances. *Appl. Phys. Lett.* **2004**, *84*, 3013-3015. b) Kim, D. Y.; So, F.; Gao, Y. Aluminum Phthalocyanine Chloride/C<sub>60</sub> Organic Photovoltaic Cells with High Open-Circuit Voltages. *Sol. Energy Mater. Sol. Cells.* **2009**, *93*, 1688-1691. c) Dumoulin, F.; Durmuş, M.; Ahsen, V.; Nyokong, T. Synthetic Pathways to Water-Soluble Phthalocyanines and Close Analogs. *Coord. Chem. Rev.* **2010**, *254*, 2792-2847. d) Li, X.; Jiang, Y.; Xie, G.; Tai, H.; Sun, P.; Zhang, B. Copper Phthalocyanine Thin Film Transistors for Hydrogen Sulfide Detection. *Sens. Actuators, B.* **2013**, *176*, 1191-1196. e) Çimen, Y.; Ermiş, E.; Dumludag, F.; Özkaya, A.R.; Salih, B.; Bekaroglu, Ö. Synthesis, Characterization, Electrochemistry and VOC Sensing Properties of Novel Ball-Type Dinuclear Metallophthalocyanines. *Sens. Actuators B: Chem.* **2014**, *202*, 1137-1147. f) Colomban, C.; Kudrik, E.V.; Afanasiev, P.; Sorokin, A.B. Degradation of Chlorinated Phenols in Water in the Presence of H<sub>2</sub>O<sub>2</sub> and Water-Soluble  $\mu$ -Nitrido Diiron Phthalocyanine. *Catal. Today* **2014**, *235*, 14-19. g) Matsuzaki, H.; Murakami, T.N.; Masaki, N.; Furube, A.; Kimura, M.; Mori, S. Dye Aggregation Effect on Interfacial Electron-Transfer Dynamics in Zinc Phthalocyanine-Sensitized Solar Cells. *J. Phys. Chem. C.* **2014**, *118*, 17205-17212. h) Arican, D.; Erdogmus, A.; Koca, A. Electrochromism of the Langmuir-Blodgett Films Based on Monophthalocyanines Carrying Redox Active Metal Centers. *Thin Solid Films.* **2014**, *550*, 669-676. i) Melville, O.A.; Lessard, B.H.; Bender, T.P. Phthalocyanine-Based Organic Thin-Film Transistors: A Review of Recent Advances. *ACS Appl. Mater. Interfaces* **2015**, *7*(24), 13105-13118.
- (17) a) Lessard, B.H.; Dang, J.D.; Grant, T.M. Gao, D.; Seferos, D.S.; Bender, T.P. Bis(tri-*n*-hexylsilyl oxide) Silicon Phthalocyanine: A Unique Additive in Ternary Bulk Heterojunction Organic Photovoltaic Devices. *ACS Appl. Mater. Interfaces* **2014**, *6*(17), 15040-15051. b) Lim, B.; Bloking, J. T.; Ponec, A.; McGehee, M. D.; Sellinger, A. Ternary Bulk Heterojunction Solar Cells: Addition of Soluble NIR Dyes for Photocurrent Generation beyond 800 nm. *ACS Appl. Mater. Interfaces* **2014**, *6*(9), 6905-6913. c) Lessard, B.H.; White, R.T.; AL-Amar, M.; Plint, T.; Castrucci, J.S.; Josey, D.S.; Lu, Z.; Bender, T.P. Assessing the Potential Roles of Silicon and Germanium Phthalocyanines in Planar Heterojunction Organic Photovoltaic Devices and How Pentafluoro Phenoxylation Can Enhance  $\pi$ - $\pi$  Interactions and Device Performance. *ACS Appl. Mater. Interfaces* **2015**, *7*(9), 5076-5088.
- (18) Kane, K.M.; Lemke, F.R.; Petersen J.L. Bis(trifluoromethanesulfonato)(tetra-*p*-tolylporphyrinato)silicon(IV), (TTP)Si(OTf)<sub>2</sub>: The First Structurally Characterized (Porphyrinato)silicon(IV) Complex. *Inorg. Chem.* **1995**, *34*(16), 4085-4091.
- (19) A recent publication details the on-surface synthesis of PorSils: Baklanov, A. Garnica, M.; Robert, A.; Bocquet, M.-L.; Seufert, K.; Kuchle, J.T.; Ryan, P.T.P.; Haag, F.; Kakavandi, R.; Allegretti, F.; Auwärter, W. On-Surface Synthesis of Non-metal Porphyrins. *J. Am. Chem. Soc.* **2020**, *142*(4), 1871-1881.
- (20) Liu, J.; Yang, X.; Sun, L. Axial Anchoring Designed Silicon-Porphyrin Sensitizers for Efficient Dye-Sensitized Solar Cells. *Chem. Commun.* **2013**, *49*, 11785-11787.
- (21) Yutronkie, N.J.; Grant, T.M.; Melville, O.A.; Lessard, B.H.; Brusso, J.L. Old Molecule, New Chemistry: Exploring Silicon Phthalocyanines as Emerging N-Type Materials in Organic Electronics. *Materials* **2019**, *12*(8), 1334.
- (22) Interestingly, while both i) the exposed hydroxy functionality of the silica gel surface and ii) methanol form stable bonds to the PorSil to make their respective adducts, attempts to form and isolate the TPP-Si(OEt)<sub>2</sub> derivative resulted instead in hydrolysis and the formation of **3**. This suggests that the Si-O-C in this porphyrin system is more reactive than Si-Cl in 2-SiCl<sub>2</sub>. Attempts to synthesize and observe bulkier alkoxy variants, namely TPP-Si(O<sup>i</sup>Pr)<sub>2</sub> and TPP-Si(O<sup>t</sup>Bu)<sub>2</sub>, were also unsuccessful. Also noteworthy to mention is that the bis(trimethylsilyloxy) derivative proved hydrolytically unstable when exposed to the atmosphere and thus was not evaluated in this study. These findings highlight the vital nature of the steric bulk of the axial substituent with respect to the properties of this family of compounds.
- (23) As a point of interest, two reduced antiaromatic porphyrin silanes have been synthesized, and in these the resonances of the protons on the axial substituents are shifted significantly downfield upon coordination: Cissell, J.A.; Vaid, T.P.; Rheingold, A.L. An Antiaromatic Porphyrin Complex: Tetrphenylporphyrinato(silicon)(L)<sub>2</sub> (L = THF or Pyridine). *J. Am. Chem. Soc.* **2005**, *127*(35), 12212-12213.
- (24) Vangberg, T.; Ghosh, A. A First-Principles Quantum Chemical Analysis of the Factors Controlling Ruffling Deformations of Porphyrins: Insights from the Molecular Structures and Potential Energy Surfaces of Silicon, Phosphorus, Germanium, and Arsenic Porphyrins and of a Peroxidase Compound I Model. *J. Am. Chem. Soc.* **1999**, *121*(51), 12154-12160.
- (25) Planarity can be quantified by evaluating the position of the meso carbons of the porphyrin compared to the plane defined by the pyrrole nitrogen atoms; to acquire our data, we established a plane defined by N1, Si1, and N2 (i.e. the central silicon and two cis-coordinated porphyrin nitrogen atoms) and measured the shortest distance between this plane and each meso carbon. These distances are then averaged to give the common descriptor  $\Delta r$ .
- (26) Shelnut, J.A.; Song, X.-Z.; Ma, J.-G.; Jia, S.-L.; Jentzen, W.; Medforth, C.J. Nonplanar Porphyrins and their Significance in Proteins. *Chem. Soc. Rev.* **1998**, *27*(1), 31-41.
- (27) Jian-Yu, Z.; Katsuaki, K.; Aida, T. Dioxygen Insertion into the Axial Si-C Bonds of Organosilicon Porphyrins. *Chem. Lett.* **1998**, *5*, 453-454.
- (28) Zheng, J.-Y.; Konishi, K.; Aida, T. Crystallographic Studies of Organosilicon Porphyrins: Stereoelectronic Effects of Axial Groups on the Nonplanarity of the Porphyrin Ring. *Inorg. Chem.* **1998**, *37*(10), 2591-2594.
- (29) See paper in ref. 23.
- (30) Ishida, S.; Yoshimura, K.; Matsumoto, H.; Kyushin, S. Selective Si-C Bond Cleavage on a Diorganosilicon Porphyrin Complex Bearing Different Axial Ligands. *Chem. Lett.* **2009**, *38*(4), 362-363.
- (31) Kane, K.M.; Lemke, F.R.; Petersen, J.L. *trans*-Difluorosilicon(IV) Complexes of Tetra-*p*-tolylporphyrin and Tetrakis(*p*-(trifluoromethyl)phenyl)porphyrin: Crystal

- Structures and Unprecedented Reactivity in Hexacoordinate Difluorosilanes<sup>1</sup>. *Inorg. Chem.* **1997**, *36*(7), 1354-1359.
- (32) Observed bond lengths for Si-X in crystal structure of porphyrin silane (PorSil) and a tetracoordinated (4c) silane (with reference): X = OH, PorSil = 1.67 Å, 4c = 1.66 Å (ref. 23); C<sub>H</sub>CH<sub>2</sub>, PorSil = 1.83 Å (ref. 24), 4c = 1.86 Å (Bartkowska, B.; Krüger, C. Tetravinylsilane. *Acta Cryst.* **1997**, *C53*, 1066-1068.); CCPH, PorSil = 1.82 Å (ref. 24), 4c = 1.83 Å (Wrackmeyer, B.; Khana, E.; Bayer, S.; Toka, O.L.; Klimkina, E.V.; Miliusc, W.; Kempe, R. Alkynylsilanes and Alkynyl(vinyl)silanes. Synthesis, Molecular Structures and Multinuclear Magnetic Resonance Study. *Z. Naturforsch.* **2010**, *65b*, 725-744.); CH<sub>2</sub>TMS, PorSil = 1.93 Å (ref. 24), 4c = 1.92 Å (Buttrus, N.H.; Eaborn, C.; Hitchcock, P.B.; Lickiss, P.D.; Najim, S.T. 1,3 Silicon to Silicon Migration of the Methoxy Group in Solvolysis of (bromodiphenylsilyl)(methoxydimethylsilyl)bis(trimethylsilyl)methane. Crystal Structures of (ethoxydimethylsilyl)(methoxydiphenylsilyl)bis(trimethylsilyl)-methane and (methoxydimethylsilyl)(methoxydiphenylsilyl)bis(trimethylsilyl)methane). *J. Chem. Soc. Perkin Trans. II* **1987**, 1753-1757.). As a point of reference, here are two examples for non-planar porphyrins: Ph, PorSil = 1.94 Å (ref. 24), 4c = 1.86 Å (Párkányi, L.; Sasvári, K. Crystal structure of tetraphenylsilane. *Period. Polytechnic. Chem. Eng.* **1973**, *17*(3), 271-276.); F, PorSil = 1.64 Å (ref. 26), 4c = 1.60 Å (Dell, S.; Ho, D.M.; Pascal, R.A. *in- and out-Cyclophanes Bearing Non-Hydrogen Bridgehead Substituents.* *J. Org. Chem.* **1999**, *64*(15), 5626-5633.)
- (33) Spackman, M. A.; Jayatilaka, D. Hirshfeld Surface Analysis. *CrystEngComm* **2009**, *11*(1), 19-32.
- (34) Ralphs, K.; Zhang, C.; James, S. L. Solventless Mechanochemical Metalation of Porphyrins. *Green Chem.* **2017**, *19*(1), 102-105.
- (35) Valicsek, Z.; Horváth, O. Application of the Electronic Spectra of Porphyrins for Analytical Purposes: The Effects of Metal Ions and Structural Distortions. *Microchem. J.* **2013**, *107*, 47-62.
- (36) Uttamlal, M.; Holmes-Smith, A.S. The Excitation Wavelength Dependent Fluorescence of Porphyrins. *Chem. Phys. Lett.* **2008**, *454*(4-6), 223-228.
- (37) Ghosh, M.; Nath, S.; Hajra, A.; Sinha, S. Fluorescence Self-Quenching of Tetraphenylporphyrin in Liquid Medium. *J. Lumin.* **2013**, *141*, 87-92.
- (38) Zheng, W.; Shan, N.; Yu, L.; Wang, X. UV-visible, Fluorescence and EPR Properties of Porphyrins and Metalloporphyrins. *Dyes Pigm.* **2008**, *77*, 153-157.
- (39) Chen, Z.; Lohr, A.; Saha-Möller, C.R.; Würthner, F. Self-Assembled  $\pi$ -Stacks of Functional Dyes in Solution: Structural and Thermodynamic Features. *Chem. Soc. Rev.* **2009**, *38*(2), 564-584.

PorSil paper final.pdf (2.97 MiB)

[view on ChemRxiv](#) • [download file](#)

---

# Control of Porphyrin Planarity and Aggregation by Covalent Capping: Bissilyloxy Porphyrin Silanes

## *Supporting Information*

Burhan A. Hussein,<sup>†,‡</sup> Zainab Shakeel,<sup>†</sup> Andrew T. Turley,<sup>‡</sup> Aisha N. Bismillah,<sup>‡,§</sup> Kody M. Wolfstadt,<sup>†</sup> Julia E. Pia,<sup>†</sup> Melanie Pilkington,<sup>⊥</sup> Paul R. McGonigal,<sup>‡</sup> and Marc J. Adler<sup>†,\*</sup>

<sup>†</sup> Department of Chemistry & Biology, Ryerson University, 350 Victoria St., Toronto, ON, M5B 2K3, Canada

<sup>‡</sup> Department of Chemistry, Durham University, Lower Mountjoy, Stockton Road, Durham, DH1 3LE, United Kingdom

<sup>§</sup> Department of Chemistry, Dartmouth College, Hanover, New Hampshire, 03755, USA

<sup>⊥</sup> Department of Chemistry, Brock University, 1812 Sir Isaac Brock Way, St. Catharines, ON, L2S 3A1, Canada

## Table of Contents

1. GENERAL METHODS.....	3
2. SYNTHETIC DETAILS.....	5
3. $^1\text{H}$ , $^{13}\text{C}$ , AND VARIABLE-TEMPERATURE NMR SPECTROSCOPIC CHARACTERIZATION OF SYNTHESIZED COMPOUNDS.	15
4. UV-VIS SPECTROSCOPY .....	34
5. PHOTOLUMINESCENCE SPECTROSCOPY.....	44
6. CYCLIC VOLTAMMETRY .....	49
7. X-RAY CRYSTALLOGRAPHIC ANALYSIS.....	57
7.1 INTRAMOLECULAR CONTACTS IN SOLID STATE.....	63
8. <i>IN SILICO</i> MODELLING .....	69
9. HIRSHFELD SURFACE ANALYSIS OF SOLID-STATE STRUCTURES .....	71
10. CALCULATION OF INTERMOLECULAR INTERACTION ENERGIES IN THE SOLID STATE .....	81
11. COMPOUND IDENTITY VALIDATION BY LOW RESOLUTION MASS SPECTRA.....	87
12. REFERENCES.....	92

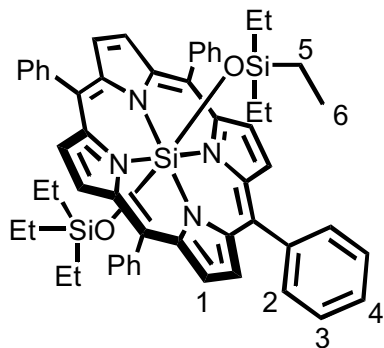
## 1. General Methods

**Materials:** All reagents were purchased from commercial suppliers (Sigma-Aldrich, Alfa Aesar, or Oakwood Chemicals) and used without further purification.

**Instrumentation and Analytical Techniques:** Purification by column chromatography was carried out using silica (Silicycle: ultrapure flash silica). Analytical thin-layer chromatography (TLC) was performed on aluminum-backed sheets pre-coated with silica 60 F<sub>254</sub> adsorbent (0.25 mm thick; Silicycle) and visualized under UV light (254 nm), if needed. Routine <sup>1</sup>H and <sup>13</sup>C{<sup>1</sup>H} nuclear magnetic resonance (NMR) spectra were recorded at 400 MHz and 101 MHz respectively, on a Bruker AV 400 instrument at ambient temperatures. Variable-temperature (VT) NMR was recorded on a Varian Inova 500 (<sup>1</sup>H 500.130 MHz) at range of temperatures. For VT measurements, operating temperatures were calibrated using an internal calibration solution of MeOH and glycerol. Chemical shifts ( $\delta$ ) are reported in parts per million (ppm) from low to high field and referenced to a residual non-deuterated solvent (CHCl<sub>3</sub>) peak for <sup>1</sup>H and <sup>13</sup>C nuclei. Coupling constants (*J*) are reported in Hertz (Hz). Standard abbreviations indicating multiplicity are used as follows: s = singlet; d = doublet; m = multiplet; br = broad). <sup>13</sup>C NMR experiments were proton decoupled. NMR spectra were processed using MestReNova version 11.0. Data are reported as follows: chemical shift; multiplicity; coupling constants; integral and assignment. Low resolution mass spectrometry (MS) results were obtained on a Waters GCT Premier instrument using electron impact (EI) for ionization. High-resolution electrospray (HR-ESI) mass spectra were measured using a Waters LCT Premier XE high resolution, accurate mass UPLC ES MS with ASAP ion source. Cyclic voltammetry (CV) data were collected using a Metrohm  $\mu$ -Autolab Type III potentiostat/galvanostat and are reported relative to the potential of the normal hydrogen electrode (NHE). UV-Vis spectroscopy data was obtained using a Cary

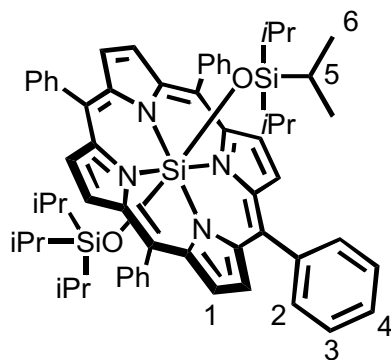
Series UV-Vis Spectrophotometer from Agilent Technologies. Steady-state photoluminescence (PL) solution data were obtained using a Perkin-Elmer LS 50 B Luminescence Spectrometer. Steady-state PL of films and solutions were measured using Jobin Yvon Fluoromax and Fluorolog with machine-specific calibration curves. The low temperature and temperature-dependent PL spectra were measured using a Janis Research Co. Inc. nitrogen filled cryostat. Thus, at low temperature, films were in a nitrogen atmosphere and solutions in a sealed long-neck cuvette. Suitable single crystals of all four compounds **1f-i** were mounted on a cryoloop with paratone oil and examined on a Bruker APEX-II CCD diffractometer. All four compounds have been deposited in the Cambridge Structural Database with numbers CCDC 1977452-1977455.

## 2. Synthetic Details

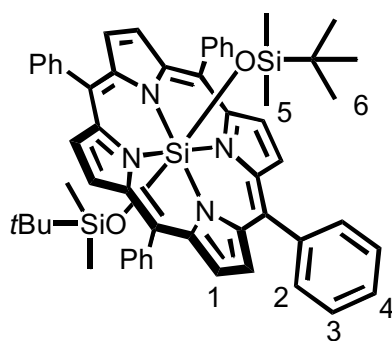


**1a:** In a 50 mL round-bottom flask with a magnetic stir bar, **3** (100 mg, 0.15 mmol) was dissolved in 1,2-dichloroethane (10 mL) to which Et<sub>3</sub>N (50  $\mu$ L, 0.37 mmol) was added. The reaction mixture was stirred for 5 min, followed by the addition of triethylchlorosilane (40 mg, 0.37 mmol). The reaction was refluxed overnight and monitored by TLC. Upon completion, the reaction mixture was concentrated *in vacuo* and the crude residue was purified using a short silica plug (petroleum ether:Et<sub>3</sub>N, 9:1), R<sub>f</sub> = 0.70. The filtrate was then triturated using cold MeCN until no further precipitation occurred. The solid was filtered through a sintered glass funnel which was then dried under vacuum to yield **1a** as a purple solid (127 mg, 0.14 mmol, 95%). **<sup>1</sup>H NMR** (400 MHz, CDCl<sub>3</sub>)  $\delta$  8.83 (s, 8H, H<sub>1</sub>), 8.18 – 8.13 (m, 8H, H<sub>2</sub>), 7.79 – 7.70 (m, 12H, H<sub>3</sub>, H<sub>4</sub>), -1.36 (t,  $J$  = 7.9 Hz, 18H, H<sub>6</sub>), -2.68 (q,  $J$  = 8.0 Hz, 12H, H<sub>5</sub>). **<sup>13</sup>C NMR** (101 MHz, CDCl<sub>3</sub>)  $\delta$  143.9, 141.7, 134.1, 130.5, 127.7, 126.8, 117.7, 4.49, 2.80. **IR** (cm<sup>-1</sup>) 3057, 2942, 2867, 2797, 2378, 2265, 2101, 2081, 1944, 1881, 1758, 1597, 1534, 1491, 1439, 1409, 1354, 1226, 1205, 1173, 1060, 1006, 882, 845, 801, 748. **UV-Vis** (CH<sub>2</sub>Cl<sub>2</sub>):  $\lambda_{\text{max}}$  (nm) 421 (Soret band), 513, 552, 589, 625 (Q bands); **Fluorescence** (CH<sub>2</sub>Cl<sub>2</sub>,  $\lambda_{\text{ex}}$  = 430):  $\lambda_{\text{em}}$  (nm) 605, 643. **HRMS-ASAP**  $m/z$  [M]<sup>+</sup> calculated for C<sub>56</sub>H<sub>58</sub>N<sub>4</sub>O<sub>2</sub>Si<sub>3</sub> 902.3868, measured 902.3912. **CV** (V vs NHE, ref to Fc/Fc<sup>+</sup>) -1.119, 1.321.



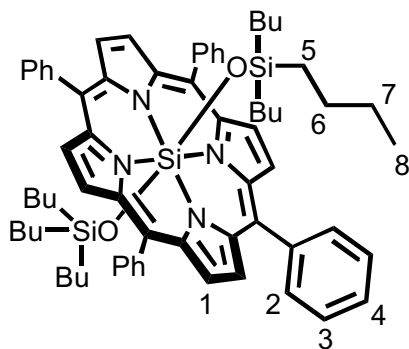


**1b:** In a 50 mL round-bottom flask with a magnetic stir bar, **3** (100 mg, 0.15 mmol) was dissolved in 1,2-dichloroethane (10 mL) to which Et<sub>3</sub>N (50 μL, 0.37 mmol) was added. The reaction mixture was stirred for 5 min, followed by the addition of triisopropylchlorosilane (71 mg, 0.37 mmol). The reaction was refluxed overnight and monitored by TLC. Upon completion, the reaction mixture was concentrated *in vacuo* and the crude residue was purified using a short silica plug (petroleum ether:Et<sub>3</sub>N, 9:1), R<sub>f</sub> = 0.72. The filtrate was then triturated using cold MeCN until no further precipitation occurred. The solid was filtered through a sintered glass funnel which was then dried under vacuum to yield **1b** as a purple solid (132 mg, 0.14 mmol, 91%). **<sup>1</sup>H NMR** (400 MHz, CDCl<sub>3</sub>) δ 8.82 (s, 8H, H<sub>1</sub>), 8.15 – 8.07 (m, 8H, H<sub>2</sub>), 7.81 – 7.69 (m, 12H, H<sub>3</sub>, H<sub>4</sub>), -1.31 (d, *J* = 7.5 Hz, 36H, H<sub>6</sub>), -2.26 (septet, *J* = 7.5 Hz, 6H, H<sub>5</sub>). **<sup>13</sup>C NMR** (101 MHz, CDCl<sub>3</sub>) δ 144.3, 141.6, 134.0, 130.8, 127.8, 126.8, 118.3, 15.5 11.0. **IR** (cm<sup>-1</sup>) 2918, 2857, 2168, 2116, 2078, 1883, 1817, 1597, 1533, 1491, 1354, 1232, 1205, 1172, 1076, 1033, 1007, 881, 836, 800, 747, 698. **UV-Vis** (CH<sub>2</sub>Cl<sub>2</sub>): λ<sub>max</sub> (nm) 422 (Soret band), 512, 550, 591, 623 (Q bands). **Fluorescence** (CH<sub>2</sub>Cl<sub>2</sub>, λ<sub>ex</sub> = 430 nm): λ<sub>em</sub> (nm) 592, 627. **MS** (EI<sup>+</sup>) *m/z* [M]<sup>+</sup> calculated for C<sub>62</sub>H<sub>70</sub>N<sub>4</sub>O<sub>2</sub>Si<sub>3</sub> 986.5, measured 986.5. **CV** (V vs NHE ref to Fc/Fc<sup>+</sup>) -1.218, 1.353.



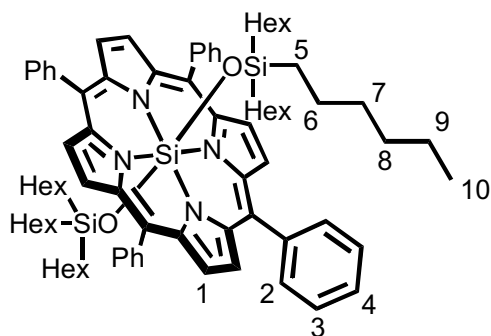
**1c:** In a 50 mL round-bottom flask with a magnetic stir bar, **3** (100 mg, 0.15 mmol) was dissolved in 1,2-dichloroethane (10 mL) to which Et<sub>3</sub>N (50 μL, 0.37 mmol) was added. The reaction mixture was stirred for 5 min, followed by the addition of *tert*-butyldimethylchlorosilane (56 mg, 0.37 mmol). The reaction

was refluxed overnight and monitored by TLC. Upon completion, the reaction mixture was concentrated *in vacuo* and the crude residue was purified using a short silica plug (petroleum ether:Et<sub>3</sub>N, 9:1), R<sub>f</sub> = 0.72. The filtrate was then triturated using cold MeCN until no further precipitation occurred. The solid was filtered through a sintered glass funnel which was then dried under vacuum to yield **1c** as a purple solid (115 mg, 0.13 mmol, 86%). **<sup>1</sup>H NMR** (400 MHz, CDCl<sub>3</sub>) δ 8.86 (s, 8H, H<sub>1</sub>), 8.20 – 8.14 (m, 8H, H<sub>2</sub>), 7.81 – 7.70 (m, 12H, H<sub>3</sub>, H<sub>4</sub>), -1.61 (s, 18H, H<sub>6</sub>), -3.34 (s, 12H, H<sub>5</sub>). **<sup>13</sup>C NMR** (101 MHz, CDCl<sub>3</sub>) δ 144.5, 141.9, 134.1, 127.8, 126.7, 118.4, 120.2, 23.2, 15.1, 7.5. **IR** (cm<sup>-1</sup>) 2920, 2848, 1597, 1537, 1491, 1440, 1355, 1240, 1207, 1062, 1008, 939, 829, 801, 749. **UV-Vis** (CH<sub>2</sub>Cl<sub>2</sub>): λ<sub>max</sub> (nm) 418 (Soret band), 512, 549, 586, 618 (Q bands); **Fluorescence** (CH<sub>2</sub>Cl<sub>2</sub>, λ<sub>ex</sub> = 427): λ<sub>em</sub> (nm) 605, 646. **MS** (EI+) *m/z* [M]<sup>+</sup> calculated for C<sub>56</sub>H<sub>58</sub>N<sub>4</sub>O<sub>2</sub>Si<sub>3</sub> 902.38, measured 902.39. **CV** (V vs NHE ref to Fc/Fc<sup>+</sup>) -1.144, 1.342.



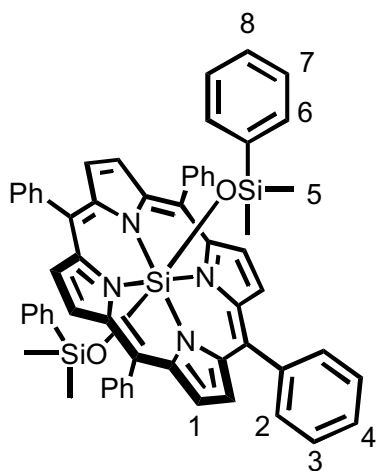
**1d:** In a 50 mL round-bottom flask with a magnetic stir bar, **3** (100 mg, 0.15 mmol) was dissolved in 1,2-dichloroethane (10 mL) to which Et<sub>3</sub>N (50 μL, 0.37 mmol) was added. The reaction mixture was stirred for 5 min, followed by the addition of tributylchlorosilane (87 mg, 0.37 mmol). The reaction mixture was refluxed overnight and monitored by TLC. Upon completion, the reaction mixture was concentrated *in vacuo* and the residue was purified using a short silica plug (petroleum ether:Et<sub>3</sub>N, 9:1), R<sub>f</sub> = 0.72. The filtrate was then triturated using cold MeCN until no further precipitation occurred. The solid was filtered through a sintered glass funnel which was then dried under vacuum to yield **1d** as a purple solid (141 mg, 0.13 mmol, 89%). **<sup>1</sup>H NMR** (400 MHz, CDCl<sub>3</sub>) δ 8.83 (s, 8H, H<sub>1</sub>), 8.18 (d, *J* = 5.8 Hz, 8H, H<sub>2</sub>), 7.80 – 7.69 (m, 12H, H<sub>3</sub>, H<sub>4</sub>), 0.36 – 0.17 (m, 30H, H<sub>7</sub>, H<sub>8</sub>),

-1.18 – -1.46 (m, 12H, H<sub>6</sub>), -2.54 – -2.95 (m, 12H, H<sub>5</sub>). <sup>13</sup>C NMR (100 MHz, CDCl<sub>3</sub>) δ 143.9, 141.8, 134.4, 130.6, 127.8, 126.8, 117.8, 26.1, 23.4, 13.5, 12.2. IR (cm<sup>-1</sup>) 2951, 2914, 2850, 1598, 1534, 1490, 1440, 1355, 1292, 1059, 1008, 883, 800, 752. UV-Vis (CH<sub>2</sub>Cl<sub>2</sub>): λ<sub>max</sub> (nm) 424 (Soret band), 514, 555, 596, 627 (Q bands); Fluorescence (CH<sub>2</sub>Cl<sub>2</sub>, λ<sub>ex</sub> = 424): λ<sub>em</sub> (nm) 598, 645. MS (EI+) *m/z* [M]<sup>+</sup> calculated for C<sub>68</sub>H<sub>82</sub>N<sub>4</sub>O<sub>2</sub>Si<sub>3</sub> 1070.5, measured 1070.5. CV (V vs NHE, ref to Fc/Fc<sup>+</sup>) -1.184, 1.307.

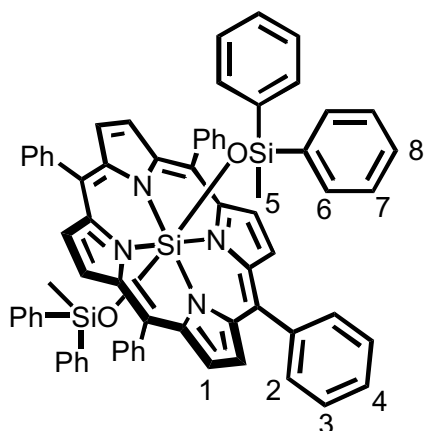


**1e:** In a 50 mL round-bottom flask with a magnetic stir bar, **3** (100 mg, 0.15 mmol) was dissolved in 1,2-dichloroethane (10 mL) to which Et<sub>3</sub>N (50 μL, 0.37 mmol) was added. The reaction mixture was stirred for 5 min, followed by the addition of trihexylchlorosilane (105 mg, 0.37 mmol). The reaction mixture was refluxed overnight and monitored by TLC. Upon completion, the reaction mixture was concentrated *in vacuo* and the residue was purified using a short silica plug (petroleum ether:Et<sub>3</sub>N, 9:1), R<sub>f</sub> = 0.72. The filtrate was then triturated using cold MeCN until no further precipitation occurred. The solid was filtered through a sintered glass funnel which was then dried under vacuum to yield **1e** as a purple solid (178 mg, 0.15 mmol, 97%). <sup>1</sup>H NMR (400 MHz, CDCl<sub>3</sub>) δ 8.82 (s, 8H, H<sub>1</sub>), 8.21 – 8.13 (m, 8H, H<sub>2</sub>), 7.80 – 7.67 (m, 12H, H<sub>3</sub>, H<sub>4</sub>), 1.02 – 0.85 (m, 18H, H<sub>10</sub>), 0.71 (t, *J* = 7.3 Hz, 12H, H<sub>9</sub>), 0.63 (tt, *J* = 9.4, 6.5 Hz, 12H, H<sub>8</sub>), 0.23 (tt, *J* = 7.5, 7.5 Hz, 12H, H<sub>7</sub>), -1.33 (m, 12H, H<sub>6</sub>), -2.67 – -2.82 (m, 12H, H<sub>5</sub>). <sup>13</sup>C NMR (101 MHz, CDCl<sub>3</sub>) δ 143.7, 134.3, 130.5, 141.6, 127.7, 126.6, 117.6, 32.9, 31.15, 22.5, 21.0, 14.1, 12.3. IR (cm<sup>-1</sup>) 2953, 2916, 2849, 1597, 1526, 1490, 1440, 1356, 1207, 1176, 1068, 1010, 884, 799, 750. UV-Vis (CH<sub>2</sub>Cl<sub>2</sub>): λ<sub>max</sub> (nm) 423 (Soret band), 514, 555, 595, 627 (Q bands); Fluorescence

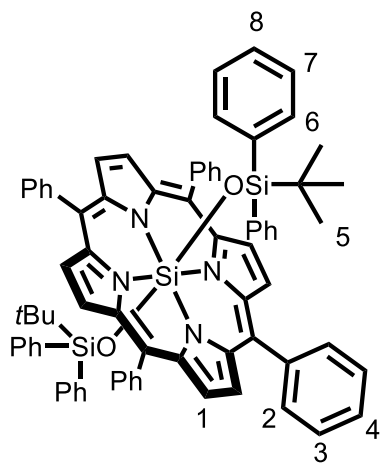
(CH<sub>2</sub>Cl<sub>2</sub>,  $\lambda_{\text{ex}} = 423$ ):  $\lambda_{\text{em}}$  (nm) 602, 649. **HRMS-ESI**  $m/z$  [M]<sup>+</sup> calculated for C<sub>80</sub>H<sub>106</sub>N<sub>4</sub>O<sub>2</sub>Si<sub>3</sub> 1238.7653, measured 1238.7653. **CV** (V vs NHE, ref to Fc/Fc<sup>+</sup>) -1.235, 1.317.



**1f**: In a 50 mL round-bottom flask with a magnetic stir bar, **3** (100 mg, 0.15 mmol) was dissolved in 1,2-dichloroethane (10 mL) to which Et<sub>3</sub>N (50  $\mu$ L, 0.37 mmol) was added. The reaction mixture was stirred for 5 min, followed by the addition of dimethylphenylchlorosilane (63 mg, 0.37 mmol). The reaction mixture was refluxed overnight and monitored by TLC. Upon completion, the reaction mixture was concentrated *in vacuo* and the residue was purified using a short silica plug (petroleum ether:Et<sub>2</sub>O:Et<sub>3</sub>N, 5:2:1), R<sub>f</sub> = 0.63. The filtrate was then triturated using cold EtOH until no further precipitation occurred. The solid was filtered through a sintered glass funnel which was then dried under vacuum to yield **1f** as a purple solid (129 mg, 0.14 mmol, 92%). **<sup>1</sup>H NMR** (400 MHz, CDCl<sub>3</sub>)  $\delta$  8.82 (s, 8H, H<sub>1</sub>), 7.98 – 7.91 (m, 8H, H<sub>2</sub>), 7.75 – 7.69 (m, 4H, H<sub>4</sub>), 7.69 – 7.63 (m, 8H, H<sub>3</sub>), 6.72 (tt,  $J = 7.4, 1.4$  Hz, 2H, H<sub>8</sub>), 6.50 – 6.41 (m, 4H, H<sub>7</sub>), 4.52 (dd,  $J = 7.9, 1.4$  Hz, 4H, H<sub>6</sub>), -2.89 (s, 12H, H<sub>5</sub>). **<sup>13</sup>C NMR** (101 MHz, CDCl<sub>3</sub>)  $\delta$  177.8, 143.6, 141.1, 140.2, 134.2, 131.1, 131.1, 127.9, 127.3, 126.9, 126.2, 2.8. **IR** (cm<sup>-1</sup>) 3051, 2946, 2552, 2377, 2104, 2077, 1884, 1814, 1761, 1597, 1533, 1490, 1440, 1399, 1355, 1239, 1206, 1174, 1115, 1067, 1007, 799, 743. **UV-Vis** (CH<sub>2</sub>Cl<sub>2</sub>):  $\lambda_{\text{max}}$  (nm) 423 (Soret band), 514, 552, 591, 628 (Q bands). **Fluorescence** (CH<sub>2</sub>Cl<sub>2</sub>,  $\lambda_{\text{ex}} = 427$ ):  $\lambda_{\text{em}}$  (nm) 605, 649. **HRMS-ASAP**  $m/z$  [M+H]<sup>+</sup> calculated for C<sub>60</sub>H<sub>51</sub>N<sub>4</sub>O<sub>2</sub>Si<sub>3</sub> 943.3320, measured 943.3338. **CV** (V vs NHE, ref to Fc/Fc<sup>+</sup>) -1.099, 1.349.



**1g:** In a 50 mL round-bottom flask with a magnetic stir bar, **3** (100 mg, 0.15 mmol) was dissolved in 1,2-dichloroethane (10 mL) to which Et<sub>3</sub>N (50 μL, 0.37 mmol) was added. The reaction mixture was stirred for 5 min, followed by the addition of CH<sub>3</sub>Si(C<sub>6</sub>H<sub>5</sub>)<sub>2</sub>Cl (86 mg, 0.37 mmol). The reaction mixture was refluxed overnight and monitored by TLC. Upon completion, the reaction mixture was concentrated *in vacuo* and the residue was purified using a short silica plug (petroleum ether:Et<sub>2</sub>O:Et<sub>3</sub>N, 5:2:1), R<sub>f</sub> = 0.63. The filtrate was then triturated using cold EtOH until no further precipitation occurred. The solid was filtered through a sintered glass funnel which was then dried under vacuum to yield **1g** as a purple solid (130 mg, 0.12 mmol, 82 %). **<sup>1</sup>H NMR** (400 MHz, CDCl<sub>3</sub>) δ 8.75 (s, 8H, H<sub>1</sub>), 7.75 – 7.66 (dd, 12H, H<sub>4</sub>, H<sub>2</sub>), 7.63 (t, *J* = 7.4 Hz, 8H, H<sub>3</sub>), 6.78 (tt, *J* = 7.7, 1.3 Hz, 4H, H<sub>8</sub>), 6.49 (t, *J* = 7.4 Hz, 8H, H<sub>7</sub>), 4.56 (dd, *J* = 7.9, 1.3 Hz, 8H, H<sub>6</sub>), -2.65 (s, 6H, H<sub>5</sub>). **<sup>13</sup>C NMR** (101 MHz, CDCl<sub>3</sub>) δ 143.8, 141.1, 137.7, 134.3, 131.7, 130.9, 127.8, 127.5, 126.7, 126.3, 118.1, -5.4. **IR** (cm<sup>-1</sup>) 1596, 1541, 1484, 1354, 1247, 1205, 1173, 1110, 1059 (vs), 1008 (vs), 850 (s), 795 (s), 737 (s), 700 (vs). **UV-Vis** (CH<sub>2</sub>Cl<sub>2</sub>): λ<sub>max</sub> (nm) 422 (Soret band), 514, 553, 592, 628 (Q bands); **Fluorescence** (CH<sub>2</sub>Cl<sub>2</sub>, λ<sub>ex</sub> = 423): λ<sub>em</sub> (nm) 600, 648. **MS** (EI+) *m/z* [M]<sup>+</sup> calculated for C<sub>70</sub>H<sub>54</sub>N<sub>4</sub>O<sub>2</sub>Si<sub>3</sub> 1066.35, measured 1066.36. **CV** (V vs NHE, ref to Fc/Fc<sup>+</sup>) -1.105, 1.352.



**1h:** In a 50 mL round-bottom flask with a magnetic stir bar, **3** (100 mg, 0.15 mmol) was dissolved in 1,2-dichloroethane (10 mL) to which Et<sub>3</sub>N (50 μL, 0.37 mmol) was added. The reaction mixture was stirred for 5 min, followed by the addition of *tert*-butyldiphenylchlorosilane (101 mg, 0.37 mmol). The reaction mixture was refluxed overnight and monitored by TLC. Upon completion, the reaction mixture was concentrated *in vacuo* and

the residue was purified using a short silica plug (petroleum ether:Et<sub>2</sub>O:Et<sub>3</sub>N, 5:2:1), R<sub>f</sub> = 0.63.

The filtrate was then triturated using cold EtOH until no further precipitation occurred. The solid was filtered through a sintered glass funnel which was then dried under vacuum to yield **1h** as a

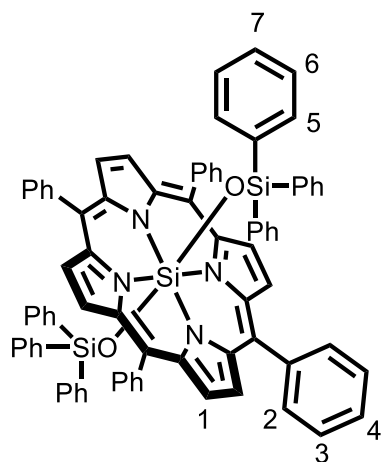
purple solid (154 mg, 0.13 mmol, 90%). **<sup>1</sup>H NMR** (400 MHz, CDCl<sub>3</sub>) δ 8.68 (s, 8H, H<sub>1</sub>), 7.83 (d, *J* = 6.7 Hz, 8H, H<sub>2</sub>), 7.80 – 7.72 (m, 4H, H<sub>4</sub>), 7.69 (t, *J* = 7.2 Hz, 8H, H<sub>3</sub>), 6.89 (t, *J* = 7.4 Hz, 4H, H<sub>8</sub>), 6.60 (t, *J* = 7.5 Hz, 8H, H<sub>7</sub>), 4.56 (d, *J* = 7.1 Hz, 8H, H<sub>6</sub>), -1.40 (s, 18H, H<sub>5</sub>). **<sup>13</sup>C NMR** (101

MHz, CDCl<sub>3</sub>) δ 144.6, 141.4, 134.3, 133.9, 133.4, 130.5, 127.6, 127.1, 126.6, 125.7, 118.5, 24.5, 16.7. **IR** (cm<sup>-1</sup>) 3053, 2923, 2849, 1597, 1540, 1424, 1355, 1259, 1206, 1174, 1102, 1042, 1008,

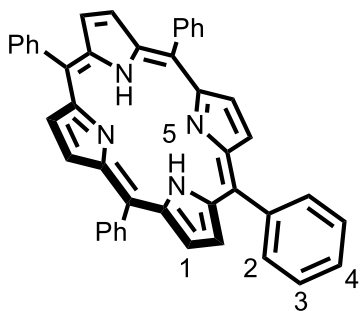
938, 799, 750. **UV-Vis** (CH<sub>2</sub>Cl<sub>2</sub>): λ<sub>max</sub> (nm) 423 (Soret band), 512, 550, 587, 628 (Q bands);

**Fluorescence** (CH<sub>2</sub>Cl<sub>2</sub>, λ<sub>ex</sub> = 431): λ<sub>em</sub>(nm) 607, 648. **MS** (EI+) *m/z* [M]<sup>+</sup> calculated for

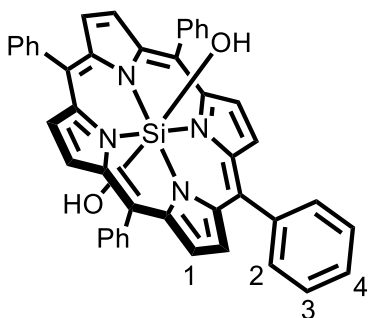
C<sub>76</sub>H<sub>66</sub>N<sub>4</sub>O<sub>2</sub>Si<sub>3</sub> 1150.44, measured 1150.45. **CV** (V vs NHE, ref to Fc/Fc<sup>+</sup>) -1.105, 1.345.



**1i:** In a 50 mL round-bottom flask with a magnetic stir bar, **3** (100 mg, 0.15 mmol) was dissolved in 1,2-dichloroethane (10 mL) to which Et<sub>3</sub>N (50  $\mu$ L g, 0.37 mmol) was added. The reaction mixture was stirred for 5 min, followed by the addition of triphenylchlorosilane (109 mg, 0.37 mmol). The reaction mixture was refluxed overnight and monitored by TLC. Upon completion, the reaction mixture was concentrated *in vacuo* and the residue was purified using a short silica plug (petroleum ether:Et<sub>2</sub>O:Et<sub>3</sub>N, 5:2:1), R<sub>f</sub> = 0.63. The filtrate was then triturated using cold EtOH until no further precipitation occurred. The solid was filtered through a sintered glass funnel which was then dried under vacuum to yield **1i** as a purple solid (150 mg, 0.13 mmol, 85%). **<sup>1</sup>H NMR** (400 MHz, CDCl<sub>3</sub>)  $\delta$  8.65 (s, 8H, H<sub>1</sub>), 7.68 – 7.63 (tt, *J* = 7.7, 1.3 Hz, 4H, H<sub>4</sub>), 7.55 (t, *J* = 7.6 Hz, 8H, H<sub>3</sub>), 7.39 (dd, *J* = 8.1, 1.2 Hz, 8H, H<sub>2</sub>), 6.84 (tt, *J* = 7.4, 1.4 Hz, 6H, H<sub>7</sub>), 6.53 (t, *J* = 7.6 Hz, 12H, H<sub>6</sub>), 4.67 – 4.59 (dd, *J* = 7.6, 1.2 Hz, 12H, H<sub>5</sub>). **<sup>13</sup>C NMR** (101 MHz, CDCl<sub>3</sub>)  $\delta$  117.9, 126.4, 126.5, 127.6, 127.8, 130.9, 132.9, 143.6, 140.8, 134.4, 132.9, 130.9, 127.8, 127.6, 126.5, 126.4, 117.9. **IR** (cm<sup>-1</sup>) 3049, 1596, 1490, 1355, 1207, 1104, 1060, 1009, 852, 798, 745, 697. **UV-Vis** (CH<sub>2</sub>Cl<sub>2</sub>):  $\lambda_{\text{max}}$  (nm) 425 (Soret band), 515, 553, 592, 633 (Q bands); **Fluorescence** (CH<sub>2</sub>Cl<sub>2</sub>,  $\lambda_{\text{ex}}$  = 427):  $\lambda_{\text{em}}$  (nm) 602, 645. **HRMS-ASAP** *m/z* [M+H]<sup>+</sup> calculated for C<sub>80</sub>H<sub>59</sub>N<sub>4</sub>O<sub>2</sub>Si<sub>3</sub> 1191.3945, measured 1191.3917. **CV** (V vs NHE, ref to Fc/Fc<sup>+</sup>) - 1.128, 1.340.



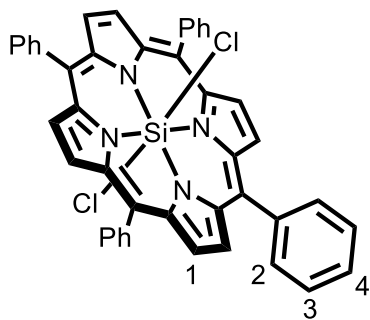
**2:** In a 250 mL round-bottom flask with a magnetic stir bar, benzaldehyde (1.74 g, 16.4 mmol) was added into propionic acid (30 mL). The mixture was heated to reflux for 15 min. Pyrrole (1.00 g, 14.9 mmol) was added dropwise to the reaction mixture over a period of 5 min. The reaction mixture was then refluxed for 1 h. The reaction mixture was allowed to cool to rt and then MeOH (40 mL) was poured into the flask. The mixture was stirred at rt overnight. The crude solid was isolated by vacuum filtration and was washed with hot MeOH yield **2** as a fine, purple solid (0.62 g, 1.00 mmol, 27%). **<sup>1</sup>H NMR** (400 MHz, CDCl<sub>3</sub>) δ 8.86 (s, 8H, H<sub>1</sub>), 8.23 (d, 8H, H<sub>2</sub>), 7.77 (m, 12H, H<sub>3</sub>, H<sub>4</sub>), -2.74 (s, 2H, H<sub>5</sub>). **<sup>13</sup>C NMR** (101 MHz, CDCl<sub>3</sub>) δ 142.4, 134.8, 131.4 (br), 127.9, 126.9, 120.4. **UV-Vis** (CH<sub>2</sub>Cl<sub>2</sub>): λ<sub>max</sub> (nm) 417 (Soret band), 514, 549, 590, 646 (Q bands). **Fluorescence** (CH<sub>2</sub>Cl<sub>2</sub>): λ<sub>em</sub> (nm) 650, 719. Spectroscopic data are consistent with those reported previously.<sup>1</sup>



**3:** In a 50 mL round-bottom flask with a magnetic stir bar, **4** (100 mg, 0.14 mmol) was dissolved in THF (15 ml) and distilled H<sub>2</sub>O (5 mL). The reaction mixture was refluxed for 2 h, monitoring the conversion of starting material by TLC. Upon completion, the reaction mixture was washed with a saturated aqueous solution of NaHCO<sub>3</sub> (30 mL) followed by brine (30 mL). The organic layers were dried over MgSO<sub>4</sub>, filtered and concentrated *in vacuo* to yield **3** as a purple solid (95 mg, 0.14 mmol, 98%). **<sup>1</sup>H NMR** (400 MHz, CDCl<sub>3</sub>) δ 8.85 (s, 8H, H<sub>1</sub>), 8.23 (d, 8H, H<sub>2</sub>), 7.76 (m, 12H, H<sub>3</sub>, H<sub>4</sub>). **<sup>13</sup>C NMR** (101MHz, CDCl<sub>3</sub>) δ 142.5, 134.9, 128.0, 127.0, 120.4. **IR** (cm<sup>-1</sup>) 2918, 2852, 2322, 2102, 2079, 1891, 1595, 1526, 1489, 1439, 1353, 1204, 1071, 1007, 828, 800, 750, 698. **UV-Vis** (CH<sub>2</sub>Cl<sub>2</sub>): λ<sub>max</sub> (nm) 418



446, (Soret band), 446, 514, 550, 590, 649 (Q bands). **Fluorescence** (CH<sub>2</sub>Cl<sub>2</sub>):  $\lambda_{em}$  (nm)  
Spectroscopic data are consistent with those reported previously.<sup>2</sup>



**TPP-SiCl<sub>2</sub>**: In a 250 mL round-bottom flask with a magnetic stir bar, **2** (100 mg, 0.16 mmol) was dissolved in anhydrous CH<sub>2</sub>Cl<sub>2</sub> (100 mL). Et<sub>3</sub>N (36.2 mg, 0.358 mmol) was added and the mixture was stirred for 5 min. Next, trichlorosilane (26 mg, 0.20 mmol) was added and the reaction was stirred at rt for 24 h. The mixture was cooled to 0 °C and quenched by adding H<sub>2</sub>O (10 mL). The reaction mixture was washed with a saturated aqueous solution of NaHCO<sub>3</sub> (2 × 50 mL) followed by brine (50 mL). The organic layer was dried over MgSO<sub>4</sub>, filtered and concentrated *in vacuo* to yield **TPP-SiCl<sub>2</sub>** as a purple solid (99 mg, 0.14 mmol, 85%). **<sup>1</sup>H NMR** (400 MHz, CDCl<sub>3</sub>)  $\delta$  8.93 (s, 8H, H<sub>1</sub>), 8.14 (m, 8H, H<sub>2</sub>), 7.74 (m, 12H, H<sub>3</sub>, H<sub>4</sub>). **<sup>13</sup>C NMR** (101MHz, CDCl<sub>3</sub>)  $\delta$  117.7, 127.2, 128.1, 131.8, 134.3, 140.6, 143.5. Spectroscopic data are consistent with those reported previously.<sup>3</sup>

### 3. $^1\text{H}$ , $^{13}\text{C}$ , and Variable-Temperature NMR Spectroscopic Characterization of Synthesized Compounds

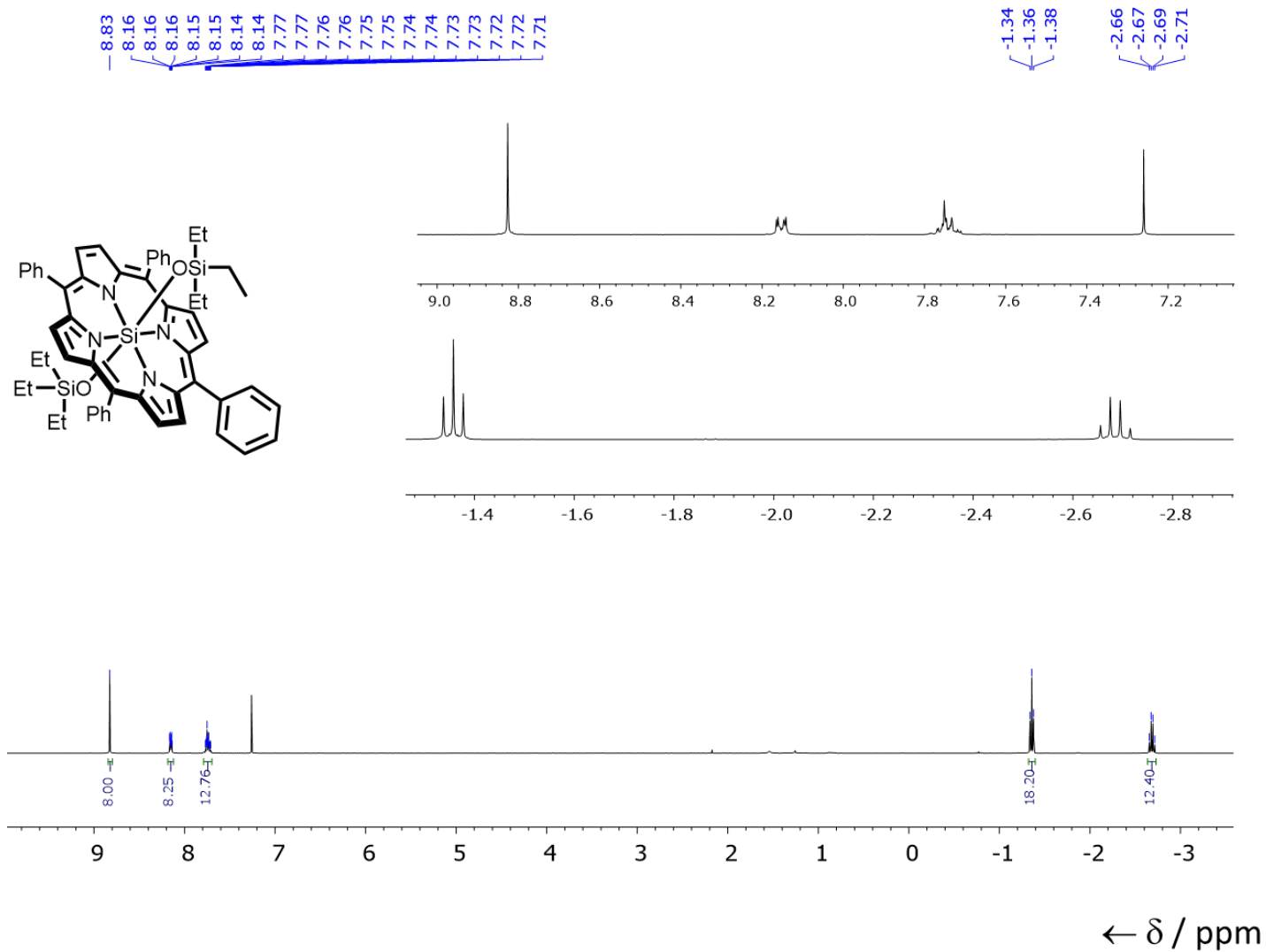


Figure S1.  $^1\text{H}$  NMR spectrum of **1a** (400 MHz,  $\text{CDCl}_3$ , 298 K).

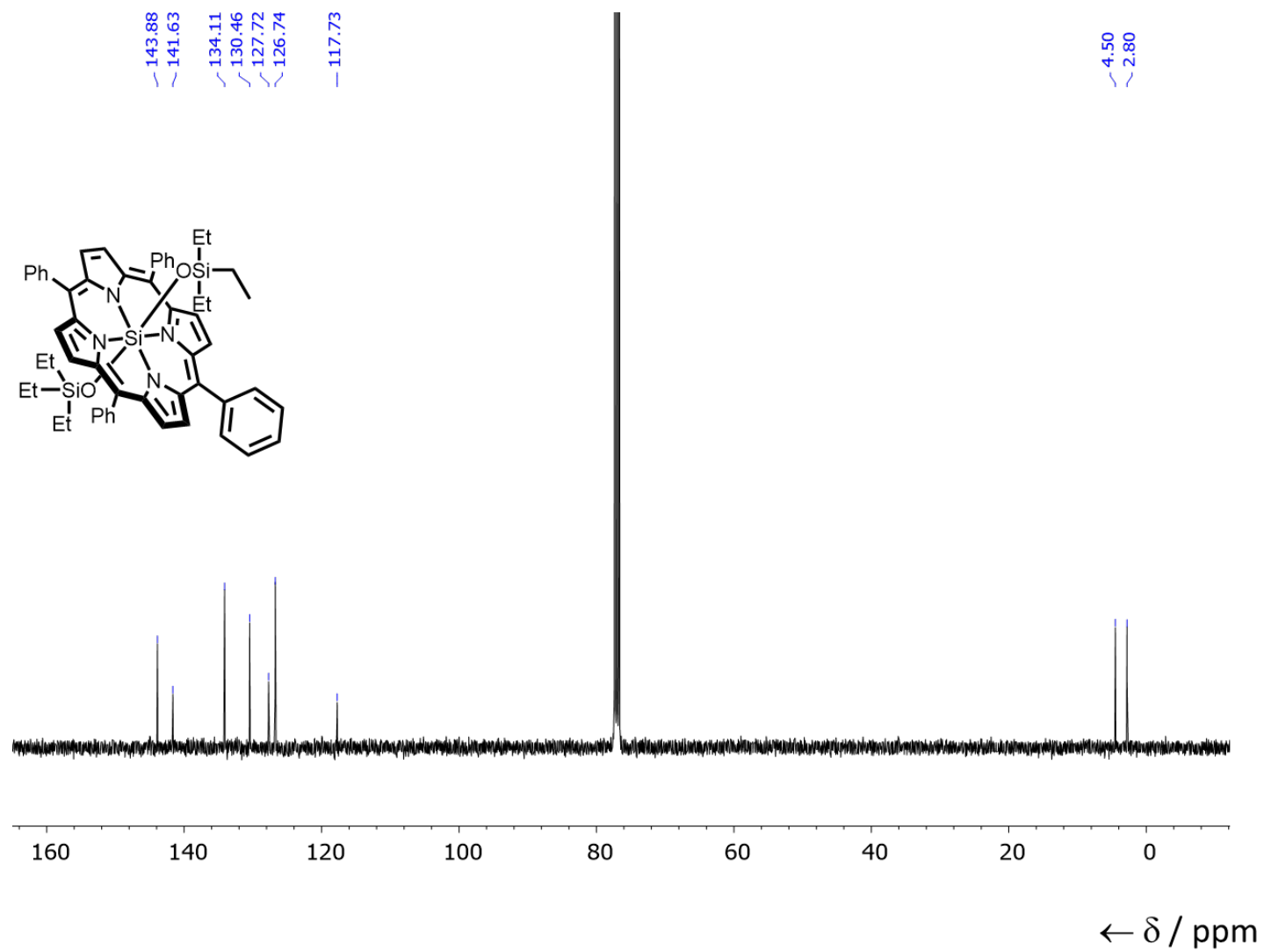


Figure S2. <sup>13</sup>C NMR spectrum of **1a** (101 MHz, CDCl<sub>3</sub>, 298 K).

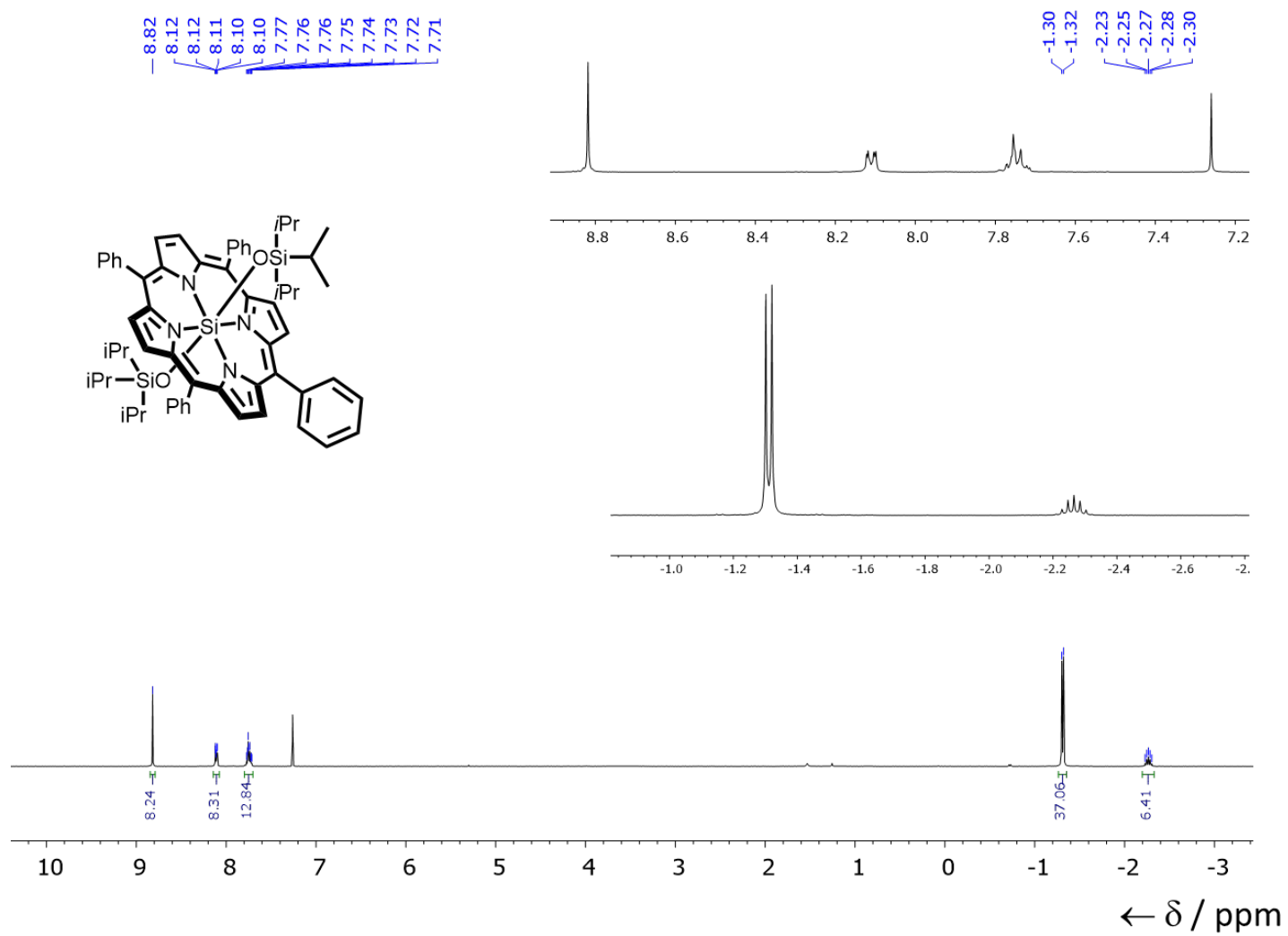


Figure S3.  $^1\text{H}$  NMR spectrum of **1b** (400 MHz,  $\text{CDCl}_3$ , 298 K).

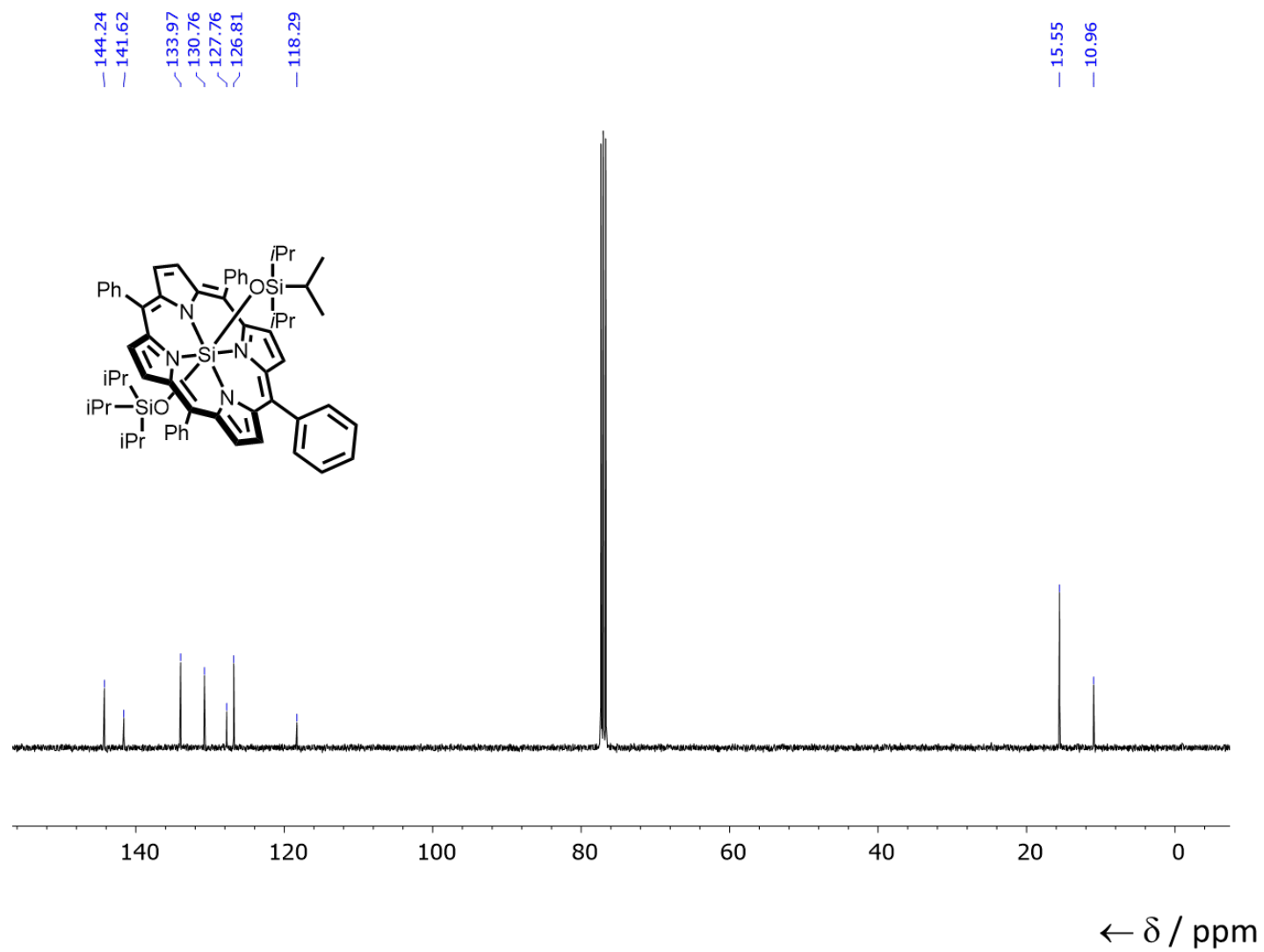
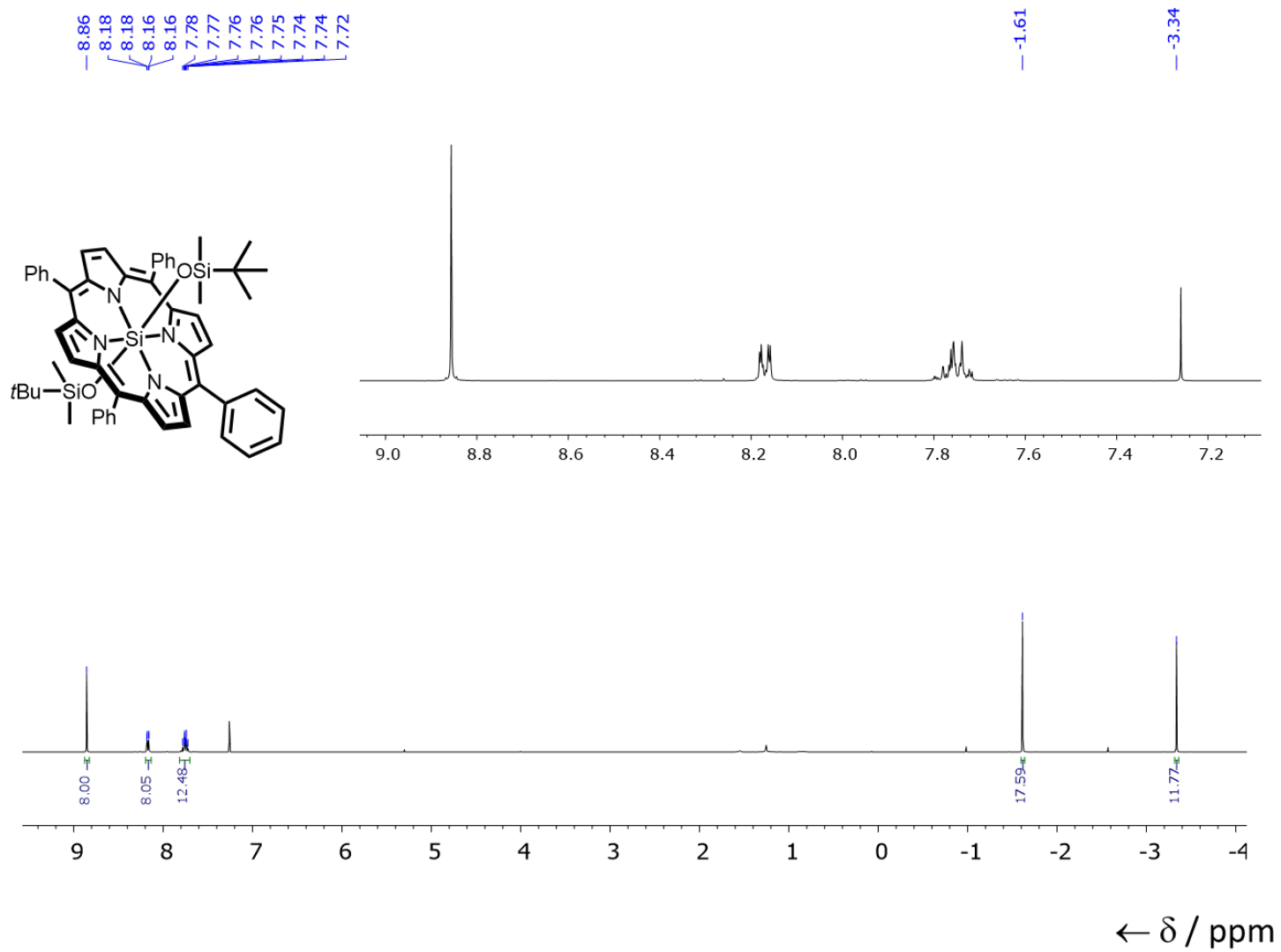


Figure S4. <sup>13</sup>C NMR spectrum of **1b** (101MHz, CDCl<sub>3</sub>, 298 K).



**Figure S5.**  $^1\text{H}$  NMR spectrum of **1c** (400 MHz,  $\text{CDCl}_3$ , 298 K).

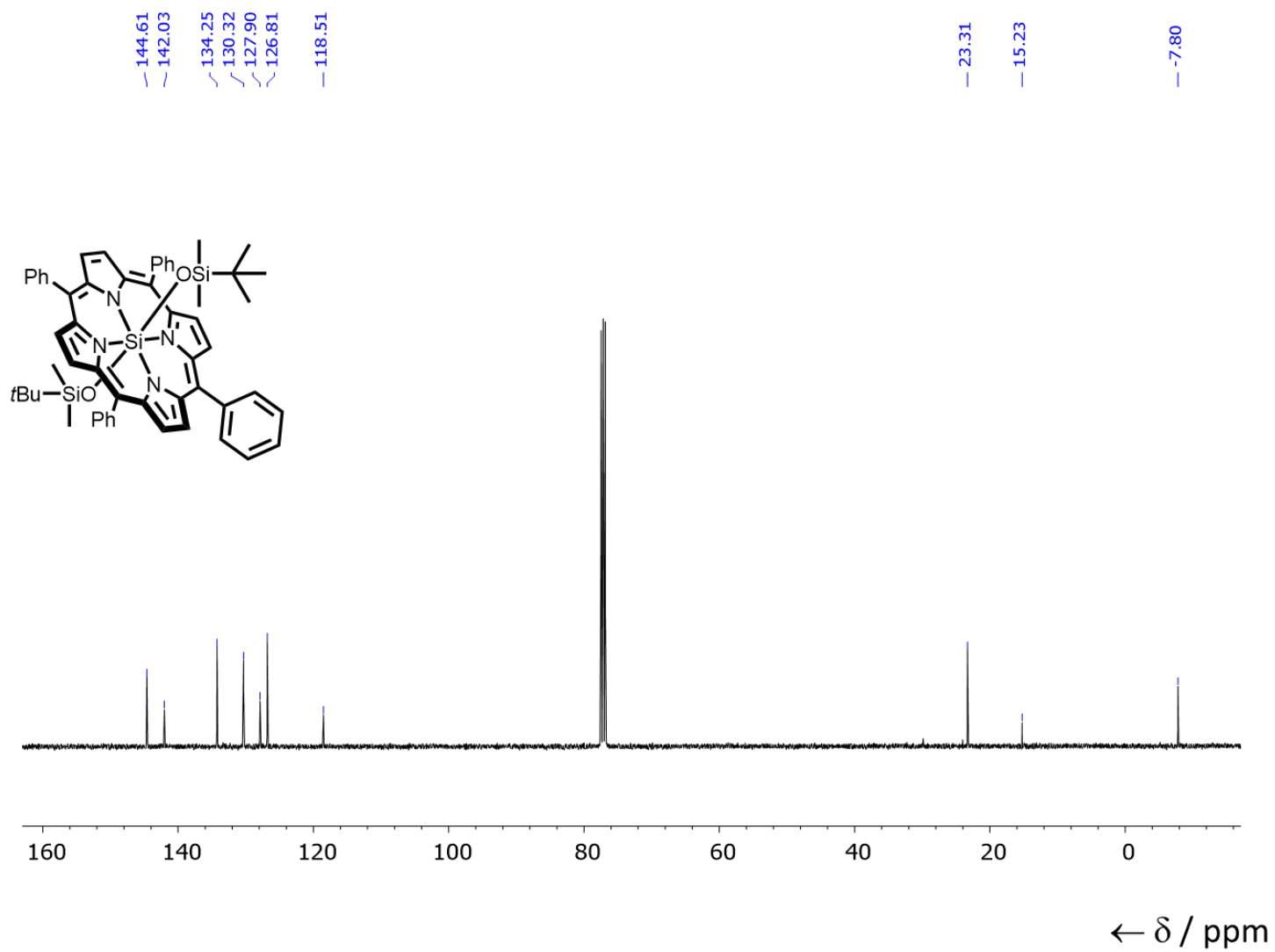
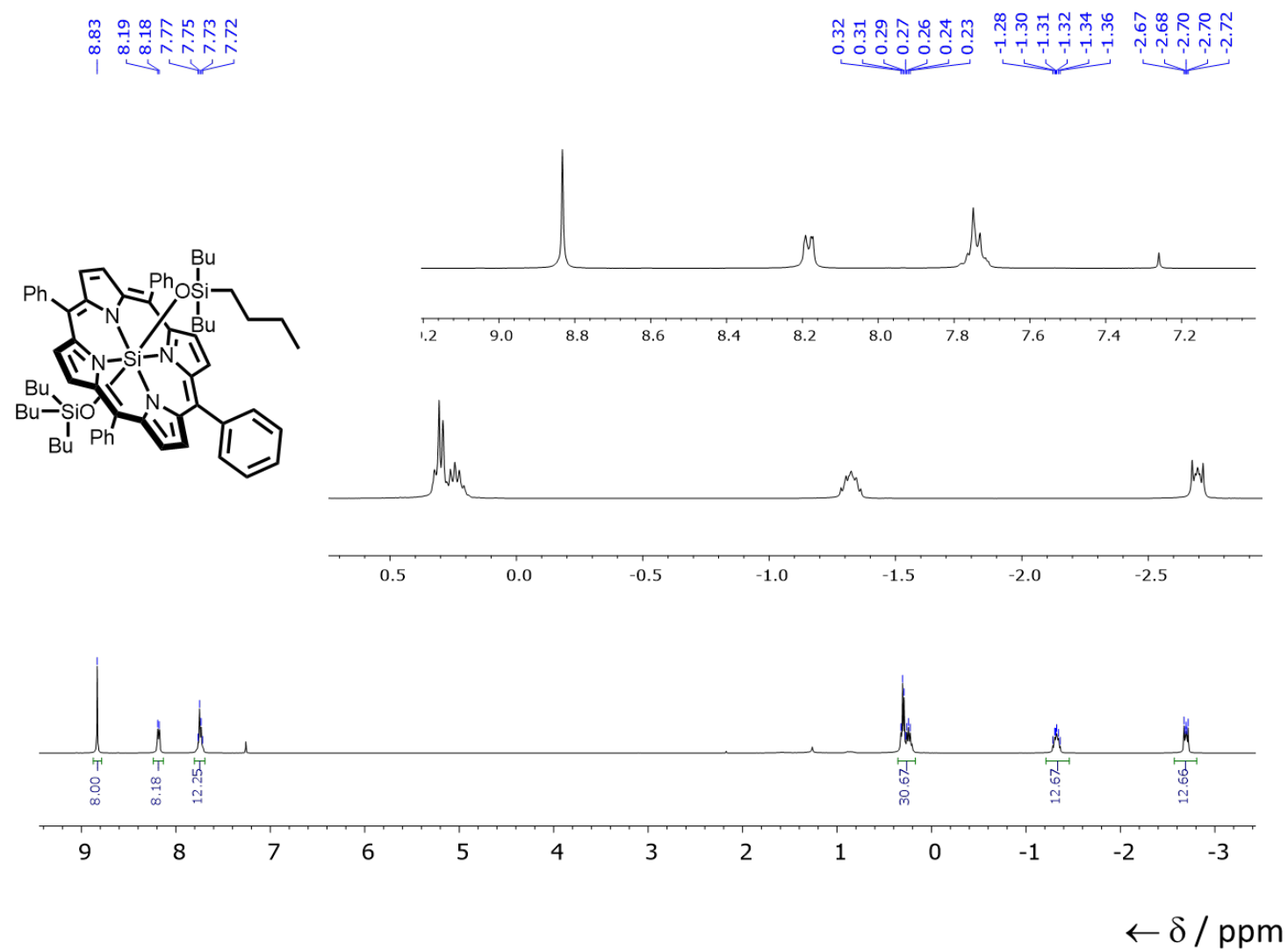
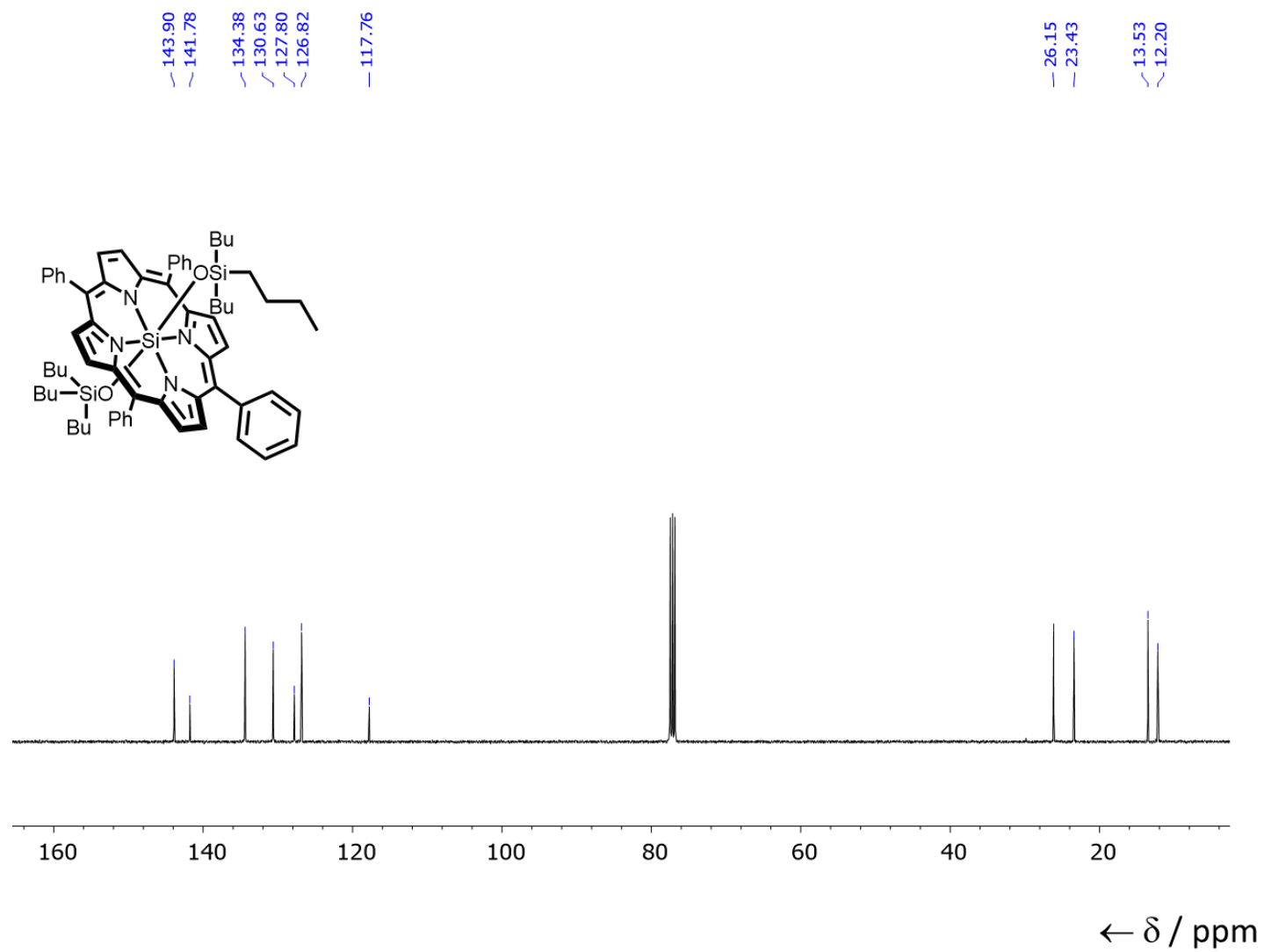


Figure S6. <sup>13</sup>C NMR spectrum of **1c** (101MHz, CDCl<sub>3</sub>, 298 K).



**Figure S7.**  $^1\text{H}$  NMR spectrum of **1d** (400 MHz,  $\text{CDCl}_3$ , 298 K).





**Figure S8.**  $^{13}\text{C}$  NMR spectrum of **1d** (101 MHz,  $\text{CDCl}_3$ , 298 K).

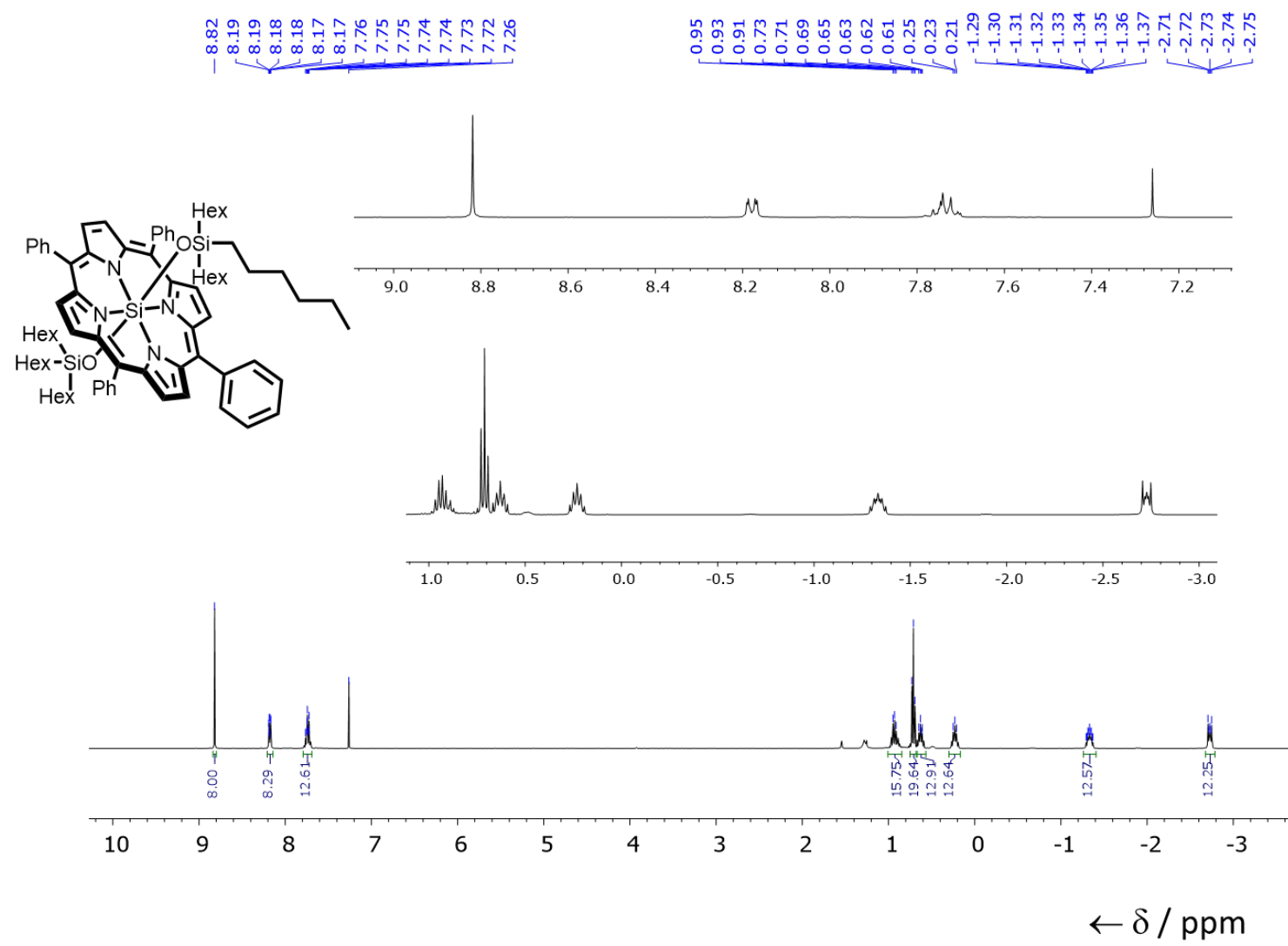
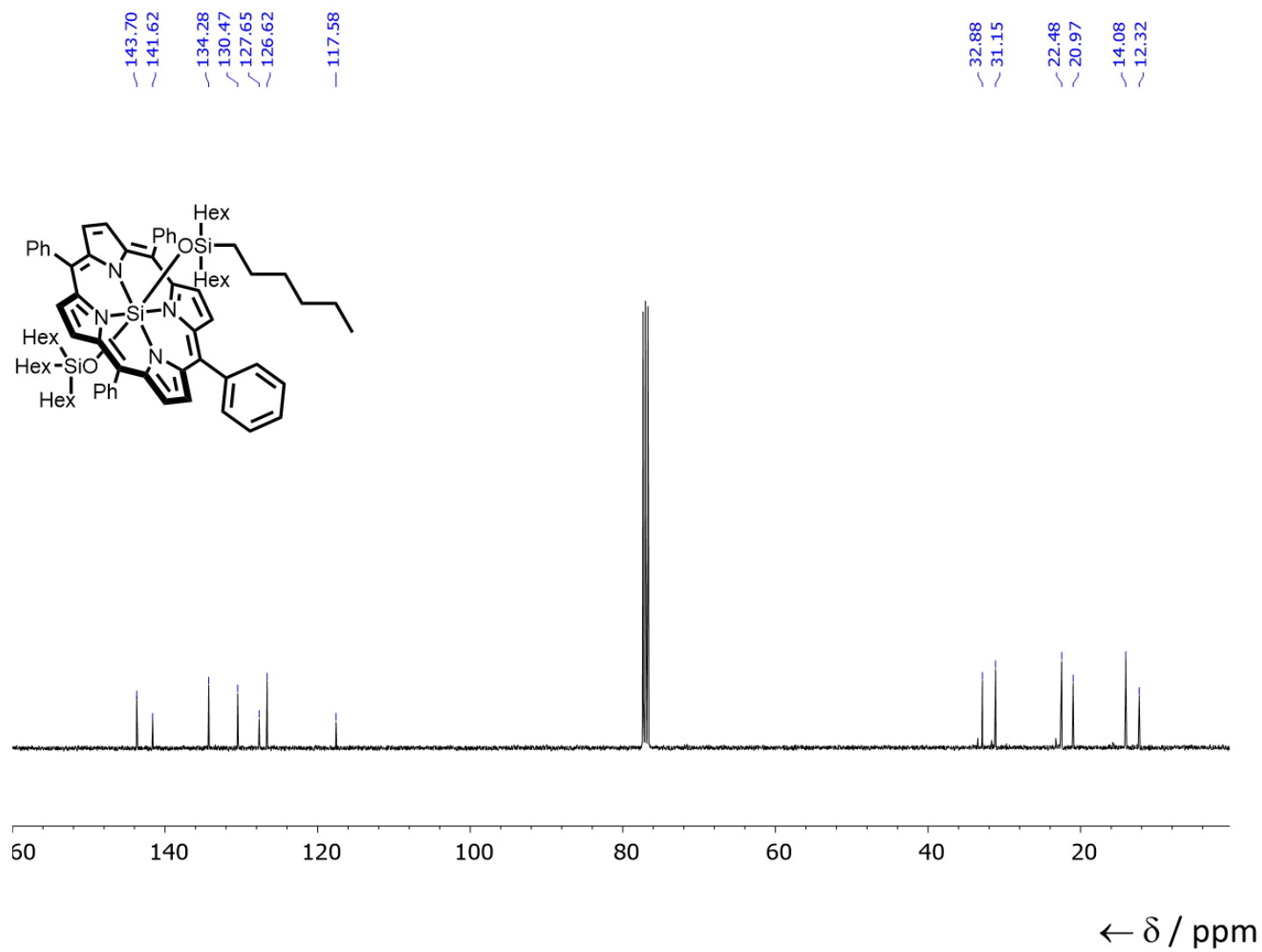
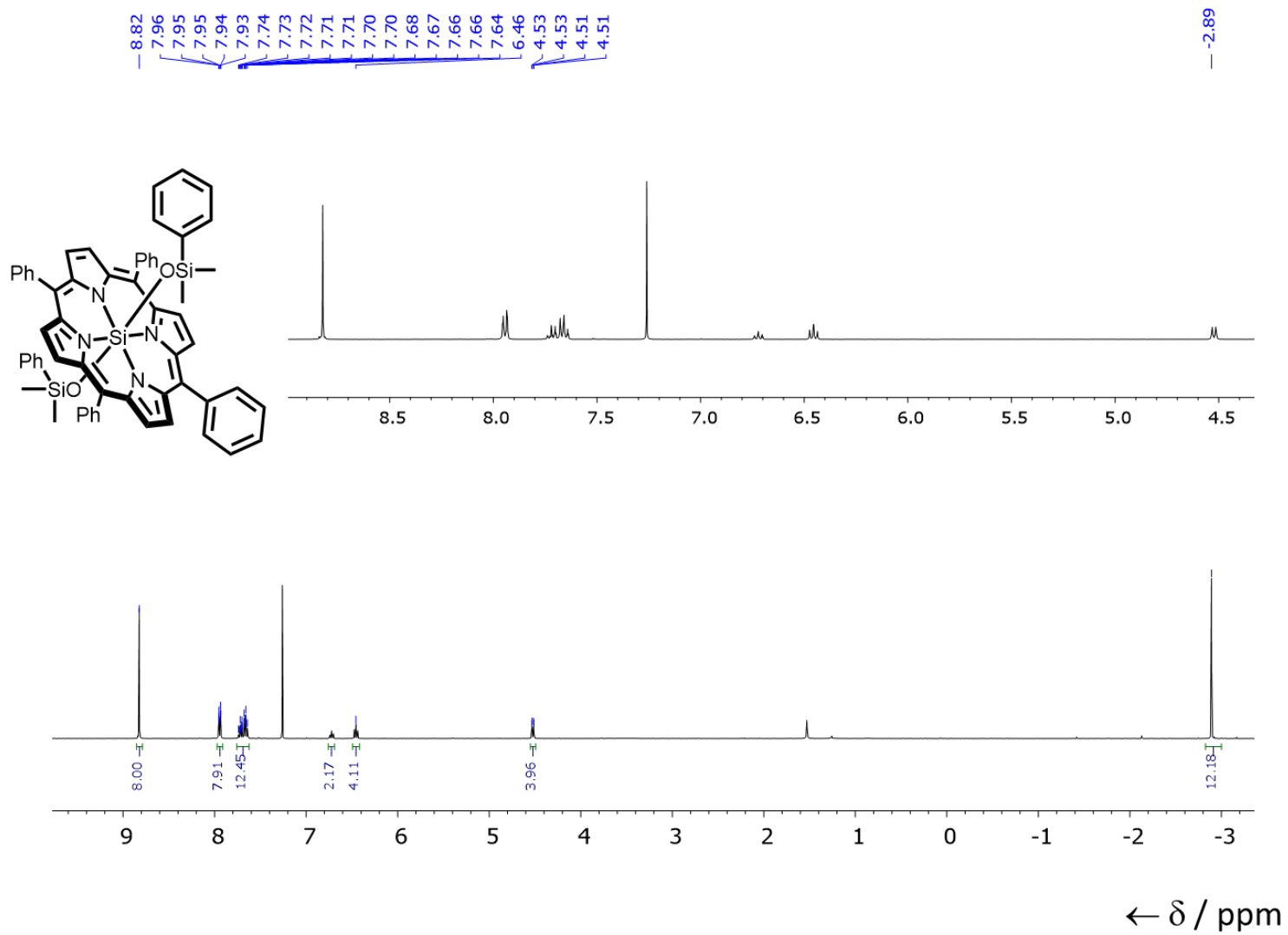


Figure S9.  $^1\text{H}$  NMR spectrum of **1e** (400 MHz,  $\text{CDCl}_3$ , 298 K).



**Figure S10.**  $^{13}\text{C}$  NMR spectrum of **1e** (101 Hz,  $\text{CDCl}_3$ , 298 K).



**Figure S11.**  $^1\text{H}$  NMR spectrum of **1f** (400 MHz,  $\text{CDCl}_3$ , 298 K).

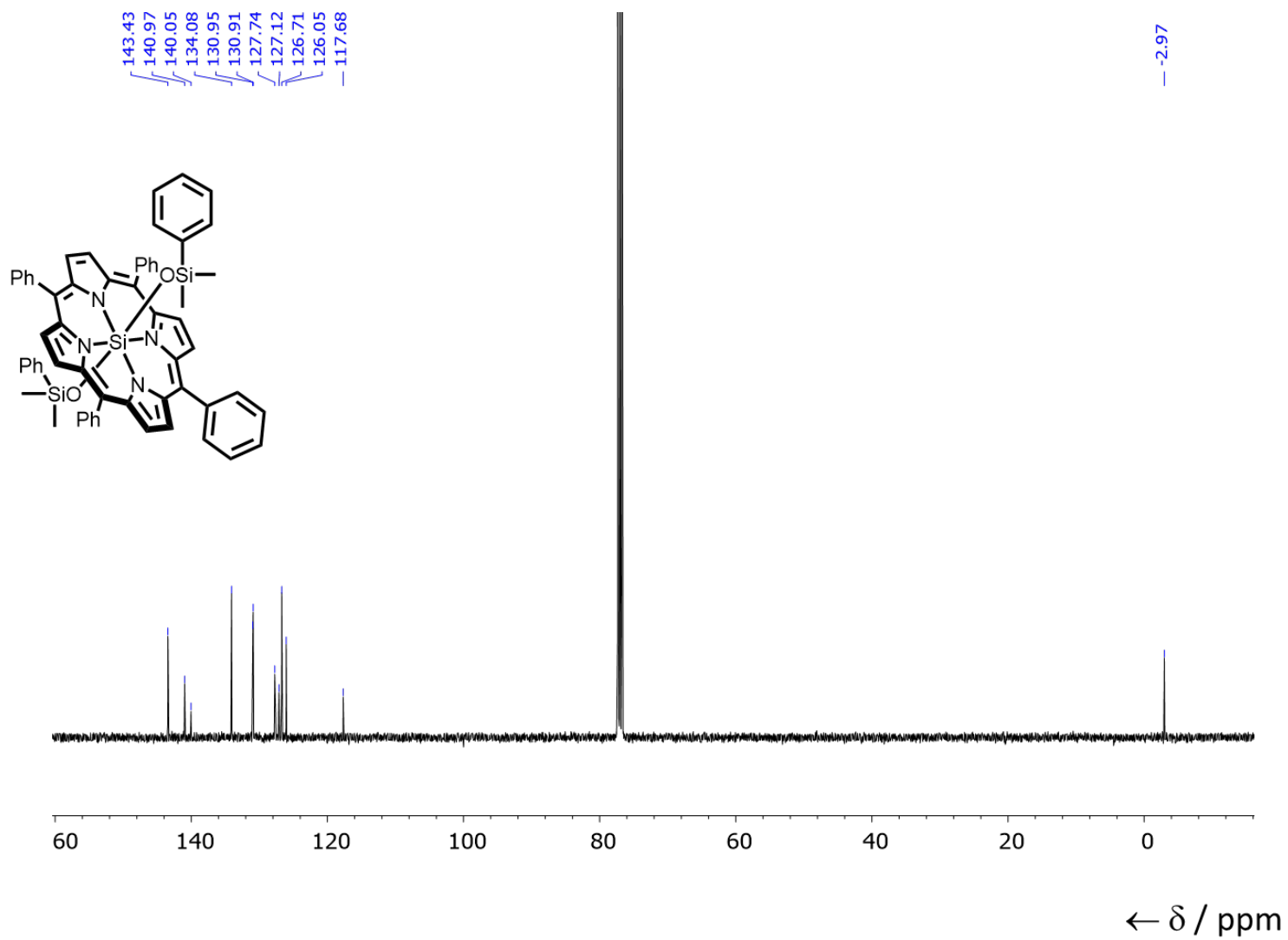


**Figure S12.**  $^{13}\text{C}$  NMR spectrum of **1f** (101MHz,  $\text{CDCl}_3$ , 298 K).

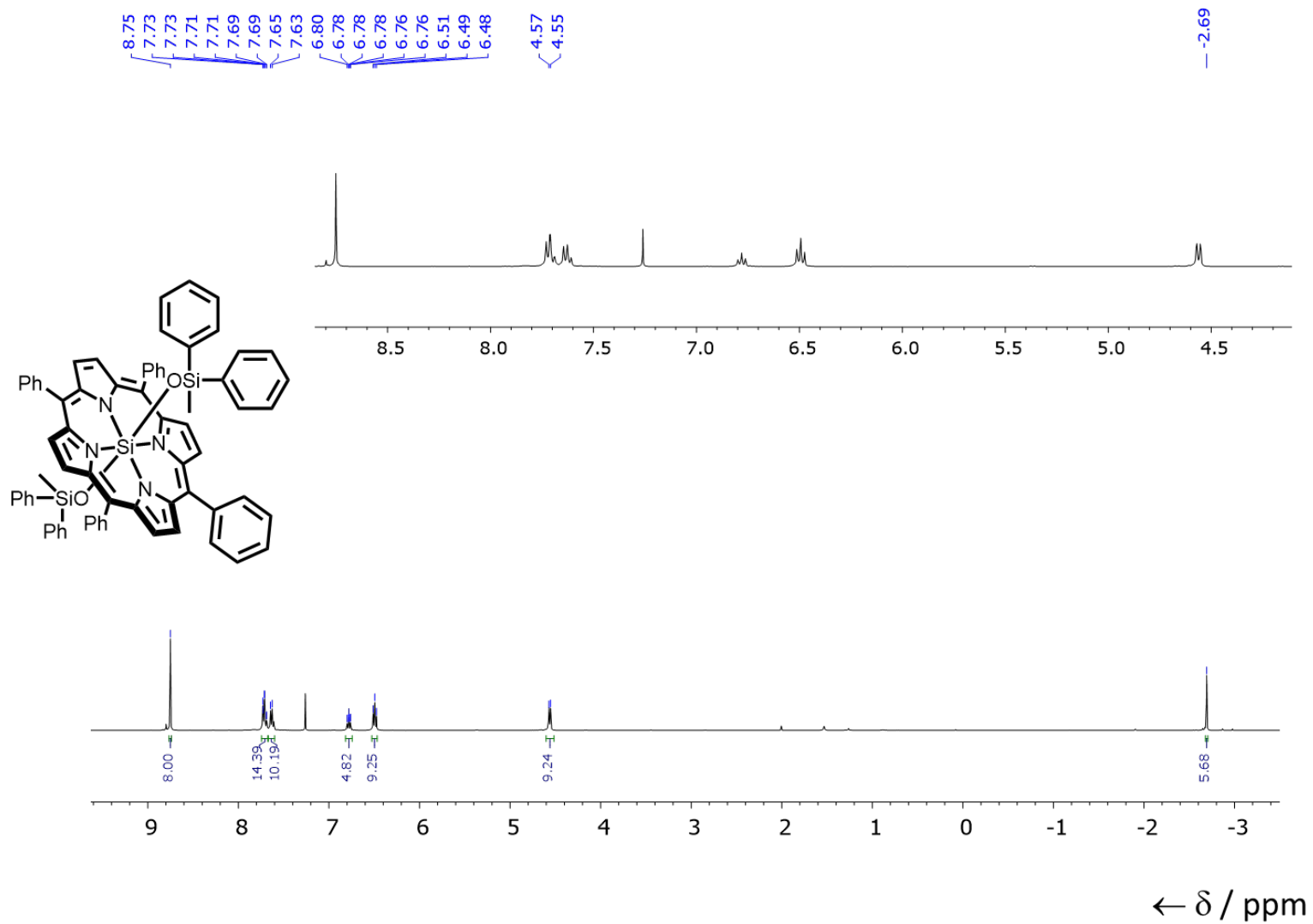
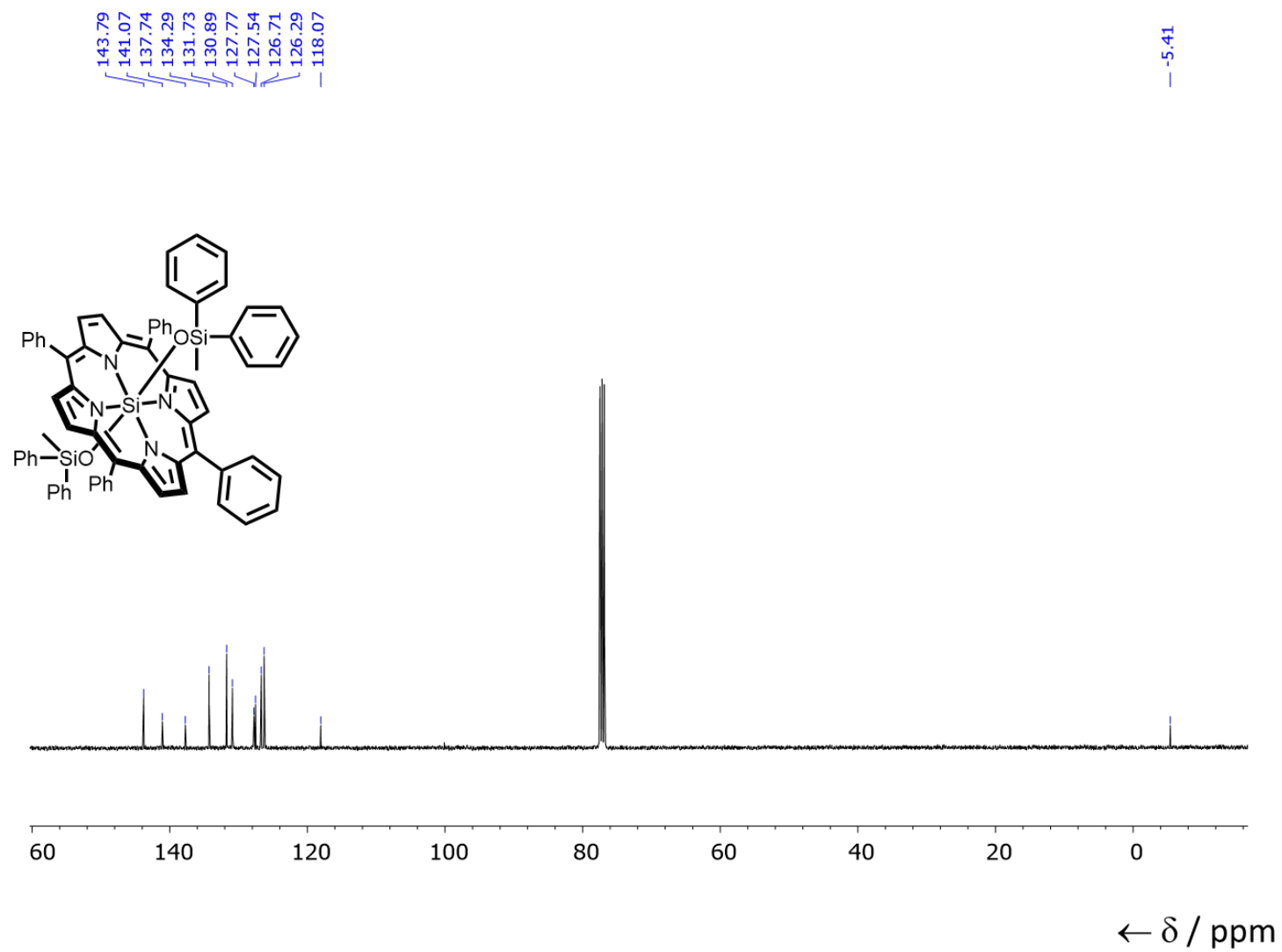
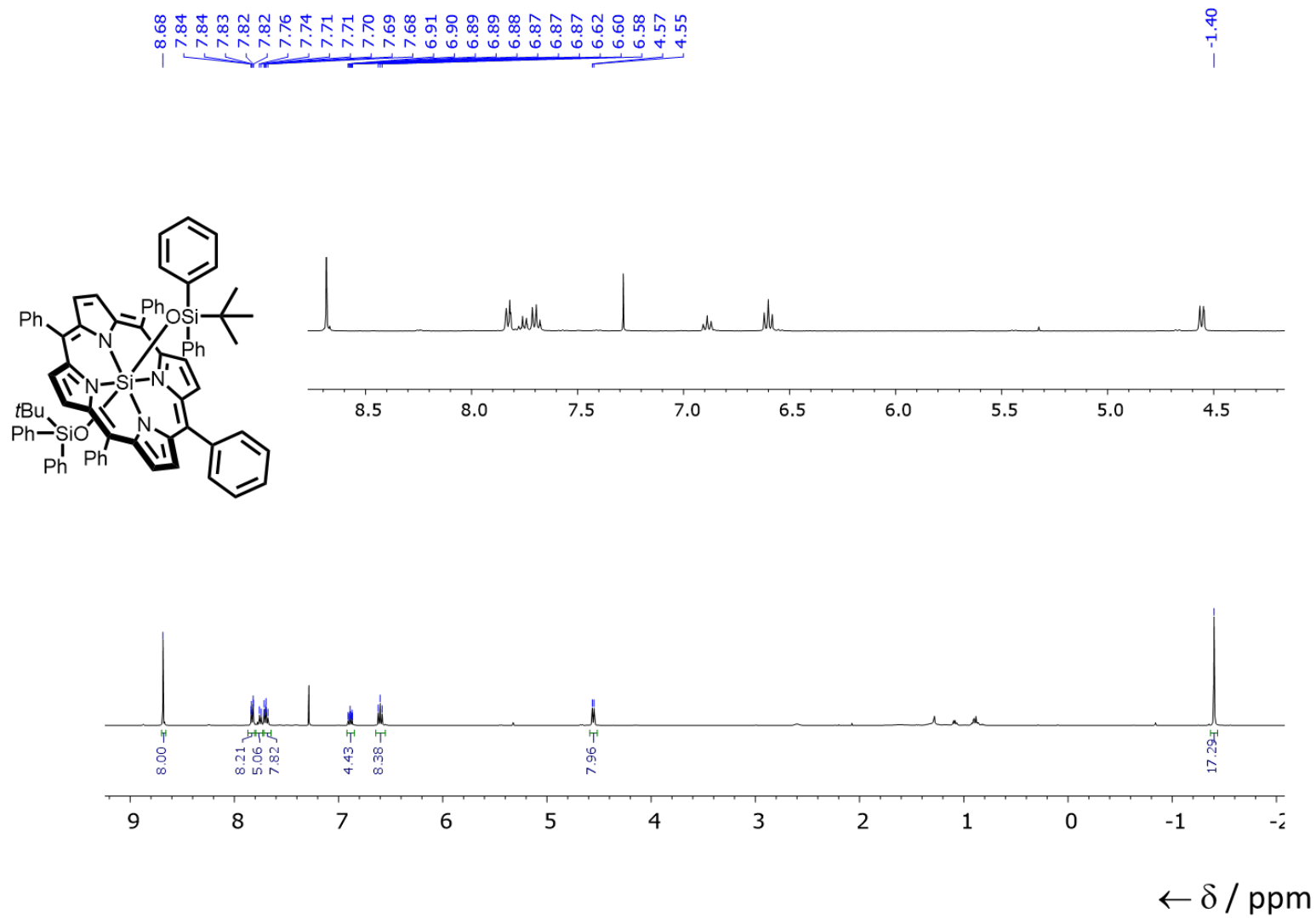


Figure S13. <sup>1</sup>H NMR spectrum of **1g** (400 MHz, CDCl<sub>3</sub>, 298 K).



**Figure S14.**  $^{13}\text{C}$  NMR spectrum of **1g** (101 MHz,  $\text{CDCl}_3$ , 298 K).



**Figure S15.**  $^1\text{H}$  NMR spectrum of **1h** (400 MHz,  $\text{CDCl}_3$ , 298 K).



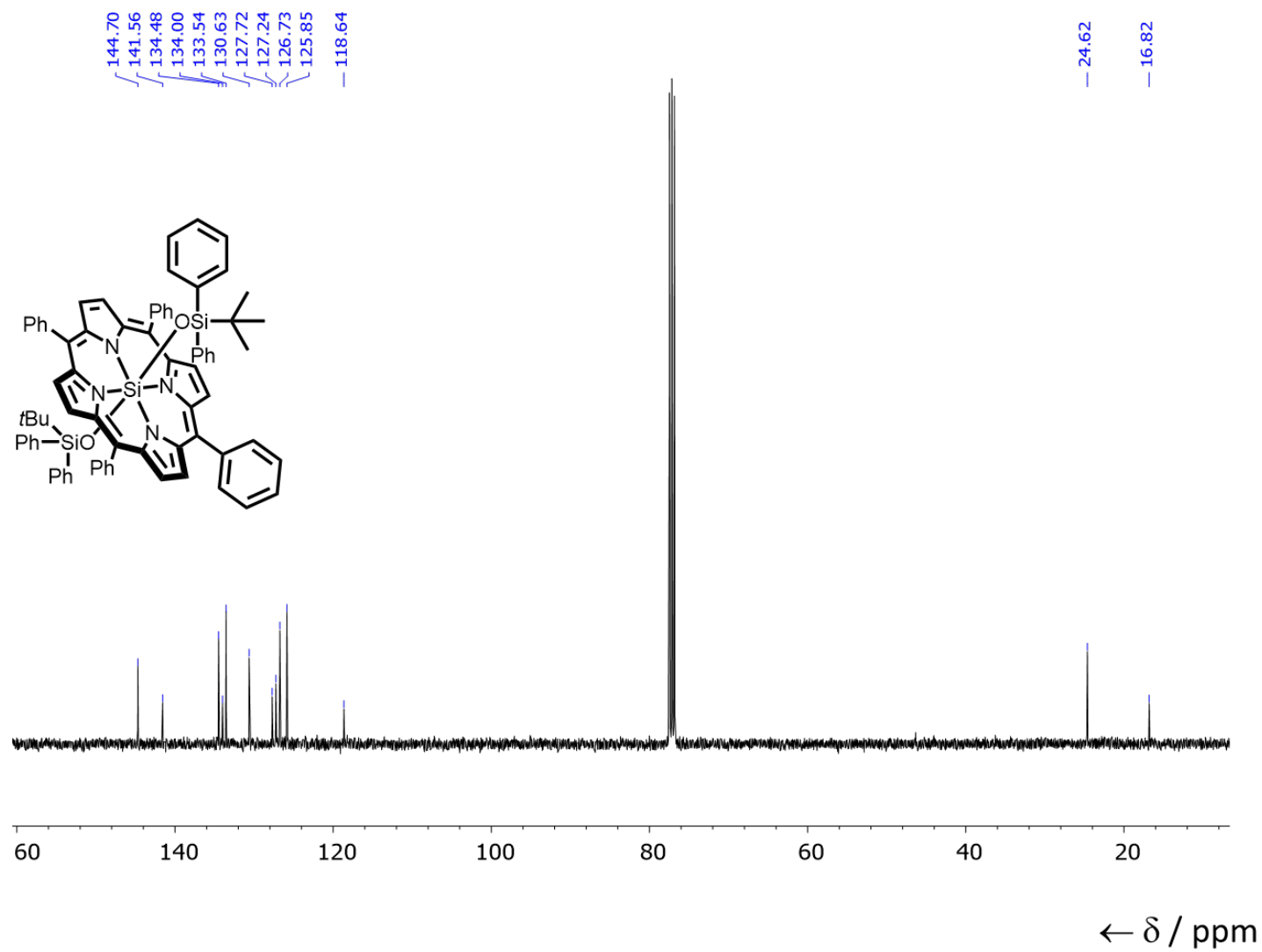


**Figure S16.** <sup>13</sup>C NMR spectrum of **1h** (101 MHz, CDCl<sub>3</sub>, 298 K).

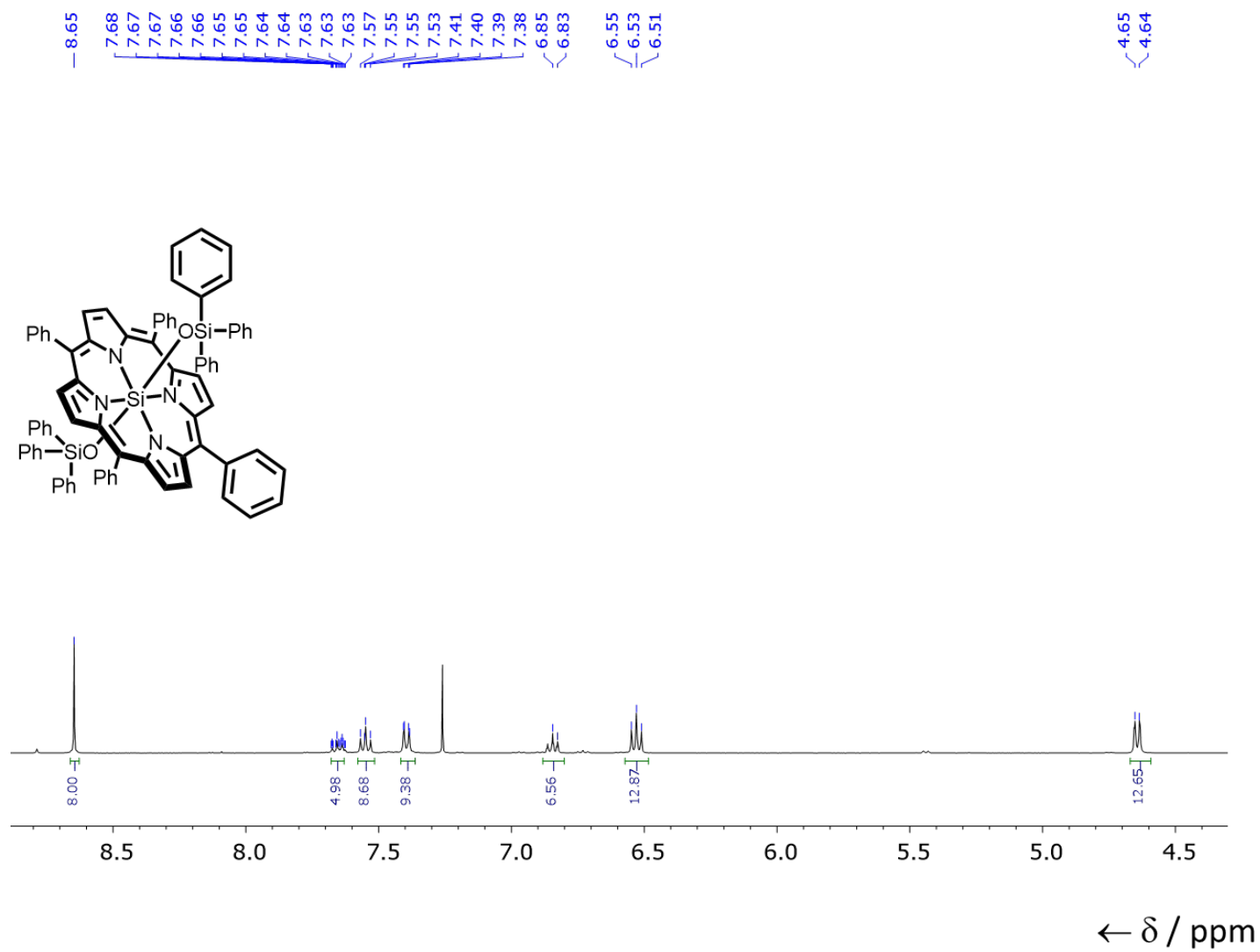
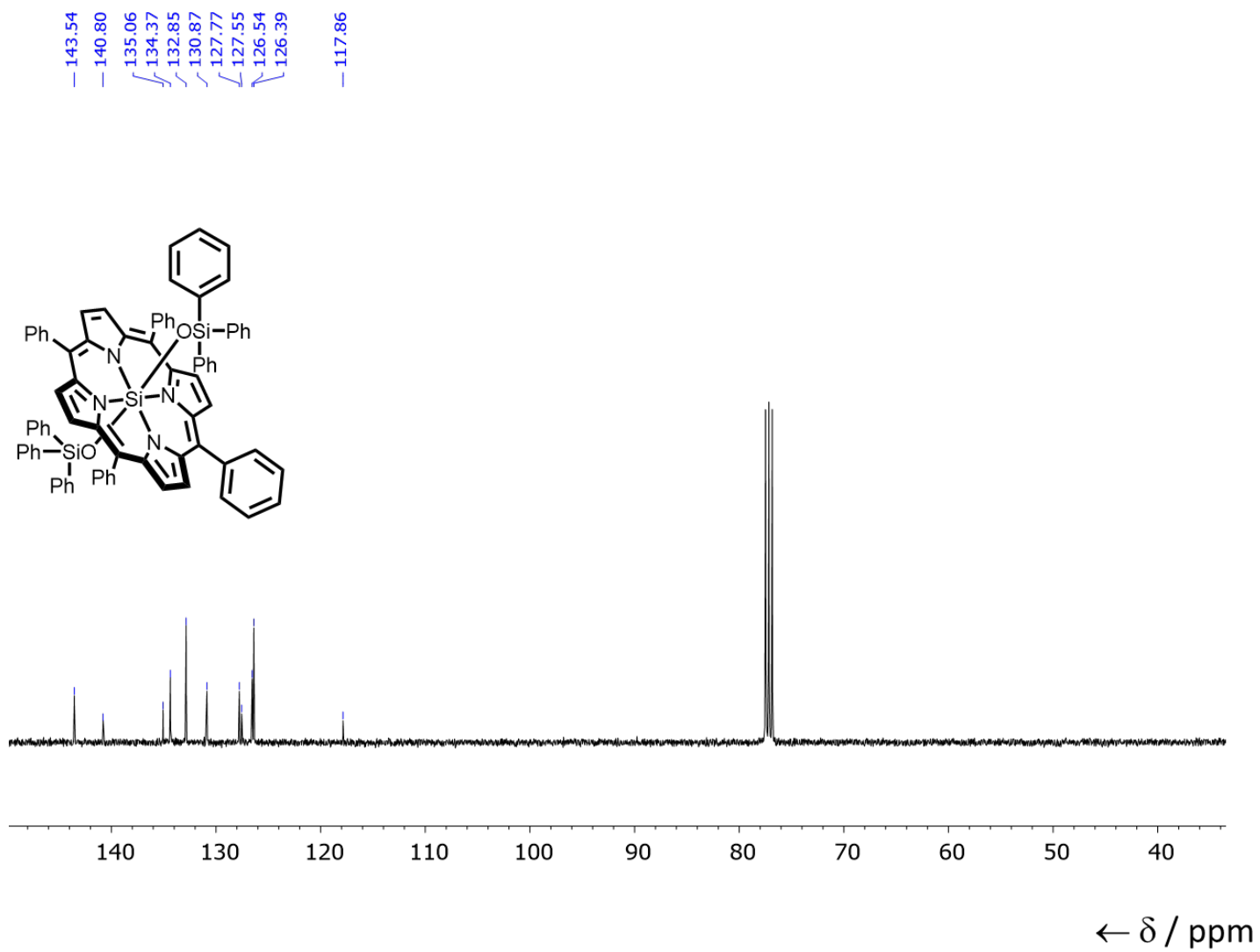


Figure S17. <sup>1</sup>H NMR spectrum of **1i** (400 MHz, CDCl<sub>3</sub>, 298 K).



**Figure S18.** <sup>13</sup>C NMR spectrum of **1i** (101MHz, CDCl<sub>3</sub>, 298 K).

### 3.1. Variable-Temperature (VT) NMR Spectroscopy

(Metallo)porphyrins are known to exhibit a variety of conformational dynamics in solution, and the dynamic processes associated with porphyrin ligands include macrocyclic inversion *meso*- and *b*-substituent rotation.<sup>4</sup> In order to investigate this phenomenon, we performed VT NMR measurements to determine conformational dynamics of these SOPS. A series of spectra were recorded for a solution (CDCl<sub>2</sub>) of **1f** ranging from 193 K to 298 K.

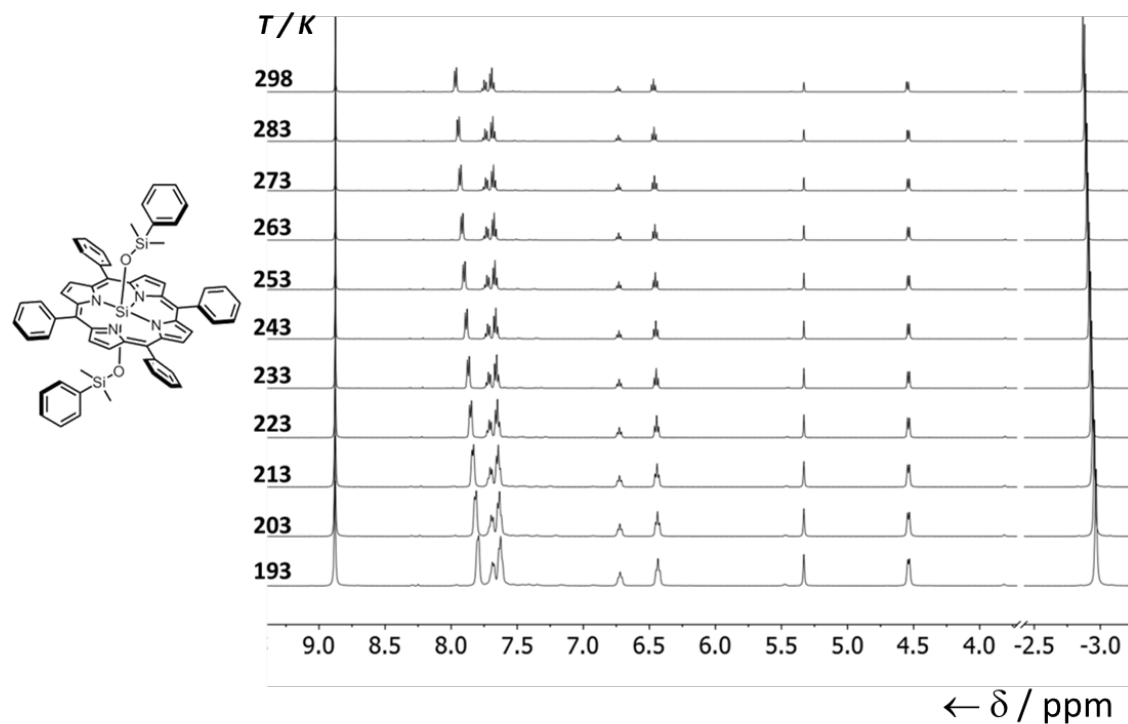
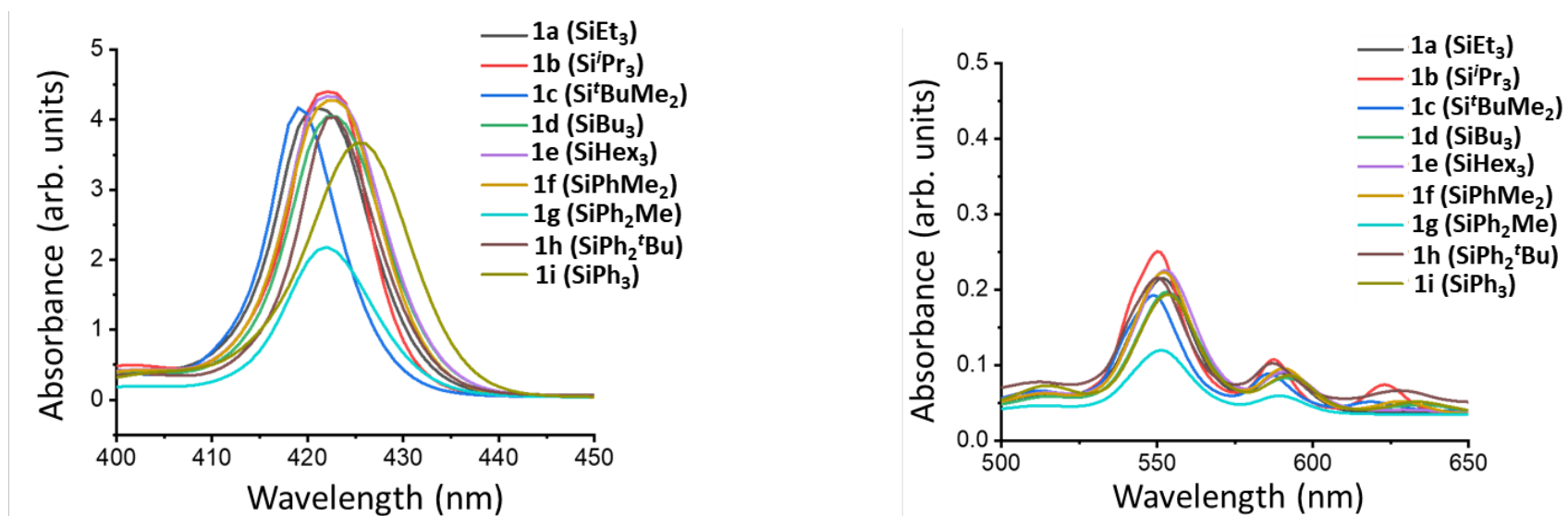


Figure S19. Partial <sup>1</sup>H NMR spectra of **1f**, recorded from 298 K to 193 K.

#### 4. UV-Vis Spectroscopy

The spectra in Figure S20 shows the UV-Vis absorption features of the SOPS (**1a-1i**) in their characteristic Soret band and Q band regions. Spectra were measured in a 10 mm path-length cuvette at room temperature. 10  $\mu$ M Sample concentrations in anhydrous  $\text{CH}_2\text{Cl}_2$  were used for all measurements. The intensities were plotted as absorption (arbitrary units). Concentration effects on the Q band region for compounds (**1a-1i**) are plotted (Figure S21-29) and shows a linear concentration between absorbance and concentration for all compounds, demonstrating no aggregation occurs in solutions at the measured concentrations.



**Figure S20.** UV-Vis spectra of the SOPS (**1a-1i**) a) in the Soret band region and b) in the Q band region.

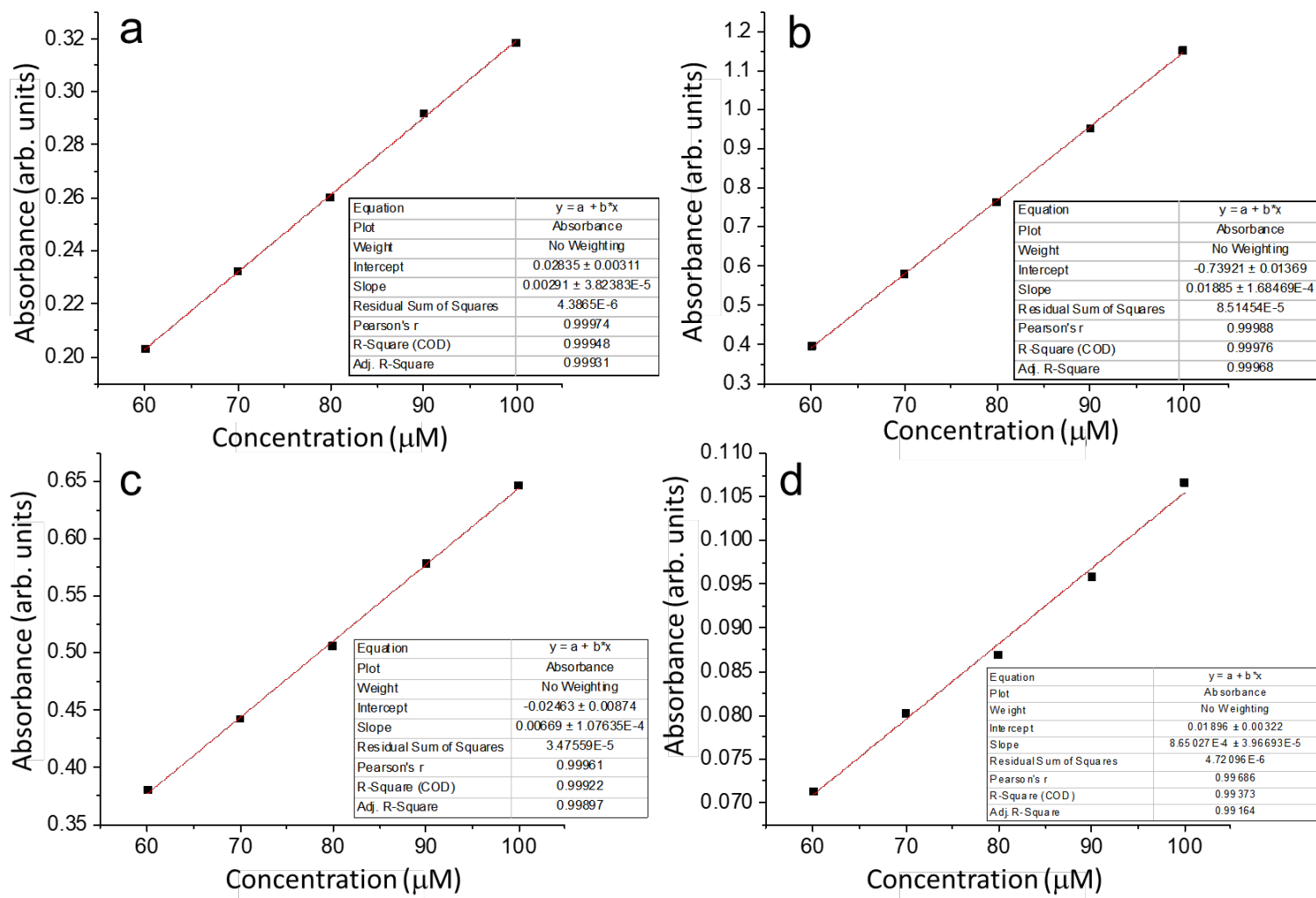


**Figure S21.** Plot of Q band  $\lambda_{\max}$  at different concentrations for compound **1a** in  $\text{CH}_2\text{Cl}_2$ . a)  $\lambda_{\max}$  of Q<sub>1</sub>, b)  $\lambda_{\max}$  of Q<sub>2</sub>, c)  $\lambda_{\max}$  of Q<sub>3</sub>, and d)  $\lambda_{\max}$  of Q<sub>4</sub>.

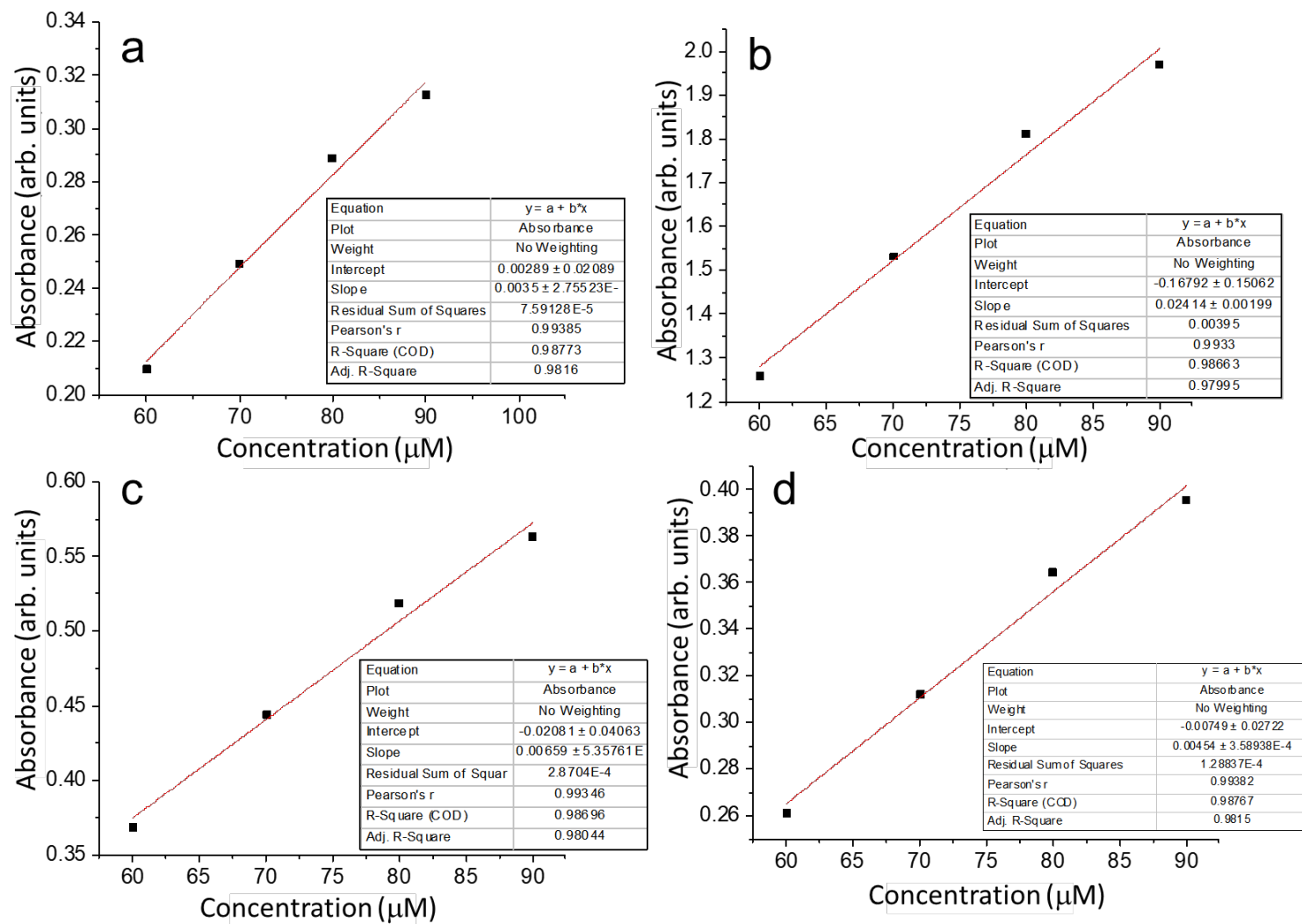


**Figure S22.** Plot of Q band  $\lambda_{\max}$  at different concentrations for compound **1b** in  $\text{CH}_2\text{Cl}_2$ . a)  $\lambda_{\max}$  of Q<sub>1</sub>, b)  $\lambda_{\max}$  of Q<sub>2</sub>, c)  $\lambda_{\max}$  of Q<sub>3</sub>, and d)  $\lambda_{\max}$  of Q<sub>4</sub>.

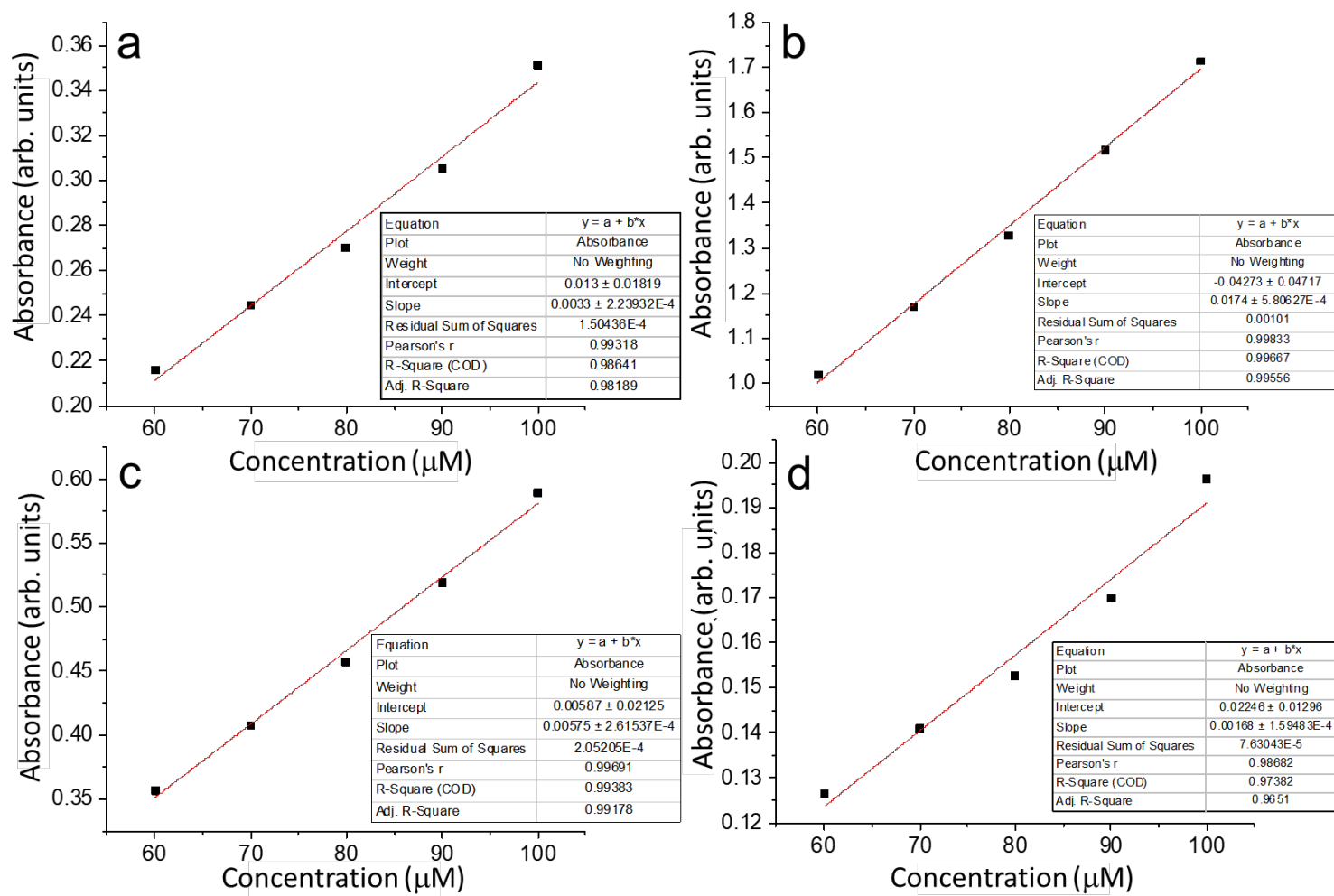


**Figure S23.** Plot of Q band  $\lambda_{\max}$  at different concentrations for compound **1c** in  $\text{CH}_2\text{Cl}_2$ . a)  $\lambda_{\max}$  of  $Q_1$ , b)  $\lambda_{\max}$  of  $Q_2$ , c)  $\lambda_{\max}$  of  $Q_3$ , and d)  $\lambda_{\max}$  of  $Q_4$ .



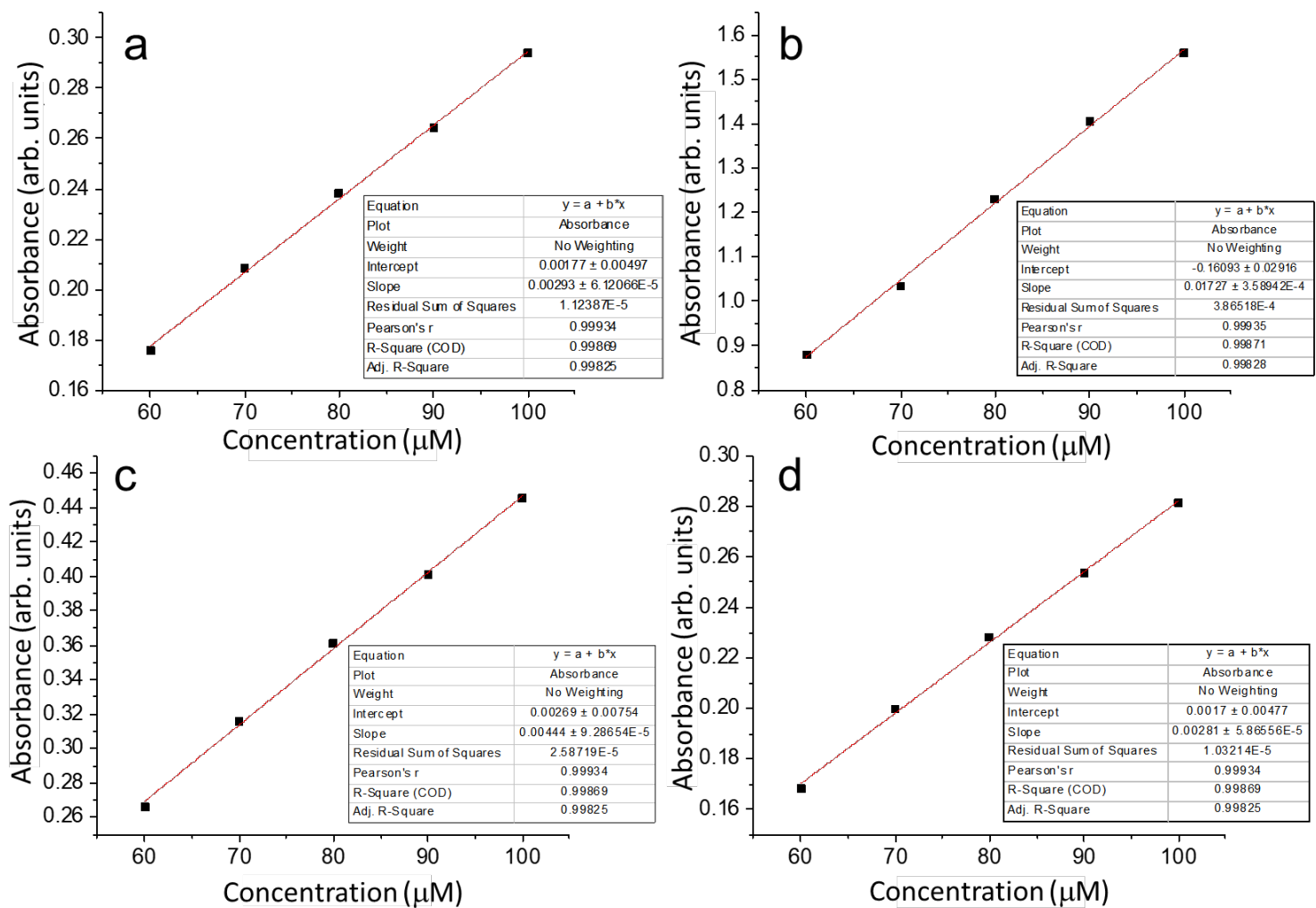


**Figure S24.** Plot of Q band  $\lambda_{\max}$  at different concentrations for compound **1d** in  $\text{CH}_2\text{Cl}_2$ . a)  $\lambda_{\max}$  of  $Q_1$ , b)  $\lambda_{\max}$  of  $Q_2$ , c)  $\lambda_{\max}$  of  $Q_3$ , and d)  $\lambda_{\max}$  of  $Q_4$ .

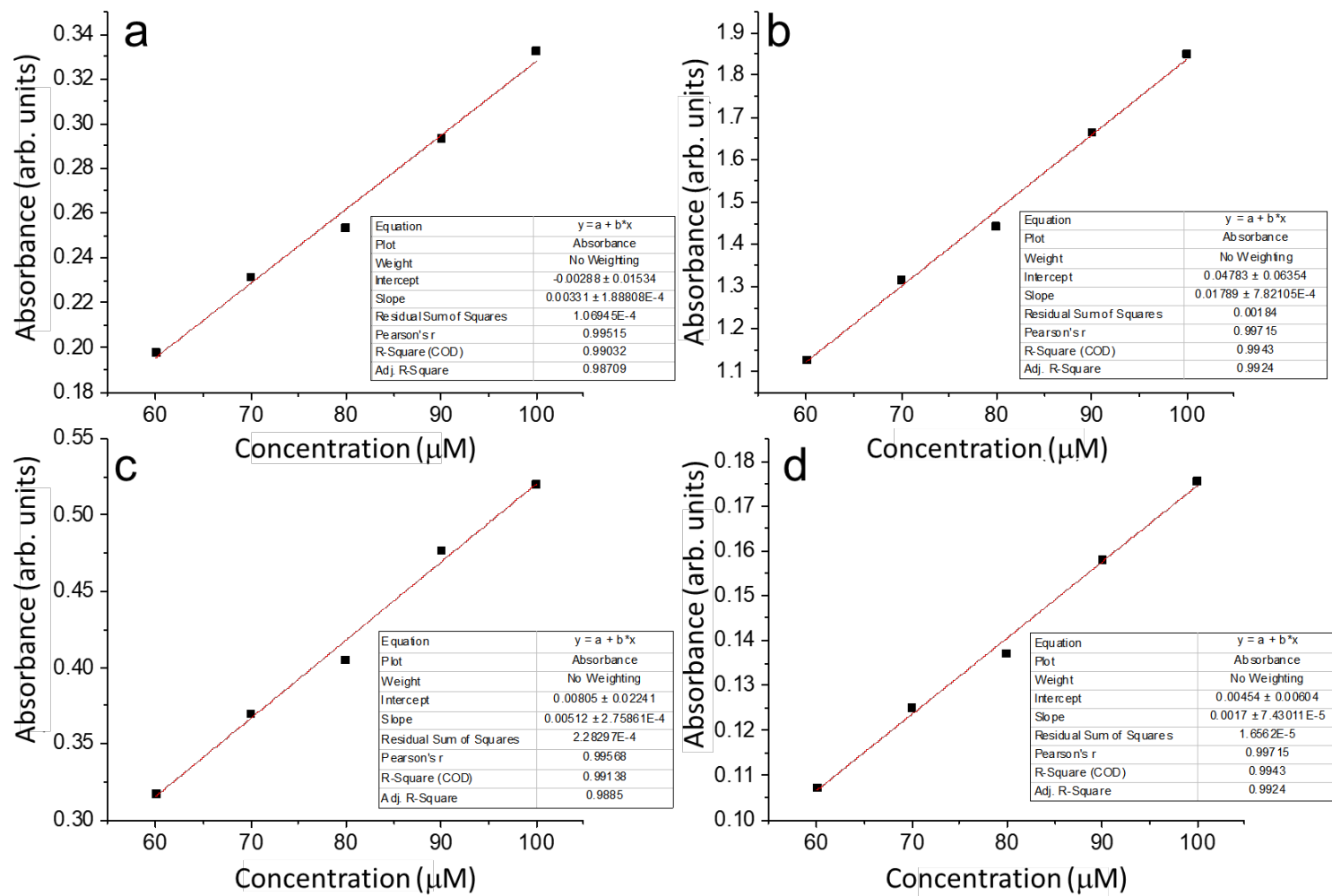


**Figure S25.** Plot of Q band  $\lambda_{\max}$  at different concentrations for compound **1e** in  $\text{CH}_2\text{Cl}_2$ . a)  $\lambda_{\max}$  of Q<sub>1</sub>, b)  $\lambda_{\max}$  of Q<sub>2</sub>, c)  $\lambda_{\max}$  of Q<sub>3</sub>, and d)  $\lambda_{\max}$  of Q<sub>4</sub>.

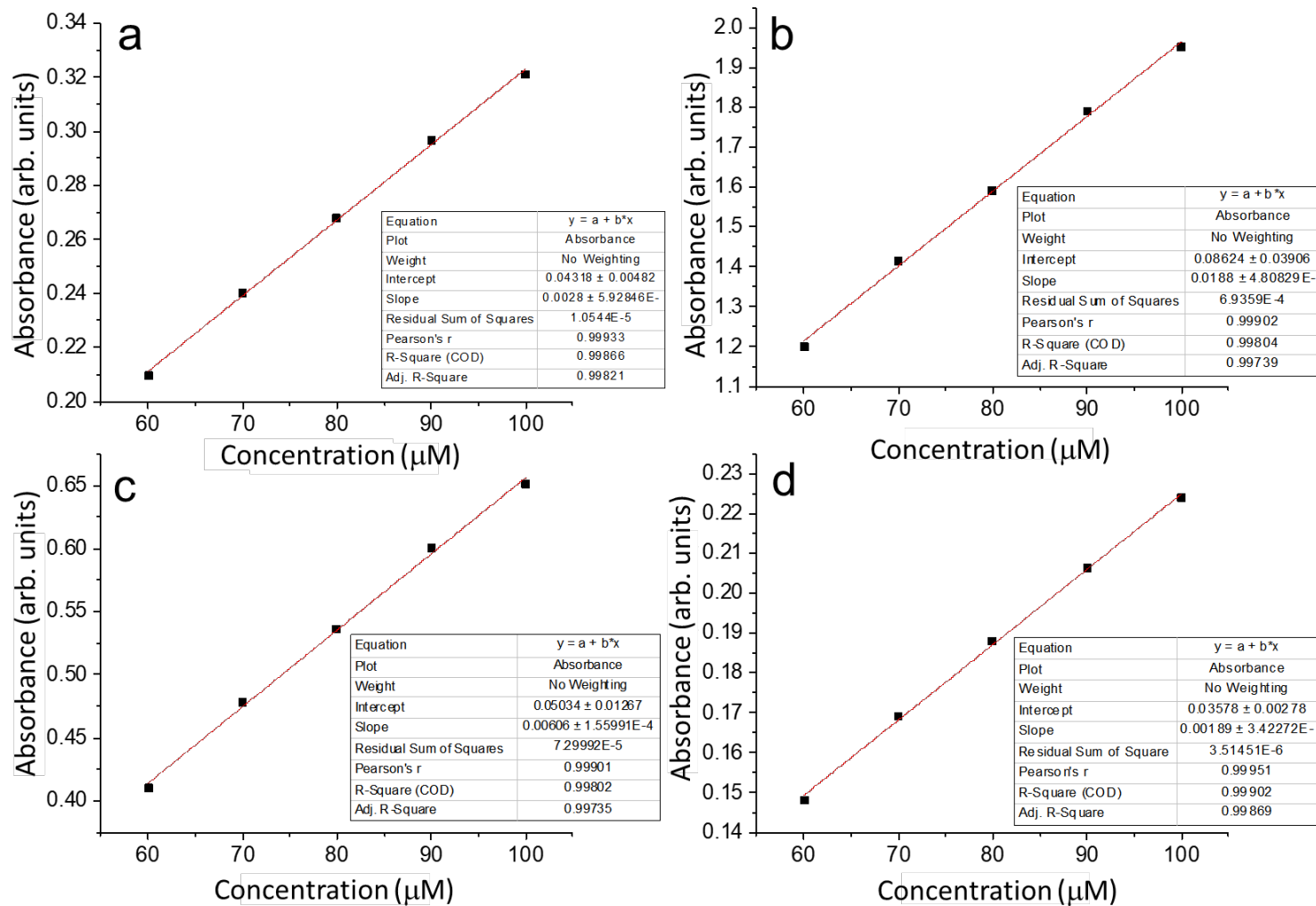


**Figure S26.** Plot of Q band  $\lambda_{\max}$  at different concentrations for compound **1f** in  $\text{CH}_2\text{Cl}_2$ . a)  $\lambda_{\max}$  of  $\text{Q}_1$ , b)  $\lambda_{\max}$  of  $\text{Q}_2$ , c)  $\lambda_{\max}$  of  $\text{Q}_3$ , and d)  $\lambda_{\max}$  of  $\text{Q}_4$ .

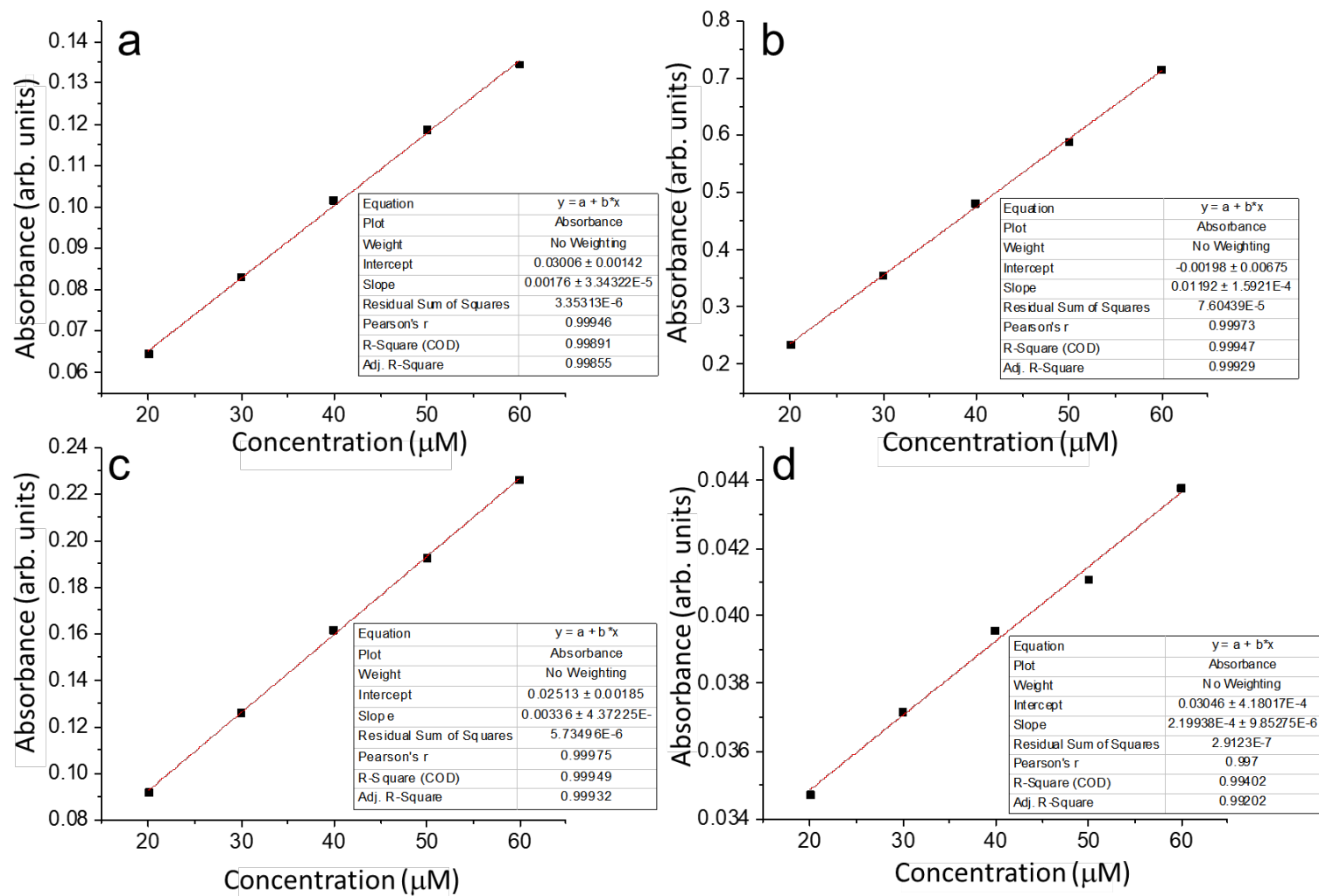


**Figure S27.** Plot of Q band  $\lambda_{\max}$  at different concentrations for compound **1g** in  $\text{CH}_2\text{Cl}_2$ . a)  $\lambda_{\max}$  of Q<sub>1</sub>, b)  $\lambda_{\max}$  of Q<sub>2</sub>, c)  $\lambda_{\max}$  of Q<sub>3</sub>, and d)  $\lambda_{\max}$  of Q<sub>4</sub>.

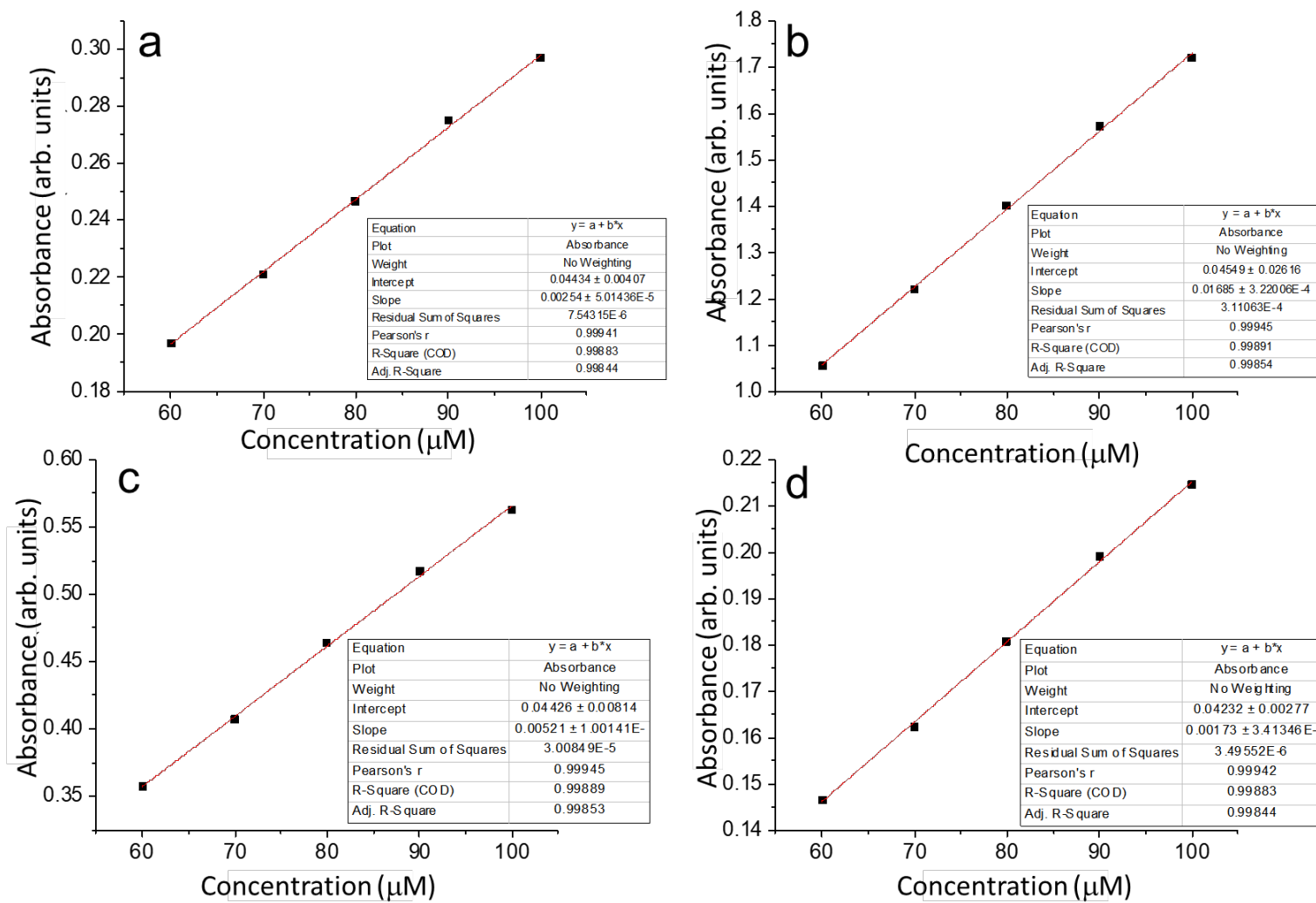


**Figure S28.** Plot of Q band  $\lambda_{\max}$  at different concentrations for compound **1h** in  $\text{CH}_2\text{Cl}_2$ . a)  $\lambda_{\max}$  of  $Q_1$ , b)  $\lambda_{\max}$  of  $Q_2$ , c)  $\lambda_{\max}$  of  $Q_3$ , and d)  $\lambda_{\max}$  of  $Q_4$ .

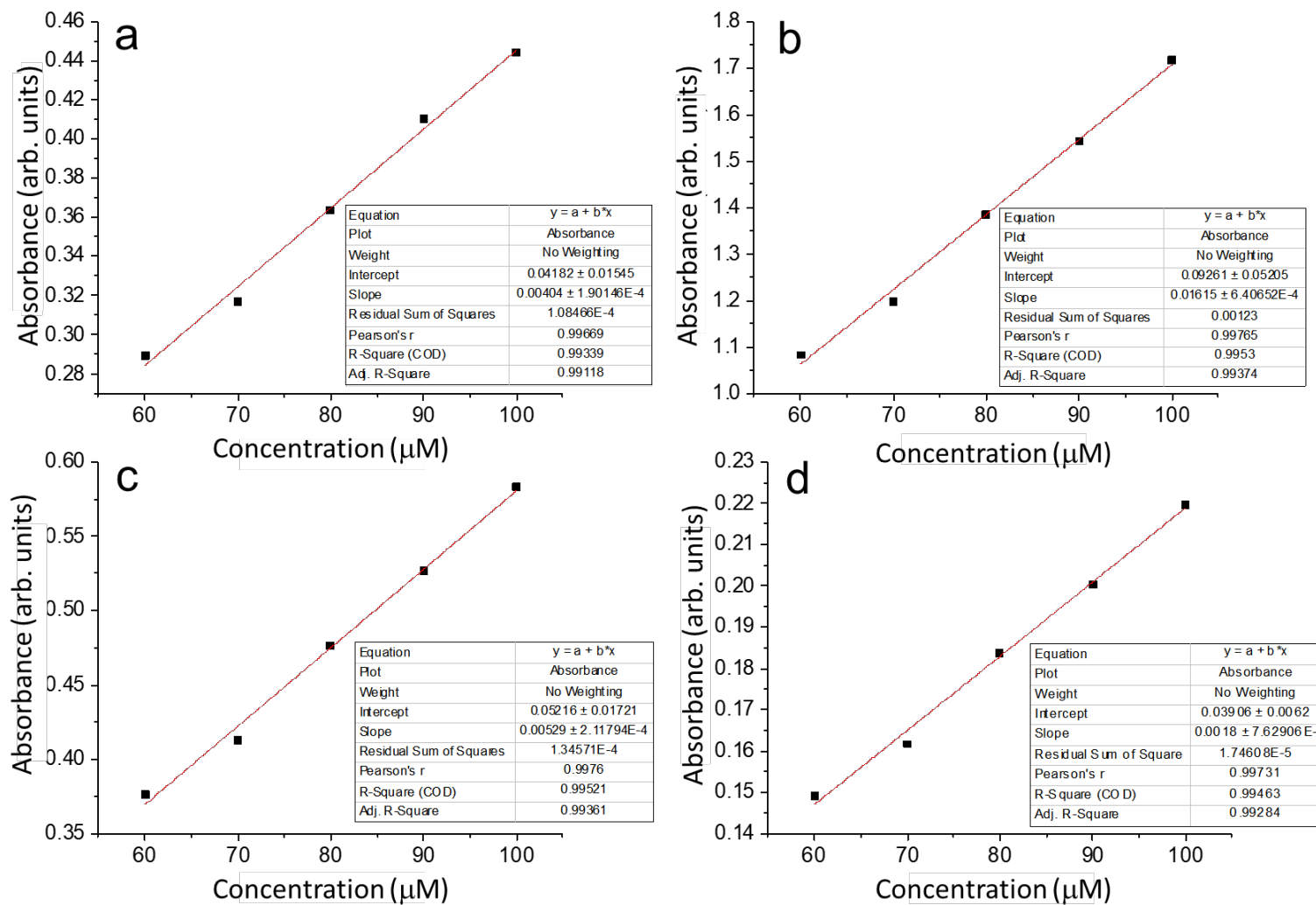


**Figure S29.** Plot of Q band  $\lambda_{\max}$  at different concentrations for compound **1i** in  $\text{CH}_2\text{Cl}_2$ . a)  $\lambda_{\max}$  of  $Q_1$ , b)  $\lambda_{\max}$  of  $Q_2$ , c)  $\lambda_{\max}$  of  $Q_3$ , and d)  $\lambda_{\max}$  of  $Q_4$ .

## 5. Photoluminescence Spectroscopy

Samples for room temperature fluorescence spectroscopy (Figure S30) were prepared as 10  $\mu\text{M}$   $\text{CH}_2\text{Cl}_2$  solutions. The solid-state photoluminescence of PorSils **1a**, **1b**, **1i** and **TPP-H<sub>2</sub>** were also measured at room temperature by preparing dispersions (1 wt% films) in an optically clear ZEONEX<sup>®</sup> Cyclo Olefin Polymer (COP) matrix or optically clear PMMA. Films were prepared by drop casting solutions of the polymer and SOPS. The results are shown in Figures S31-32. Sample **1i** for VT fluorescence was measured as a 1  $\mu\text{M}$  2-MeTHF solution and as an optically clear ZEONEX Cyclo Olefin Polymer (COP) matrix. 2-Methyltetrahydrofuran (2-MeTHF) was used as the solvent system, because it forms a stable organic glass which is UV-Vis transparent at low temperatures. Both solution- and solid-state samples were kept at each temperature for at least 10 min to equilibrate prior to recording the spectra. The results of VT fluorescence are summarized in Figure S33.

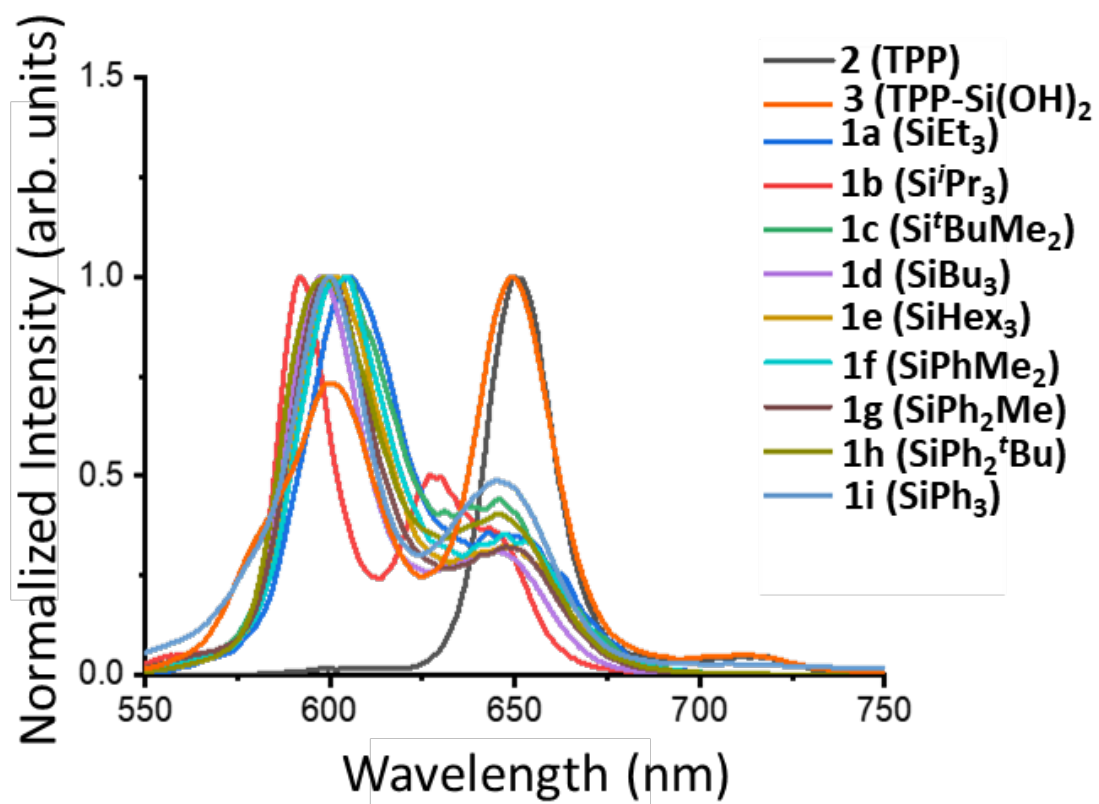


**Figure S30.** Normalized emission profiles acquired for solutions of SOPS (**1a-1i**), parent **2**, and **3** in CH<sub>2</sub>Cl<sub>2</sub>.



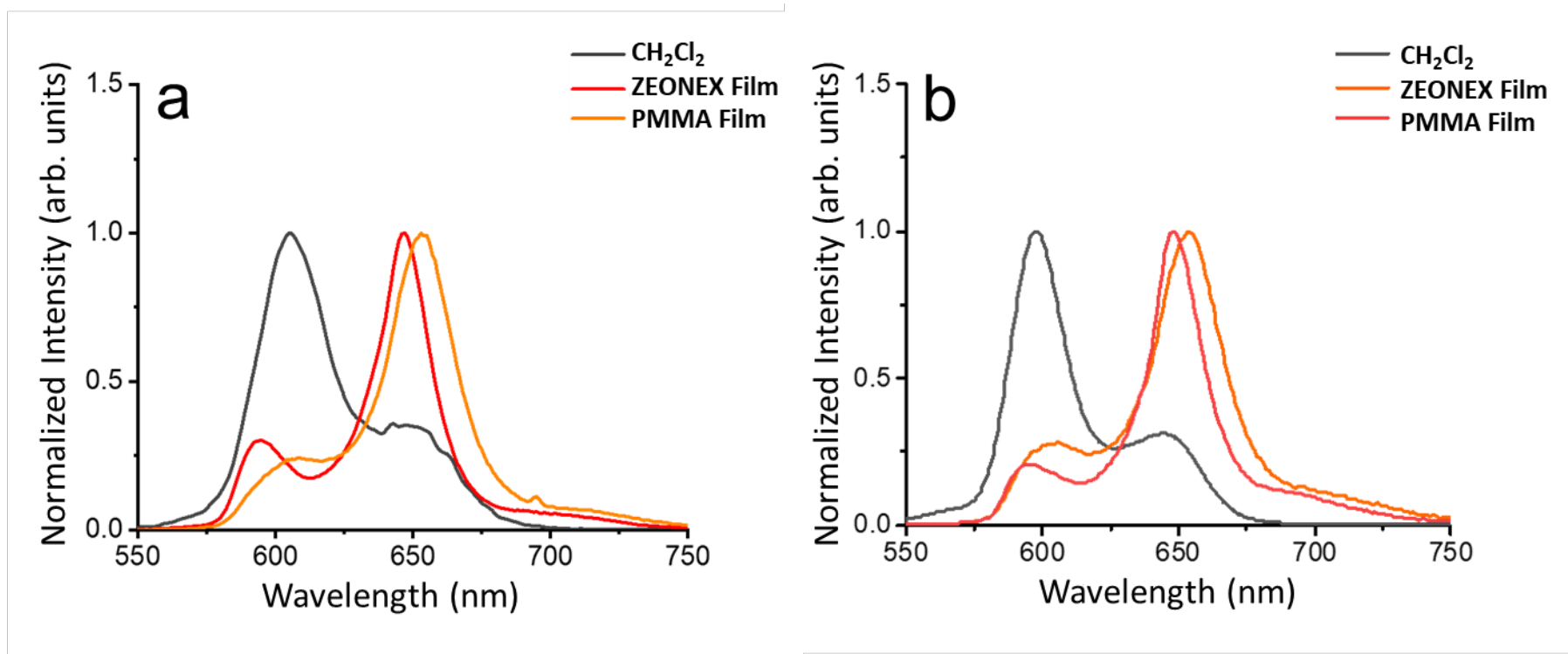


**Figure S31.** Normalized emission profiles of a) **1a** (SiEt<sub>3</sub>) and b) **1d** (Si<sup>i</sup>Pr<sub>3</sub>) dispersed in optically clear amorphous polymer films (1 wt%) are contrasted with the emission in CH<sub>2</sub>Cl<sub>2</sub> (10 μM).

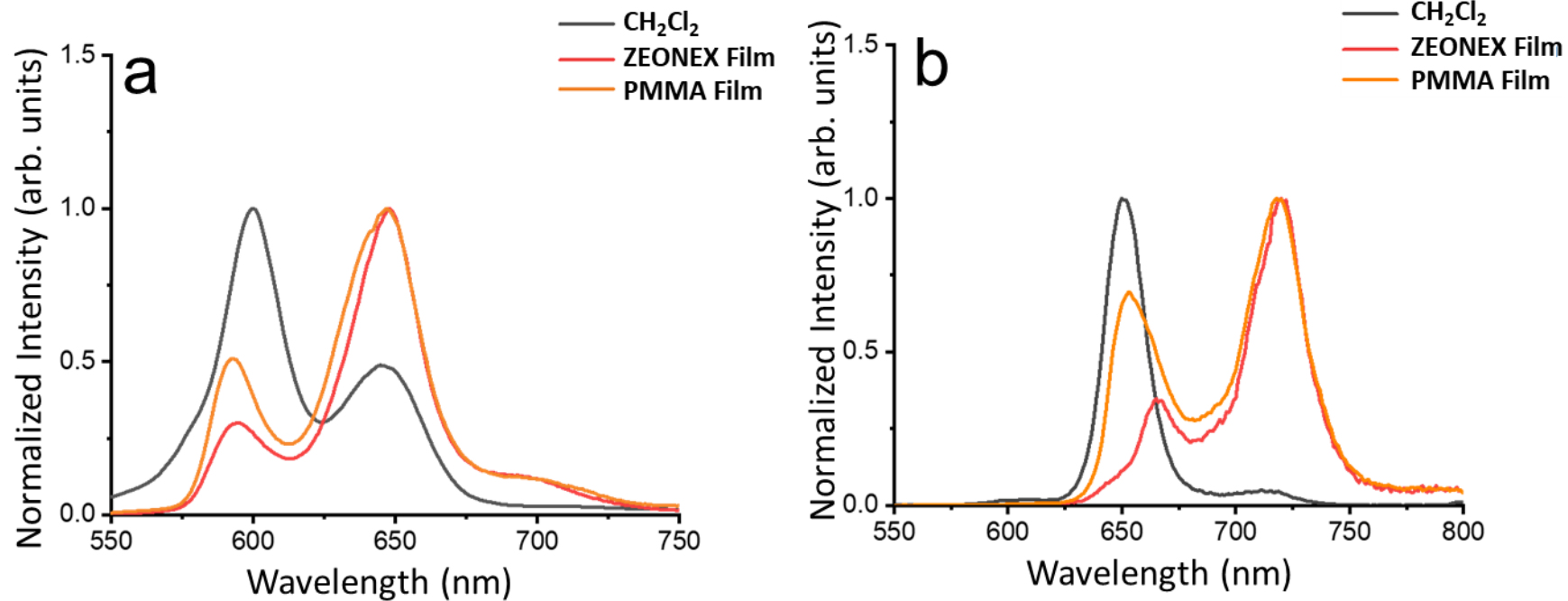


**Figure S32.** Normalized emission profiles of a) **1i** (SiPh<sub>3</sub>) and b) **2** (TPP-H<sub>2</sub>) dispersed in optically clear amorphous polymer films (1 wt%) are contrasted with the emission in CH<sub>2</sub>Cl<sub>2</sub> (10 μM).

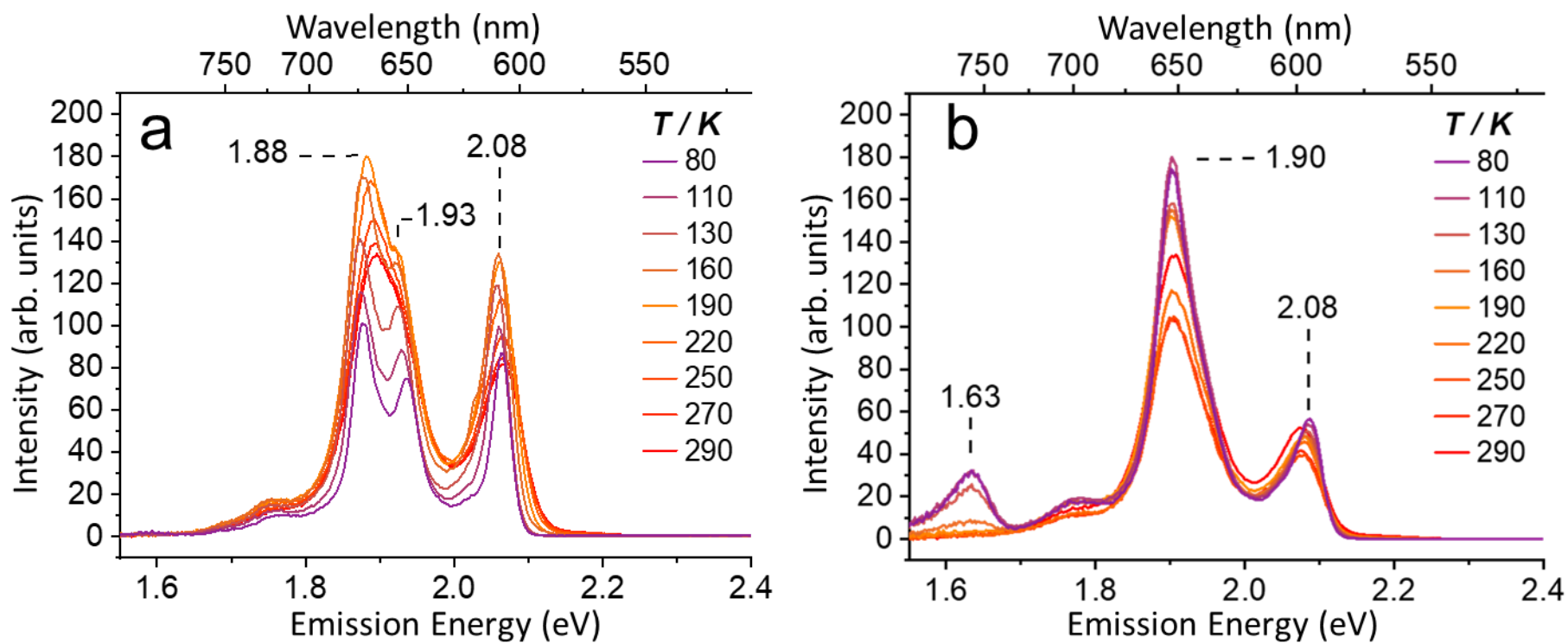


**Figure S33.** VT fluorescence spectra of 2-MeTHF solutions ( $l = 10$  mm,  $T = 80$ – $290$  K) of **1i**  $\lambda_{\text{ex}} = 425$  nm,  $c = 1$   $\mu\text{M}$ ; Inset in panel (a): Legend for temperatures in all panels

## 6. Cyclic Voltammetry

The cyclic voltammetry (CV) measurements were carried out with Gamry Interface 1000 potentiostat/galvanostat controlled by an external computer and utilizing a three-electrode configuration at 25 °C. The working electrode was a Pt disc with a surface area of 0.071 cm<sup>2</sup>. A Pt wire served as the counter electrode. Saturated calomel electrode (SCE) was employed as the reference electrode and separated from the bulk of the solution by a double bridge. Electrochemical grade NBu<sub>4</sub>PF<sub>6</sub> in anhydrous degassed CH<sub>2</sub>Cl<sub>2</sub> was employed as the supporting electrolyte at a concentration of 0.1 M.

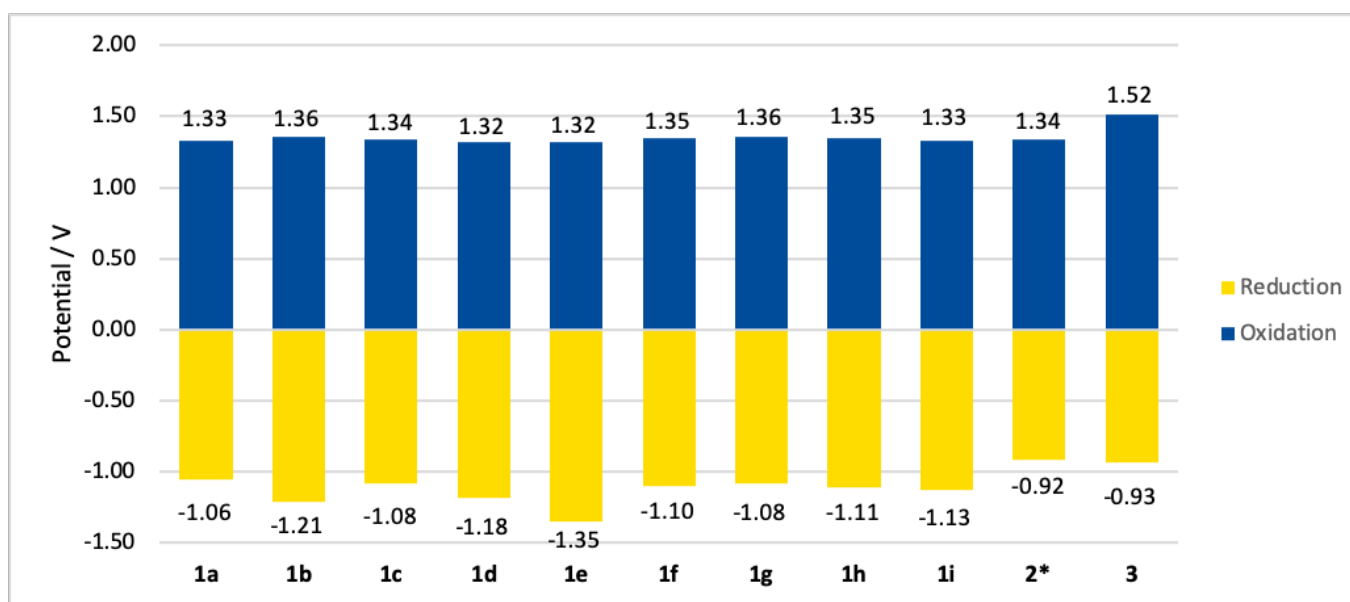


**Figure S34.** Redox potentials of SOPS (**1a–1i**), **2** (TPP-H<sub>2</sub>) and **3**. Data were collected using a 0.1 M solution of NBu<sub>4</sub>PF<sub>6</sub> in CH<sub>2</sub>Cl<sub>2</sub> at 100 mV s<sup>-1</sup> to [Fc]/[Fc<sup>+</sup>] internal standard followed by conversion to NHE; [Fc]/[Fc<sup>+</sup>] = +765 mV vs. NHE in CH<sub>2</sub>Cl<sub>2</sub>. \***2** has a second oxidation peak at 1.65 V.

**Observed**

<i>Compound</i>	<i>Ox. max</i>	<i>Ox. min</i>	<i>Red. min</i>	<i>Red. max</i>	<i>Fc max</i>	<i>Fc min</i>	<i>E½ Ox</i>	<i>E½ Red</i>	<i>(Fc/Fc+) E½</i>
<b>1a</b>	1.033	0.943	-1.512	-1.396	0.488	0.363	0.988	-1.396	0.426
<b>1b</b>	1.197	1.093	-1.480	-1.362	0.632	0.477	1.145	-1.421	0.555
<b>1c</b>	1.211	1.113	-1.269	-1.245	0.655	0.526	1.162	-1.257	0.591
<b>1d</b>	1.180	1.085	-1.431	-1.305	0.629	0.529	1.133	-1.368	0.579
<b>1e</b>	1.184	1.094	-1.530	-1.391	0.677	0.494	1.139	-1.530	0.586
<b>1f</b>	1.208	1.109	-1.347	-1.243	0.632	0.516	1.159	-1.295	0.574
<b>1g</b>	1.185	1.100	-1.346	-1.241	0.595	0.502	1.143	-1.294	0.549
<b>1h</b>	1.121	1.031	-1.448	-1.315	0.541	0.449	1.076	-1.382	0.495
<b>1i</b>	1.210	1.114	-1.347	-1.241	0.661	0.539	1.162	-1.294	0.600
<b>2</b>	0.910	0.887	-1.365	-1.341	0.425	0.229	0.899	-1.353	0.327
	1.238	1.146							
<b>3</b>	1.331	1.224	-1.244	-1.103	0.597	0.453	1.278	-1.174	0.525

**Calibrated to ferrocene (Fc) at 0.765V NHE in DCM**

<i>Compound</i>	$\Delta Fc$	<i>E½ Ox</i>	<i>E½ Red</i>	<i>E½ Ox 2</i>
<b>1a</b>	0.340	1.328	-1.057	
<b>1b</b>	0.211	1.356	-1.211	
<b>1c</b>	0.175	1.337	-1.083	
<b>1d</b>	0.186	1.319	-1.182	
<b>1e</b>	0.180	1.319	-1.351	
<b>1f</b>	0.191	1.350	-1.104	
<b>1g</b>	0.217	1.359	-1.077	
<b>1h</b>	0.270	1.346	-1.112	
<b>1i</b>	0.165	1.327	-1.129	
<b>2</b>	0.438	1.337	-0.915	1.63
<b>3</b>	0.240	1.518	-0.934	

**Table S1.** Raw CV data seen in Figures S35-40, and values derived by calibration to oxidation of ferrocene.

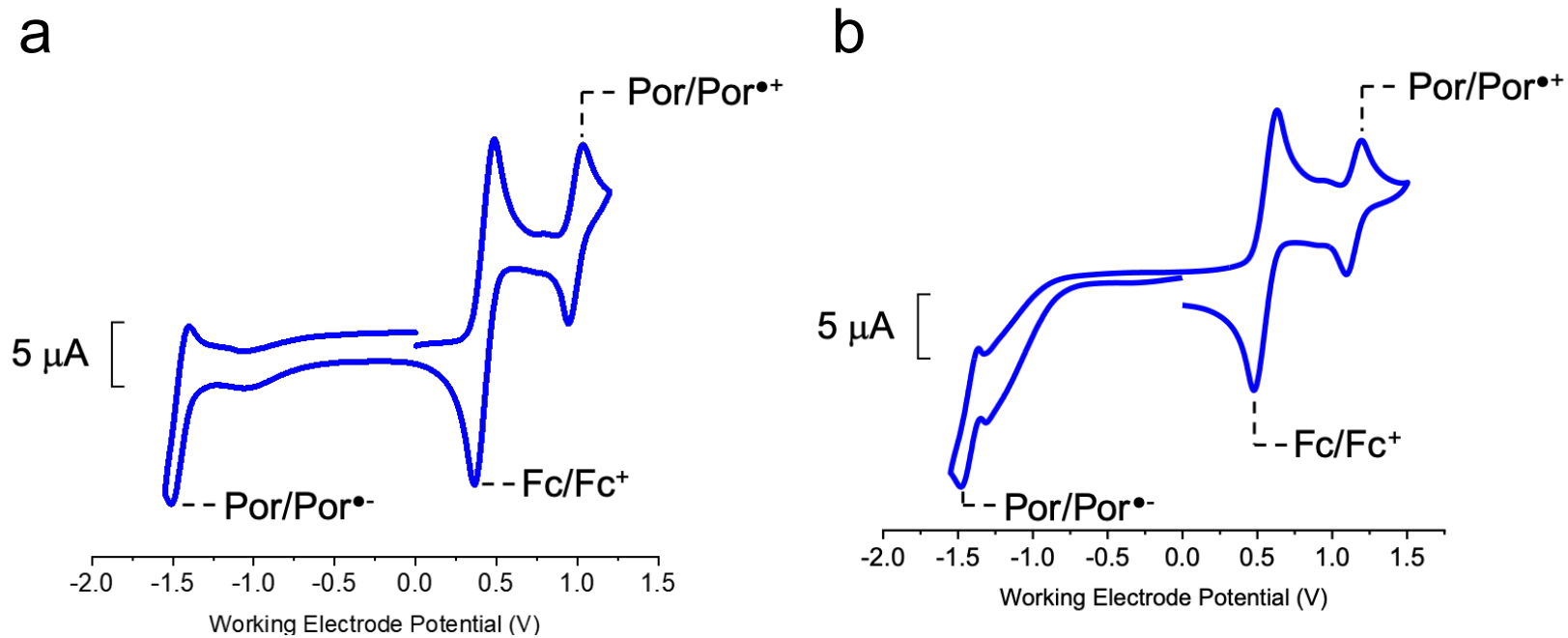


**Figure S35.** CV of a) **1a** and b) **1b**. Data were collected using 0.1 MNBu<sub>4</sub>PF<sub>6</sub> CH<sub>2</sub>Cl<sub>2</sub> solutions at 100 mV s<sup>-1</sup> to [Fc]/[Fc<sup>+</sup>] internal standard followed by conversion to NHE; [Fc]/[Fc<sup>+</sup>] = +765 mV vs. NHE in CH<sub>2</sub>Cl<sub>2</sub>. \*Reference oxidation peaks (ferrocene).

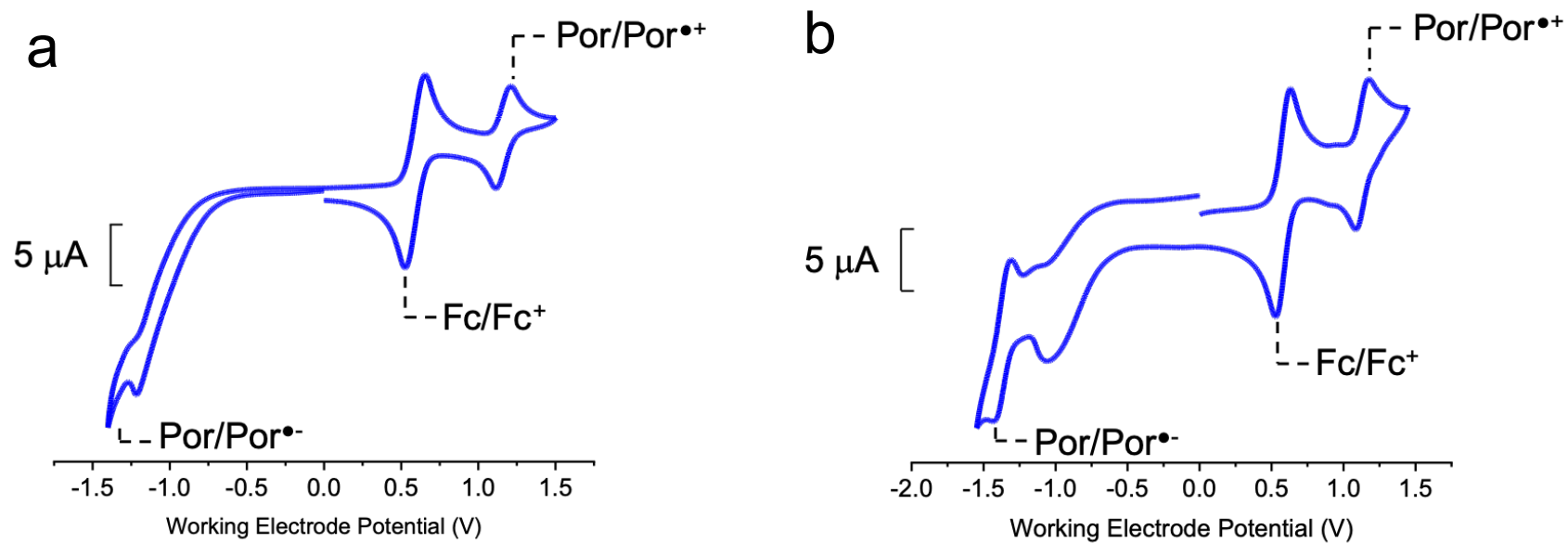


**Figure S36.** CV of a) **1c**, and b) **1d**. Data were collected using 0.1 MNBu<sub>4</sub>PF<sub>6</sub> CH<sub>2</sub>Cl<sub>2</sub> solutions at 100 mV s<sup>-1</sup> to [Fc]/[Fc<sup>+</sup>] internal standard followed by conversion to NHE; [Fc]/[Fc<sup>+</sup>] = +765 mV vs. NHE in CH<sub>2</sub>Cl<sub>2</sub>. \*Reference oxidation peaks (ferrocene).

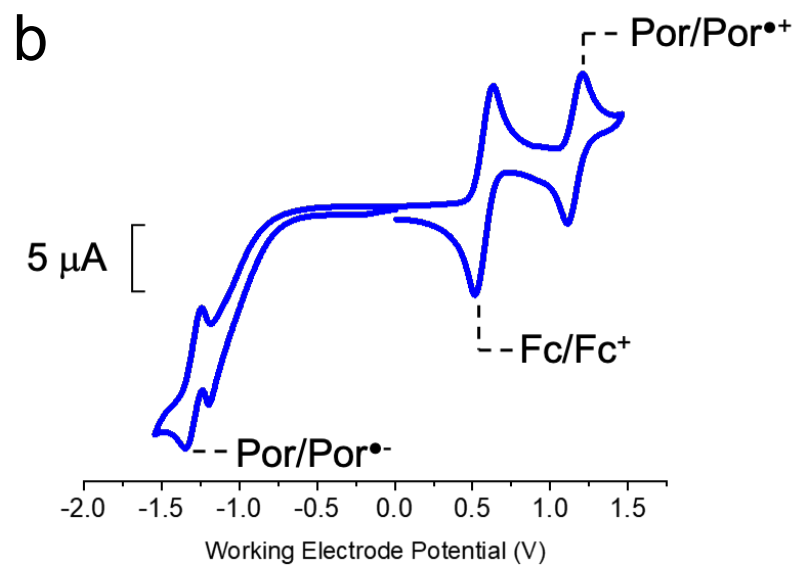
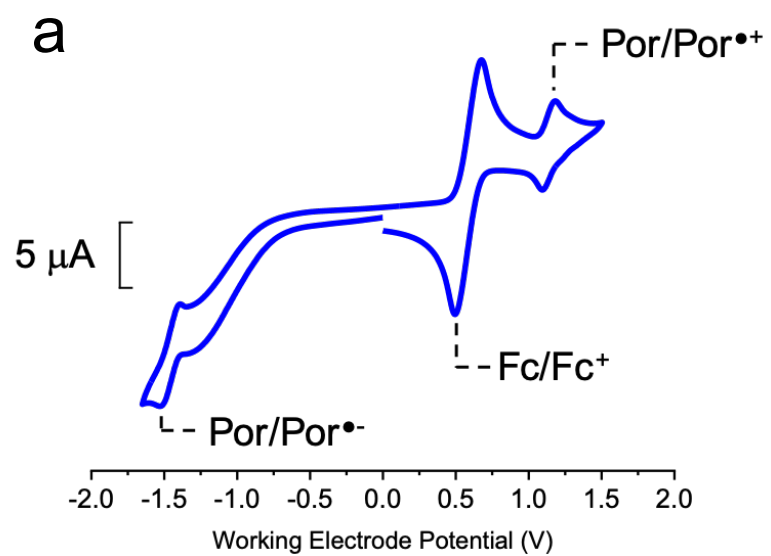


**Figure S37.** CV of a) **1e**, and b) **1f**. Data were collected using 0.1 MNBu<sub>4</sub>PF<sub>6</sub> CH<sub>2</sub>Cl<sub>2</sub> solutions at 100 mV s<sup>-1</sup> to [Fc]/[Fc<sup>+</sup>] internal standard followed by conversion to NHE; [Fc]/[Fc<sup>+</sup>] = +765 mV vs. NHE in CH<sub>2</sub>Cl<sub>2</sub>. \*Reference oxidation peaks (ferrocene).



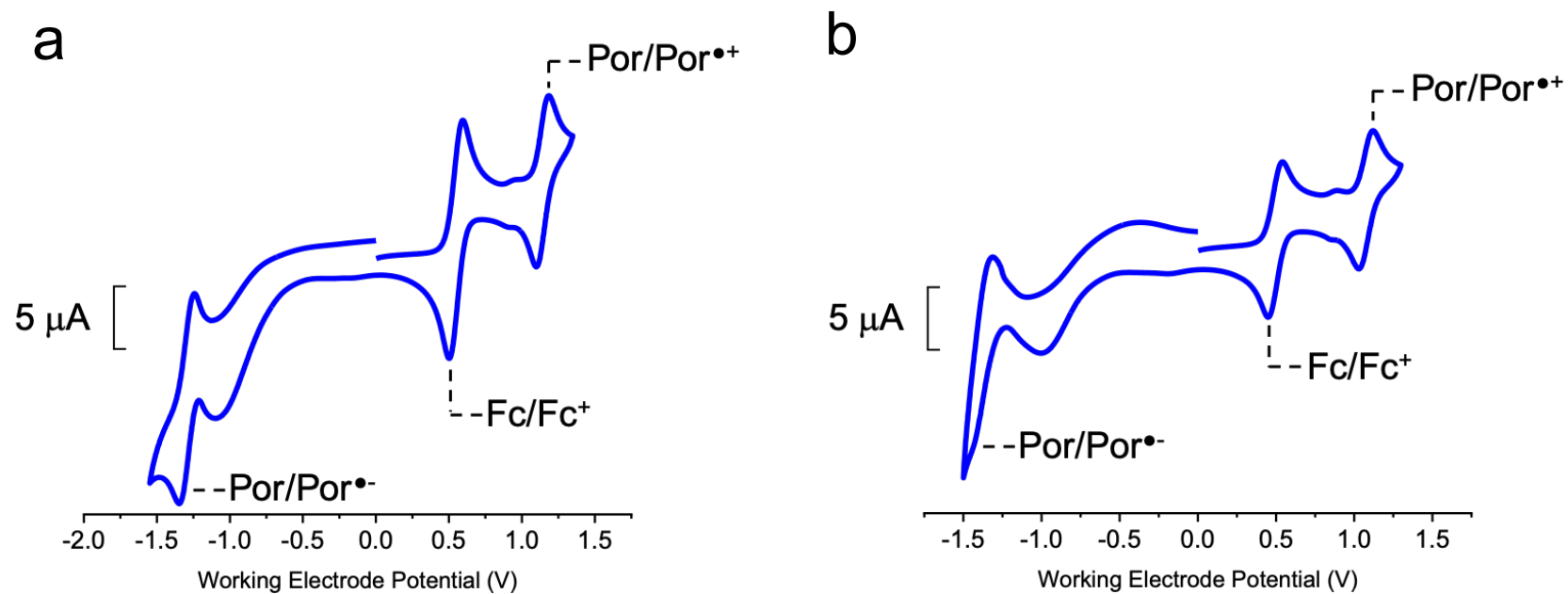


**Figure S38.** CV of a) **1g**, and b) **1h**. Data were collected using 0.1  $\text{MNBu}_4\text{PF}_6$   $\text{CH}_2\text{Cl}_2$  solutions at  $100 \text{ mV s}^{-1}$  to  $[\text{Fc}]/[\text{Fc}^+]$  internal standard followed by conversion to NHE;  $[\text{Fc}]/[\text{Fc}^+] = +765 \text{ mV vs. NHE}$  in  $\text{CH}_2\text{Cl}_2$ . \*Reference oxidation peaks (ferrocene).

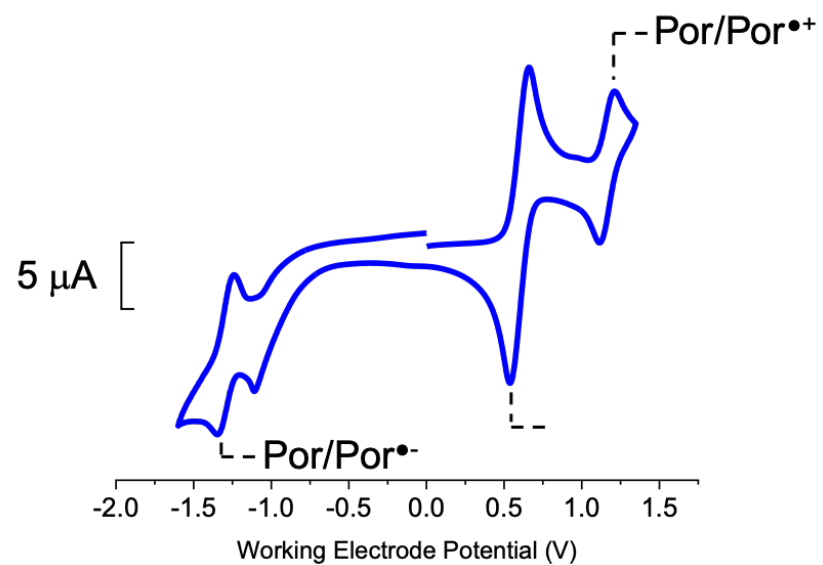


**Figure S39.** CV of **1i**. Data were collected using 0.1 MNBu<sub>4</sub>PF<sub>6</sub> CH<sub>2</sub>Cl<sub>2</sub> solutions at 100 mV s<sup>-1</sup> to [Fc]/[Fc<sup>+</sup>] internal standard followed by conversion to NHE; [Fc]/[Fc<sup>+</sup>] = +765 mV vs. NHE in CH<sub>2</sub>Cl<sub>2</sub>. \*Reference oxidation peaks (ferrocene).

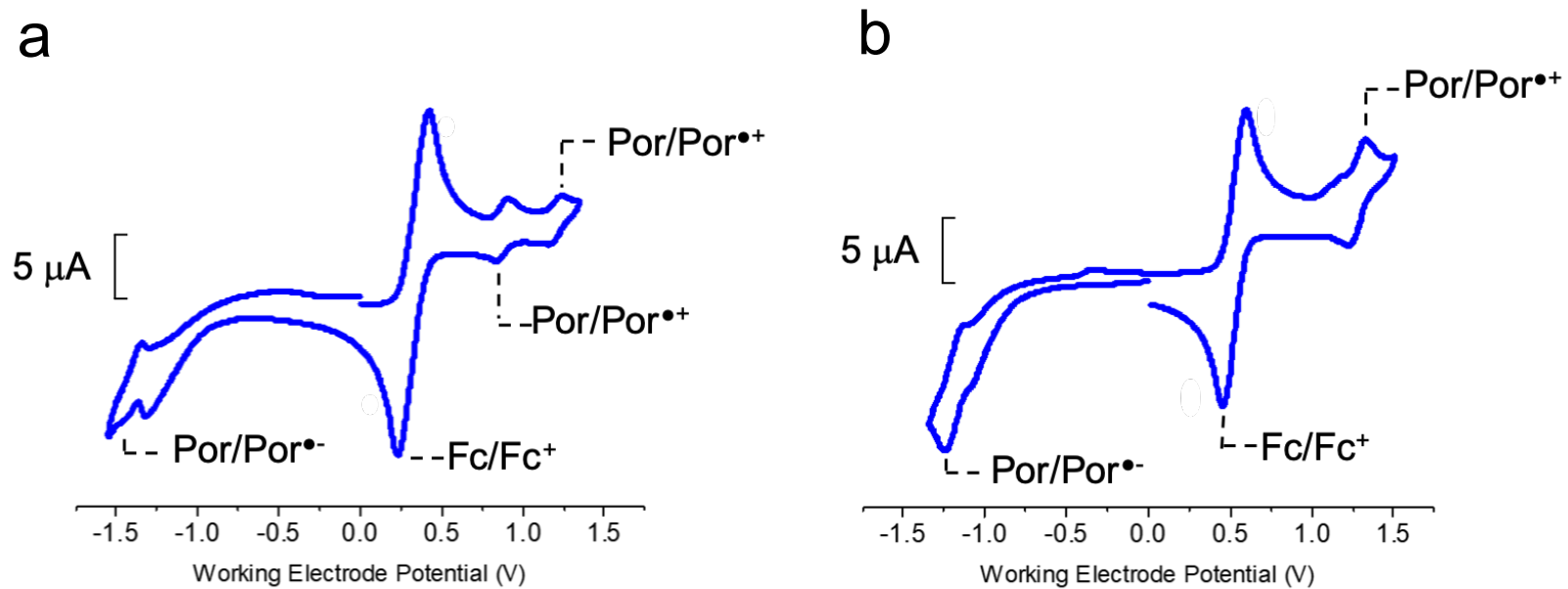


**Figure S40.** CV of a) **2**, and b) **3**. Data were collected using 0.1 MNBu<sub>4</sub>PF<sub>6</sub> CH<sub>2</sub>Cl<sub>2</sub> solutions at 100 mV s<sup>-1</sup> to [Fc]/[Fc<sup>+</sup>] internal standard followed by conversion to NHE; [Fc]/[Fc<sup>+</sup>] = +765 mV vs. NHE in CH<sub>2</sub>Cl<sub>2</sub>. \*Reference oxidation peaks (ferrocene).

## 7. X-Ray Crystallographic Analysis

Suitable single crystals of all four compounds **1f-i** were mounted on a cryoloop with paratone oil and examined on a Bruker APEX-II CCD diffractometer equipped with a CCD area detector and an Oxford Cryoflex low temperature device. Data were collected at 150(2) K with Mo K $\alpha$  radiation ( $\lambda = 0.71073 \text{ \AA}$ ) using the APEX-II software.<sup>5</sup> Cell refinement and data-reduction were carried out by SAINT. An absorption correction was performed by multi-scan method implemented in SADABS.<sup>6</sup> The structures of the complexes were solved by (SHELXT)<sup>7</sup> and refined using SHELXL-2014 in the Bruker SHELXTL suite.<sup>8</sup> Hydrogen atoms were added at calculated positions and refined with a riding model. In compound **1g**, disordered solvent was removed using the SQUEEZE procedure in PLATON.<sup>9</sup> Selected crystallographic data for the complexes are presented in Table S2. All four compounds have been deposited in the Cambridge Structural Database with numbers CCDC 1977452-1977455.

**Table S2.** Summary of select crystallographic data for compounds **1f-1i**

<i>Compound</i>	<b>1f</b>	<b>1g</b>	<b>1h</b>	<b>1i</b>
Chemical formula	C <sub>60</sub> H <sub>50</sub> N <sub>4</sub> O <sub>2</sub> Si <sub>3</sub>	C <sub>70</sub> H <sub>54</sub> N <sub>4</sub> O <sub>2</sub> Si <sub>3</sub>	C <sub>76</sub> H <sub>66</sub> N <sub>4</sub> O <sub>2</sub> Si <sub>3</sub>	C <sub>80</sub> H <sub>58</sub> N <sub>4</sub> O <sub>2</sub> Si <sub>3</sub>
$M_r$	943.31	1067.44	1151.59	1191.57
Crystal system, space group	Monoclinic, <i>P2<sub>1</sub>/n</i>	Monoclinic, <i>P2<sub>1</sub>/n</i>	Tetragonal, <i>I4<sub>1</sub>/a</i>	Triclinic, <i>P</i> <sup>-</sup> <i>1</i>
Temperature (K)	150	150	150	150
<i>a</i> , <i>b</i> , <i>c</i> (Å)	12.8165 (9), 22.7137 (14), 17.6229 (11)	11.6001 (6), 12.5673 (6), 21.2309 (11)	31.4939 (8), 12.3443 (3)	12.8070 (8), 14.8522 (9), 18.6822 (11)
<i>V</i> (Å <sup>3</sup> )	5010.2 (6)	3066.6 (3)	12243.9 (7)	3122.9 (3)
<i>Z</i>	4	2	8	2
Radiation type	Mo <i>K</i> α	Mo <i>K</i> α	Mo <i>K</i> α	Mo <i>K</i> α
μ (mm <sup>-1</sup> )	0.14	0.13	0.13	0.13
Crystal size (mm)	0.15 × 0.1 × 0.05	0.23 × 0.10 × 0.04	0.39 × 0.27 × 0.27	0.12 × 0.06 × 0.03
Absorption correction	Multi-scan Bruker <i>SADABS</i>	Multi-scan Bruker <i>SADABS</i>	Multi-scan Bruker <i>SADABS</i>	Multi-scan Bruker <i>SADABS</i>
<i>T</i> <sub>min</sub> , <i>T</i> <sub>max</sub>	0.640, 0.736	0.536, 0.786	0.945, 0.960	0.672, 0.739
No. of measured, independent, and observed [ <i>I</i> > 2σ( <i>I</i> )] reflections	61068, 10069, 7509	38881, 5387, 4883	96129, 5701, 4924	83666, 10990, 9054
<i>R</i> <sub>int</sub>	0.083	0.043	0.049	0.085
(sin θ/λ) <sub>max</sub> (Å <sup>-1</sup> )	0.630	0.594	0.667	0.595
<i>R</i> [ <i>F</i> <sup>2</sup> > 2σ( <i>F</i> <sup>2</sup> )], <i>wR</i> ( <i>F</i> <sup>2</sup> ), <i>S</i>	0.085, 0.165, 1.08	0.048, 0.154, 0.64	0.050, 0.166, 1.09	0.107, 0.184, 1.28
No. of reflections	10069	5387	5701	10990
No. of parameters	626	359	388	781
H-atom treatment	H-atom parameters constrained	H-atom parameters constrained	H-atom parameters constrained	H-atom parameters constrained
Δρ <sub>max</sub> , Δρ <sub>min</sub> (e Å <sup>-3</sup> )	0.33, -0.47	0.36, -0.54	0.26, -0.28	0.58, -0.57

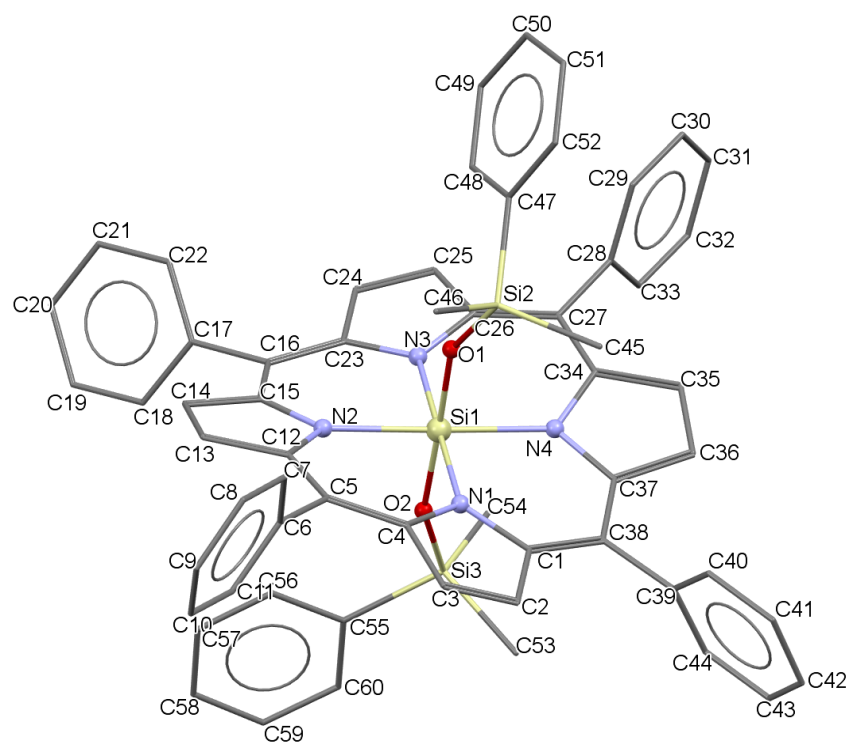


**Figure S41.** Molecular structure of **1f** with appropriate labelling scheme. H-atoms are removed for clarity.

*a* - axis

*b* - axis

*c* - axis

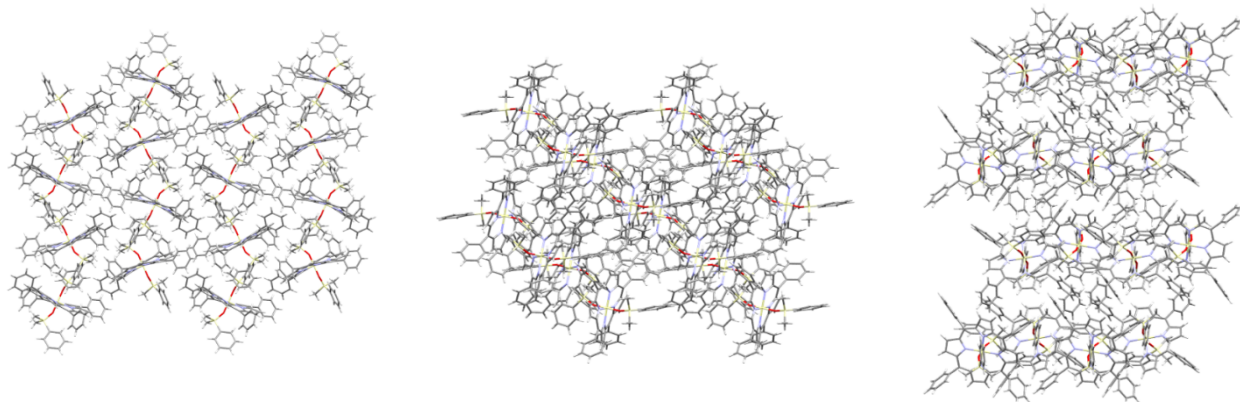


**Figure S42.** Solid-state superstructure of **1f** viewed along the three unit cell axes.

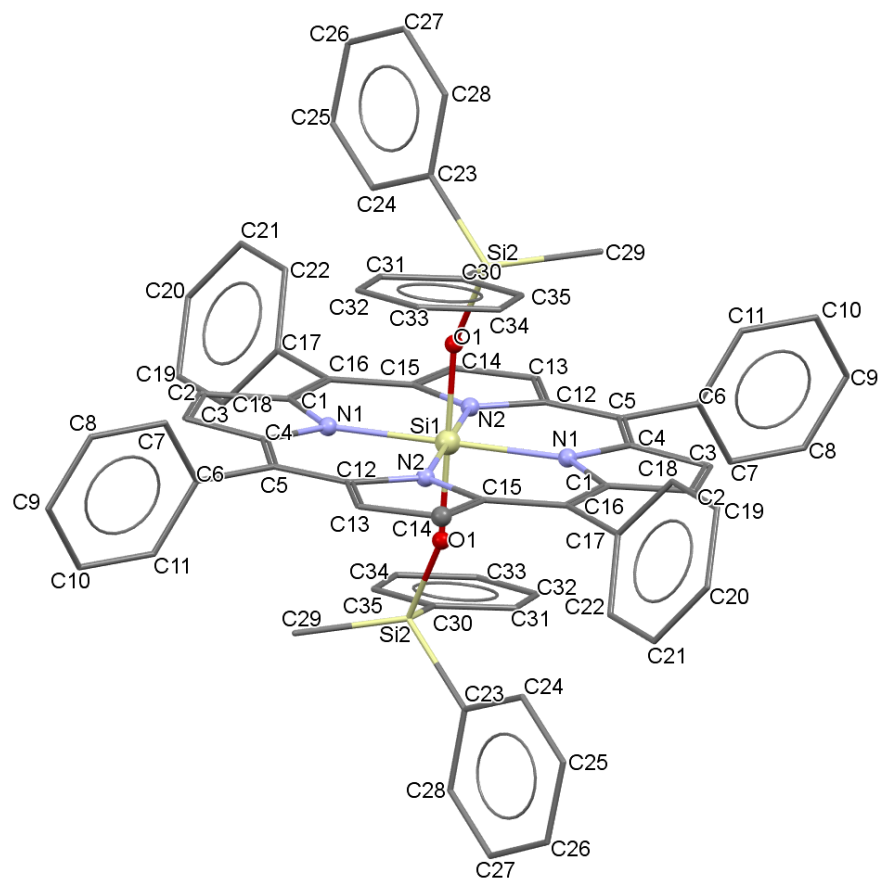


**Figure S43.** Molecular structure of **1g** with appropriate atomic labelling scheme. H-atoms are omitted for clarity.

*a* - axis

*b* - axis

*c* - axis

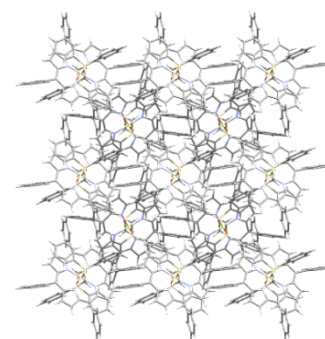
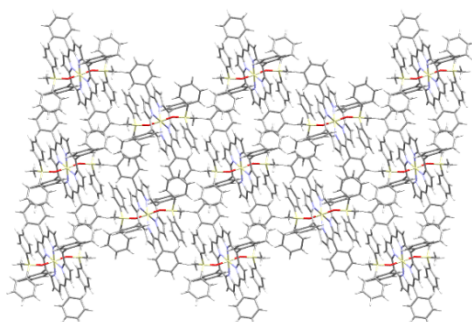
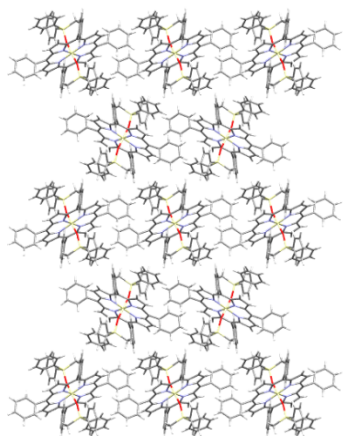


**Figure S44.** Solid-state superstructure of **1g** viewed along the three unit cell axes.

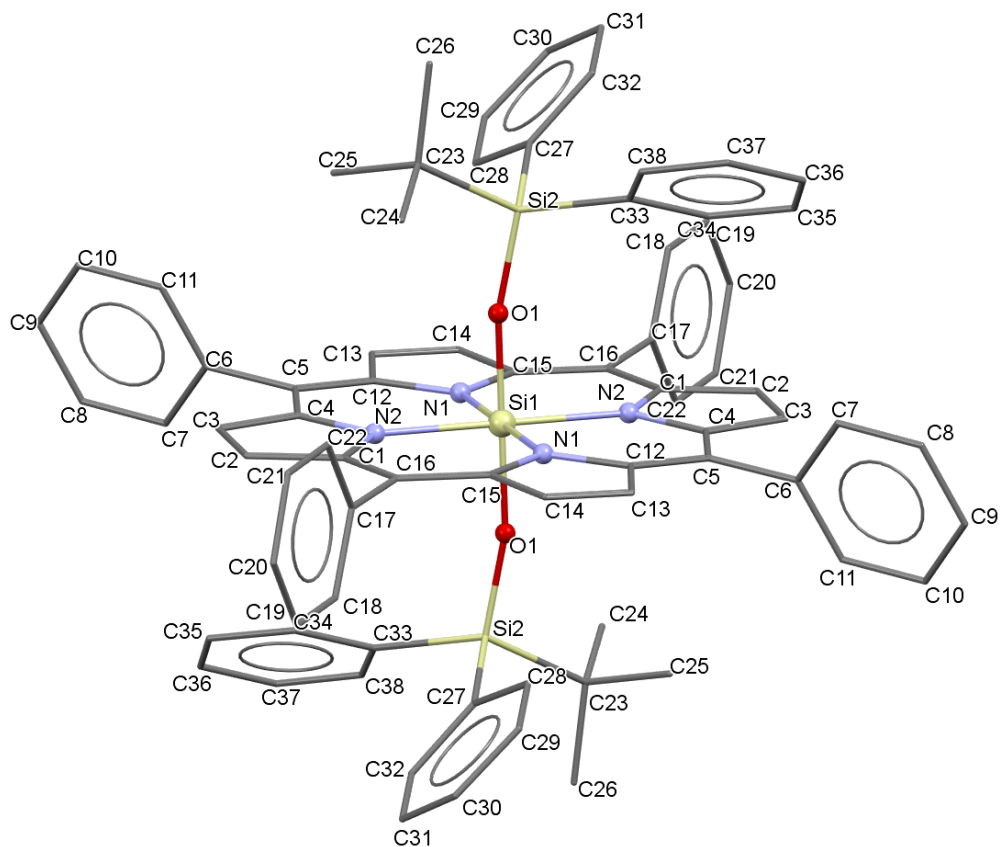


Figure S45. Molecular structure of **1h** with appropriate atomic labelling scheme. H-atoms are omitted for clarity.

*a* - axis

*b* - axis

*c* - axis

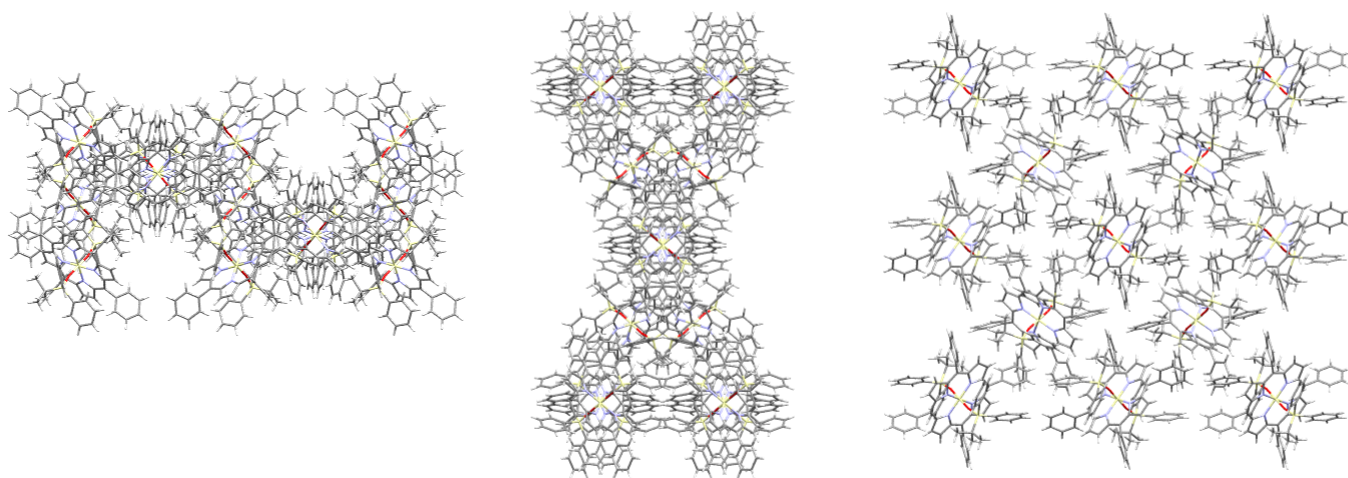
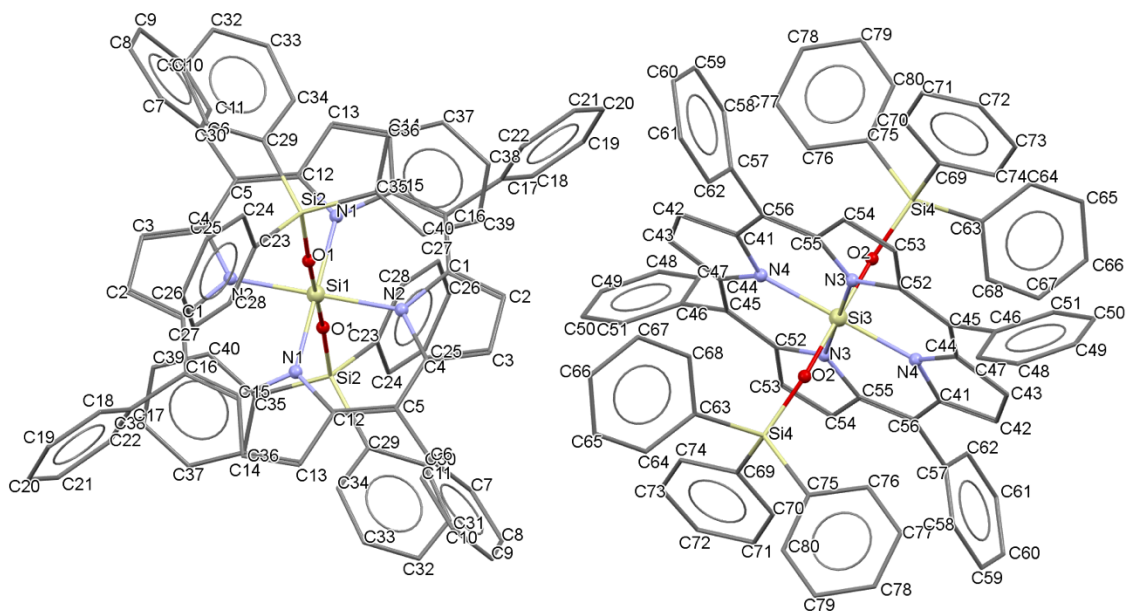


Figure S46. Solid-state superstructure of **1h** viewed along the three unit cell axes.





**Figure S47.** Molecular structure of the two crystallographically independent molecules of **1i** with appropriate atomic labelling schemes. H-atoms are omitted for clarity.

*a* - axis

*b* - axis

*c* - axis

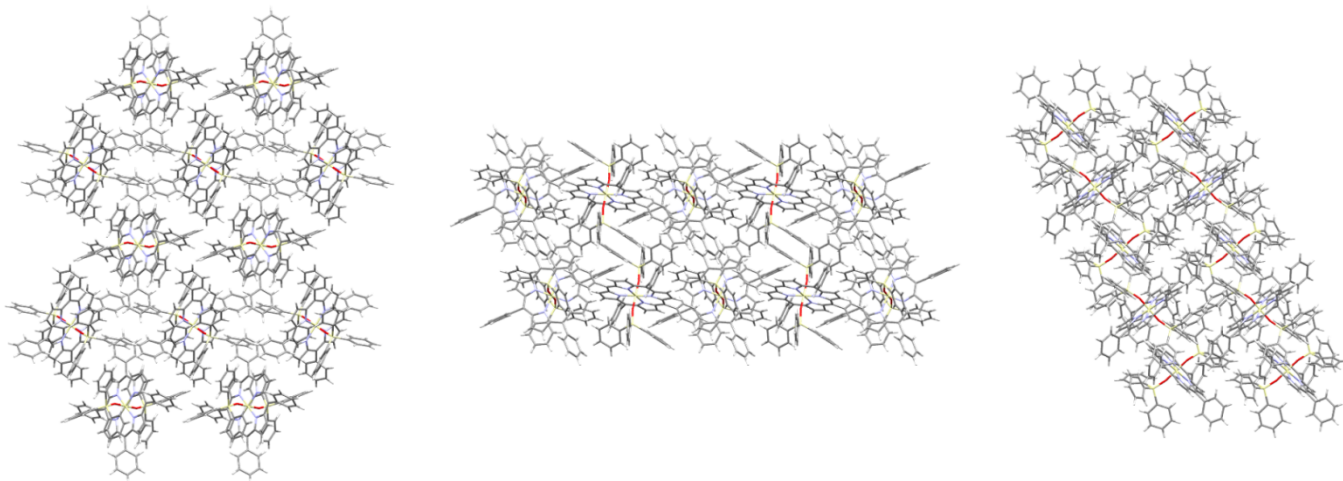


**Figure S48.** Solid-state superstructure of **1i'**/**1i''** viewed along the three unit cell axes.

## 7.1 Intramolecular Contacts in Solid State

The silyloxy caps can interact with the porphyrins by both C-H... $\pi$  and face to face aromatic interactions. Figures S49-53 illustrates the intramolecular contacts in the crystal structures of the aryl silyloxy cap **1f-1i** are within or shorter than the van der Waals radius.

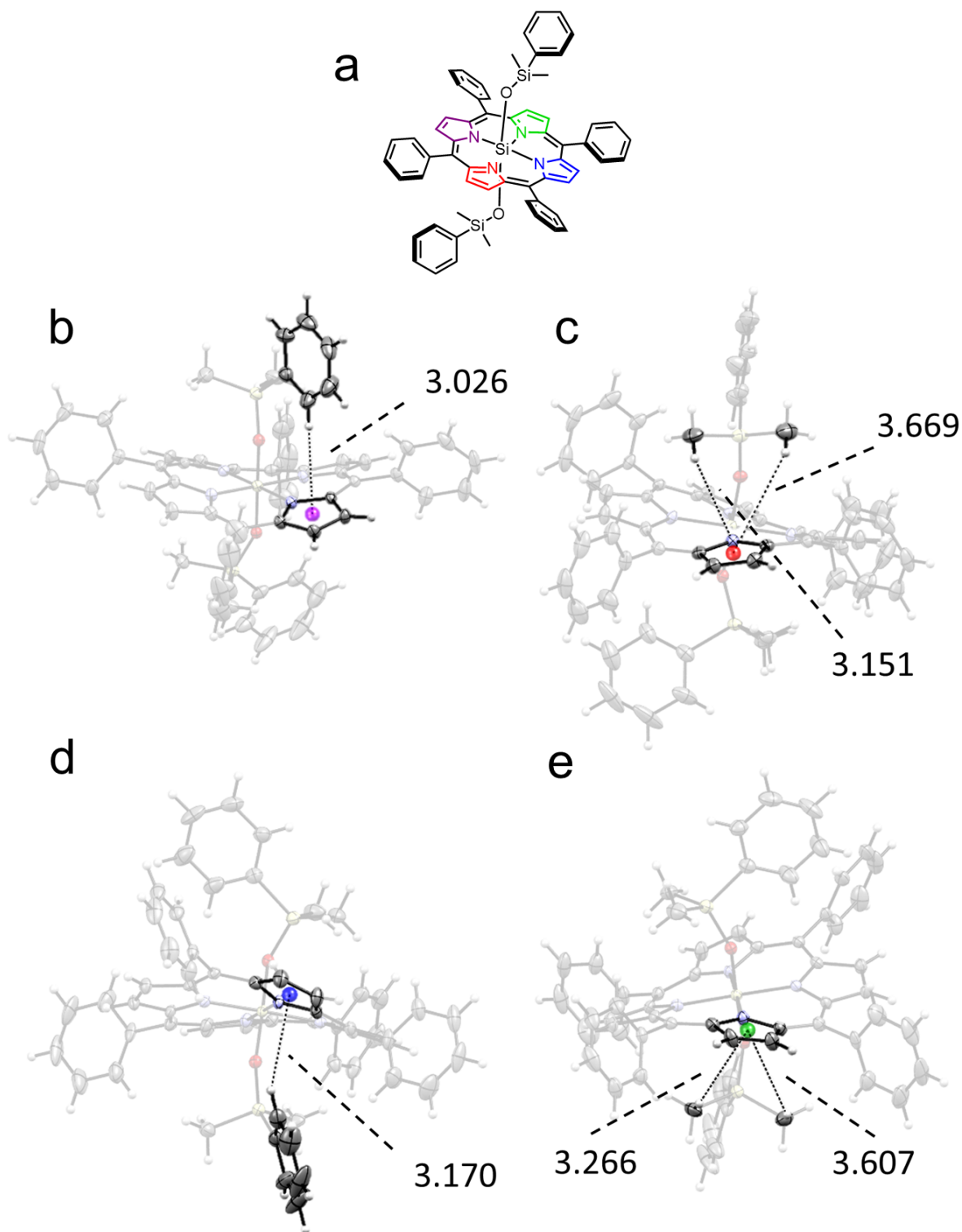


**Figure S49.** a) Structural formula of **1f** where centroids of rings are colored to match crystal structure centroids. b), c), d), and e) Four views of the solid-state structure showing intramolecular interactions of silyloxy cap with the porphyrin ring within/shorter than the sum of the van der Waals radii ( $\leq 3.8$  Å).

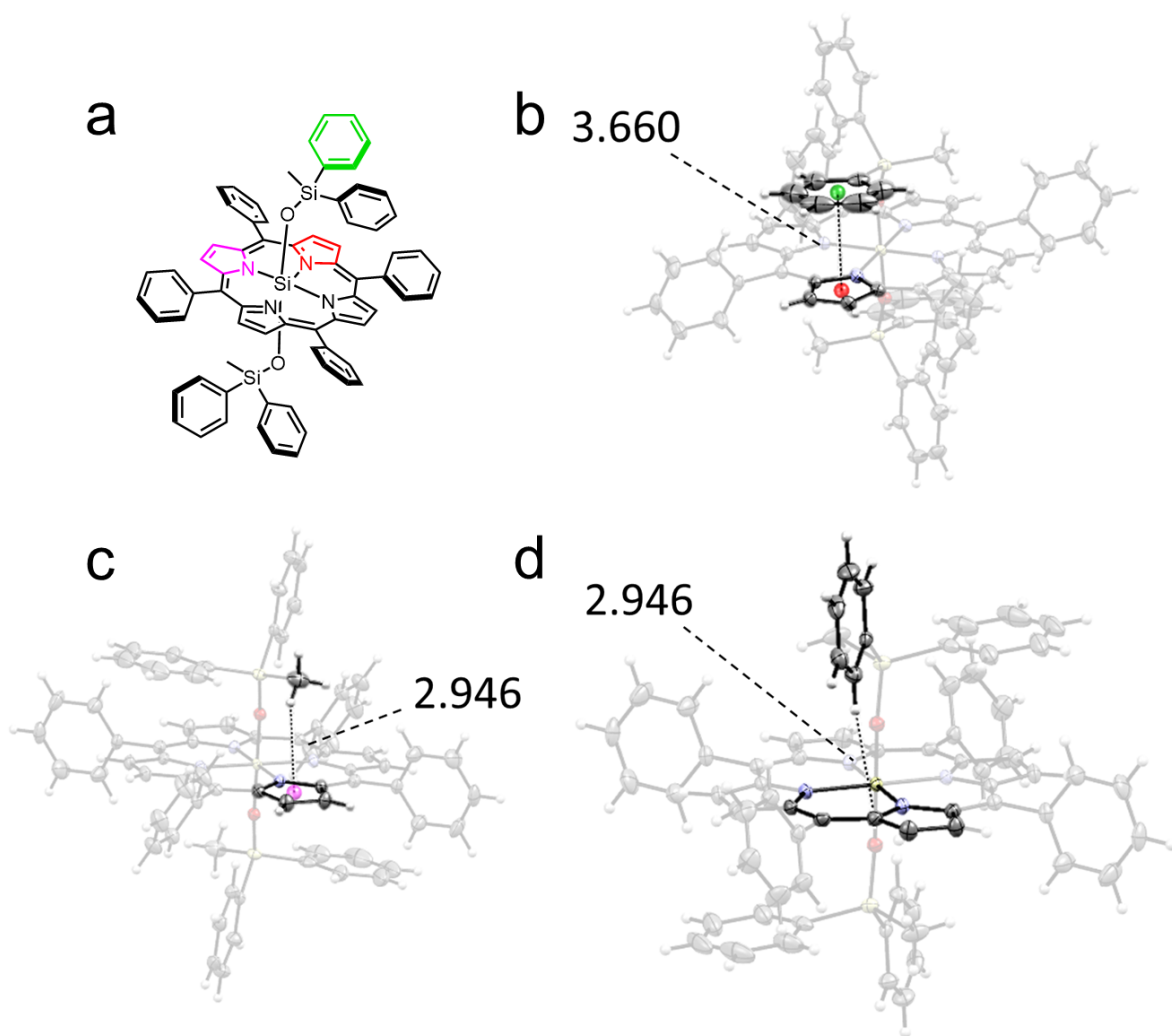


**Figure S50.** a) Structural formula of **1g** where centroids of rings are colored to match crystal structure centroids. b), c), and d) Four views of the solid-state structure showing intramolecular interactions of silyoxy cap with the porphyrin ring within/shorter than the sum of the van der Waals radii ( $\leq 3.8 \text{ \AA}$ ).

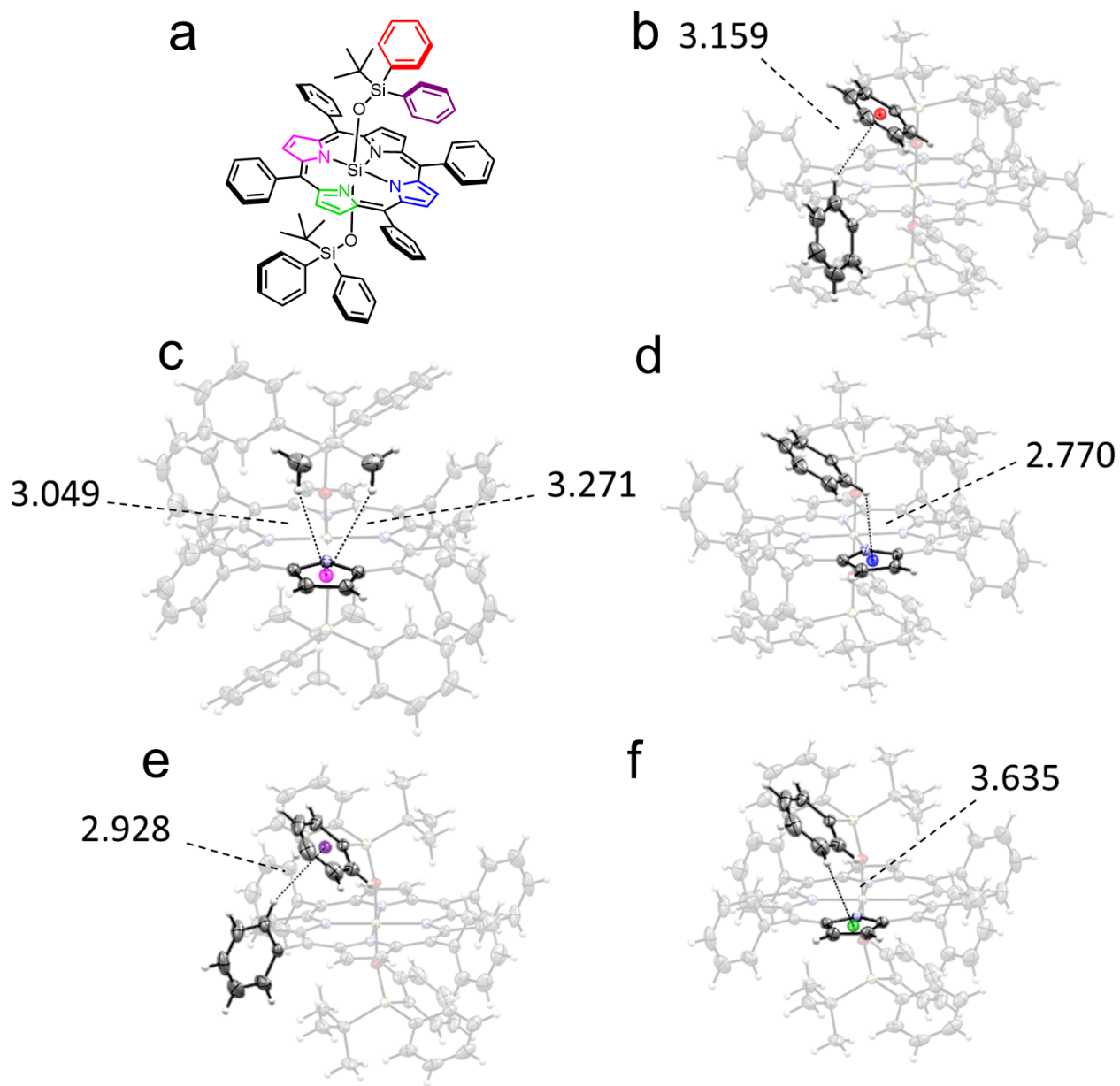


**Figure S51.** a) Structural formula of **1h** where centroids of rings are colored coded to match crystal structure centroids. b), c), d), e), and f) Five views of the solid-state structure showing intramolecular interactions of silyloxy cap with the porphyrin ring within/shorter than the sum of the van der Waals radii ( $\leq 3.8 \text{ \AA}$ ).

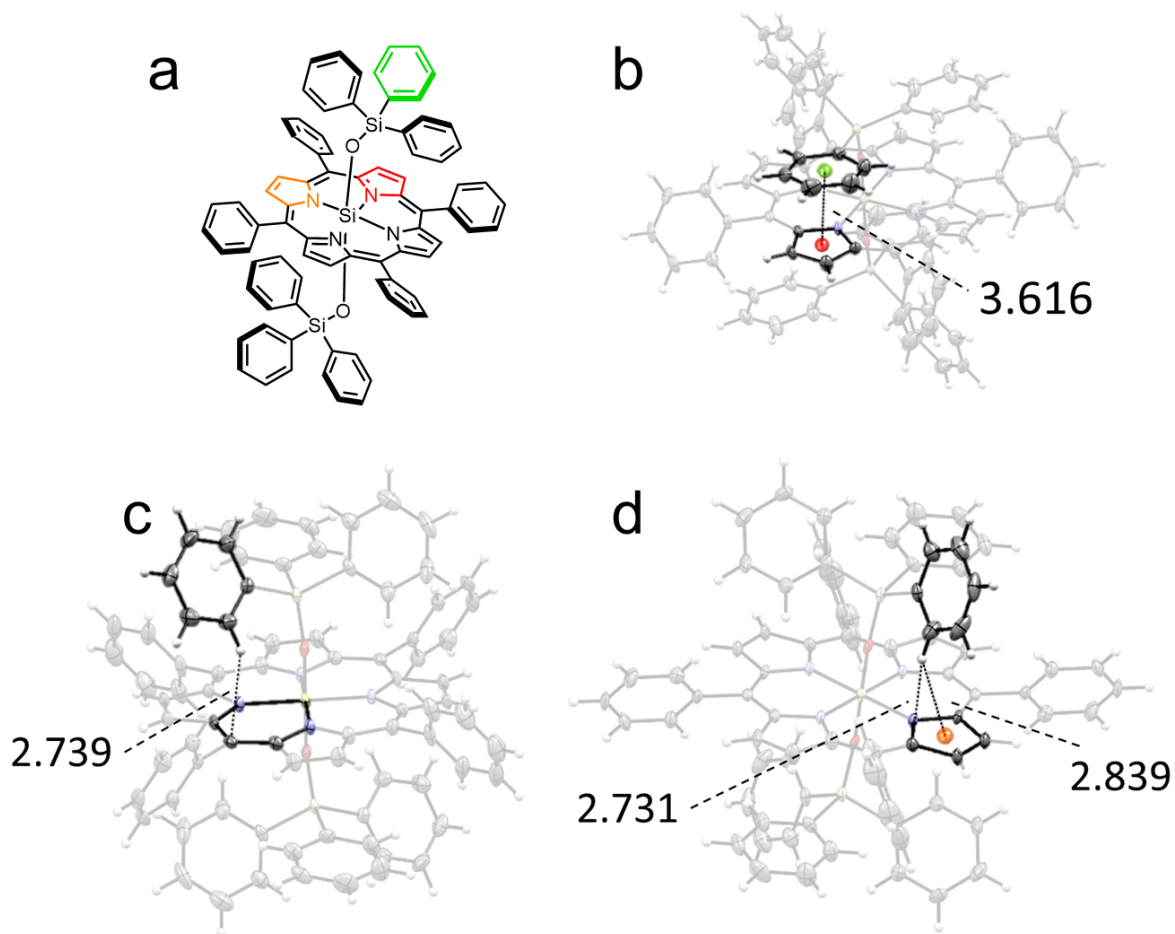


**Figure S52.** a) Structural formula of **1i'** where centroids of rings are colored coded to match crystal structure centroids. b), c), and d) Three views of the solid-state structure showing intramolecular interactions of silyloxy cap with the porphyrin ring within/shorter than the sum of the van der Waals radii ( $\leq 3.8 \text{ \AA}$ ).

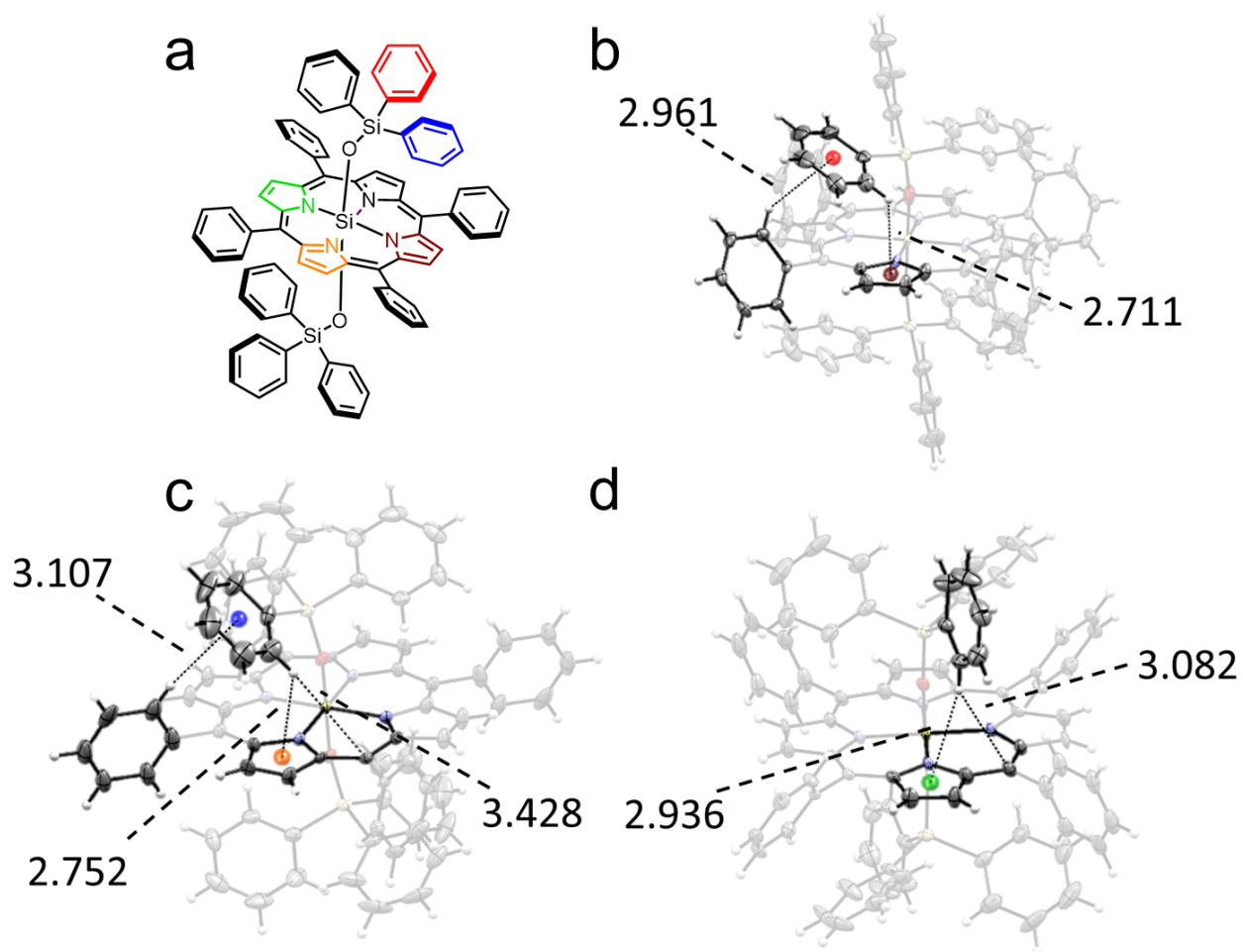


**Figure S53.** a) Structural formula of 1i'' where centroids of rings are colored coded to match crystal structure centroids. b), c), and d) Three views of the solid-state structure showing intramolecular interactions of silyloxy cap with the porphyrin ring within/shorter than the sum of the van der Waals radii ( $\leq 3.8 \text{ \AA}$ ).

## 8. *In Silico* Modelling

X-ray diffraction analysis shows that the porphyrin rings of **1f–1i** adopt a range of distorted conformations in solid state from ruffled to planar geometries. To determine the more stable conformation of these SOPS in solution, density functional theory (DFT) modelling was used to gain better insight into their conformational energetics. Select SOPs were optimized in Gaussian 09, Revision A.02,<sup>10</sup> to minima (confirmed by frequency calculations on the same level of theory having no imaginary frequency) using the M06–2X functional, 6-31G basis set, and a C-PCM solvent model for CH<sub>2</sub>Cl<sub>2</sub> (chosen as it is the solvent used for the majority of the physicochemical analysis). The calculations reveal (Figures S54–55) that the minimum energy geometries for all the alkyl (**1a**, **1c**, **1e**) and aryl (**1f**, **1g**) SOPS we modelled include a ruffled porphyrin core. The steric and electronic interactions between the silyloxy cap and the porphyrin ring system change the preferred porphyrin geometry from planar to nonplanar.



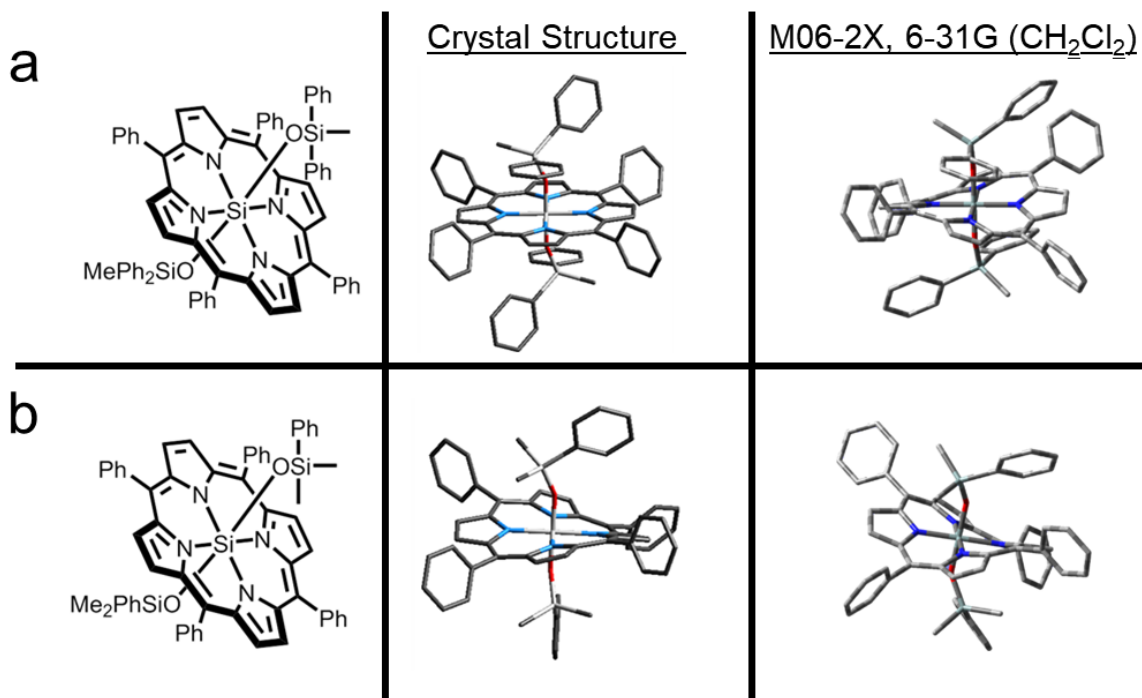


**Figure S54.** The DFT minimized structures in CH<sub>2</sub>Cl<sub>2</sub> compared to the X-Ray structure of a) **1f**, b) **1g** at M06-2X, using 6-31G basis set and a C-PCM solvent model for CH<sub>2</sub>Cl<sub>2</sub>.

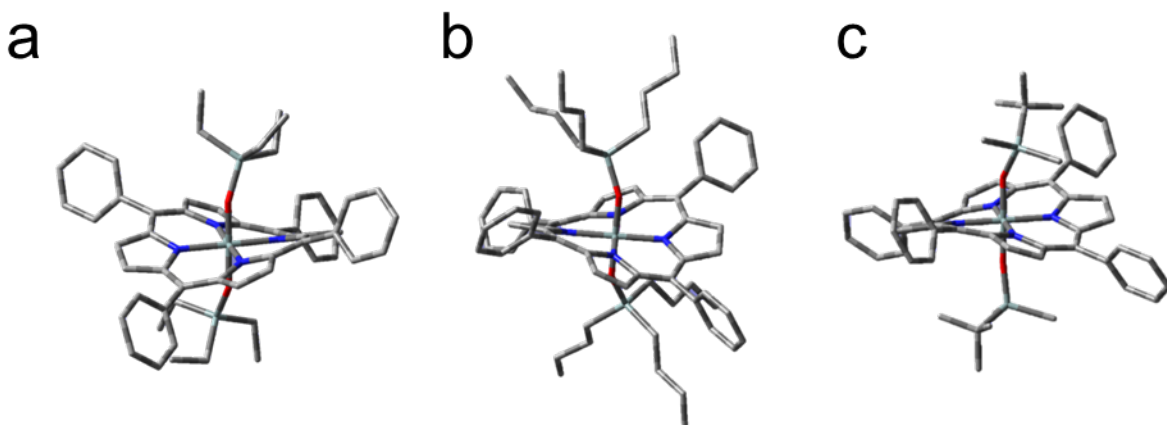


**Figure S55.** The DFT minimized structures in CH<sub>2</sub>Cl<sub>2</sub> of a) **1a**, b) **1e**, and c) **1c** at M06-2X, using 6-31G basis set and a C-PCM solvent model for CH<sub>2</sub>Cl<sub>2</sub>.

## 9. Hirshfeld Surface Analysis of Solid-State Structures

Hirshfeld surfaces<sup>11</sup> give insights into the interactions between molecules in the crystal lattices. We calculated Hirshfeld surfaces for the crystal packing structures of **1f-1i''/1i''** in CrystalExplorer17<sup>12</sup> using an isovalue of 0.5 and mapping the normalized contact distance,  $d_{\text{norm}}$ . The surfaces highlight (Figures S56–61) in red any regions in which the molecular surfaces meet at distances shorter than the sum of van der Waals radii, while white and blue illustrate regions where they meet at distances that are the sum of the van der Waals radii or longer, respectively.

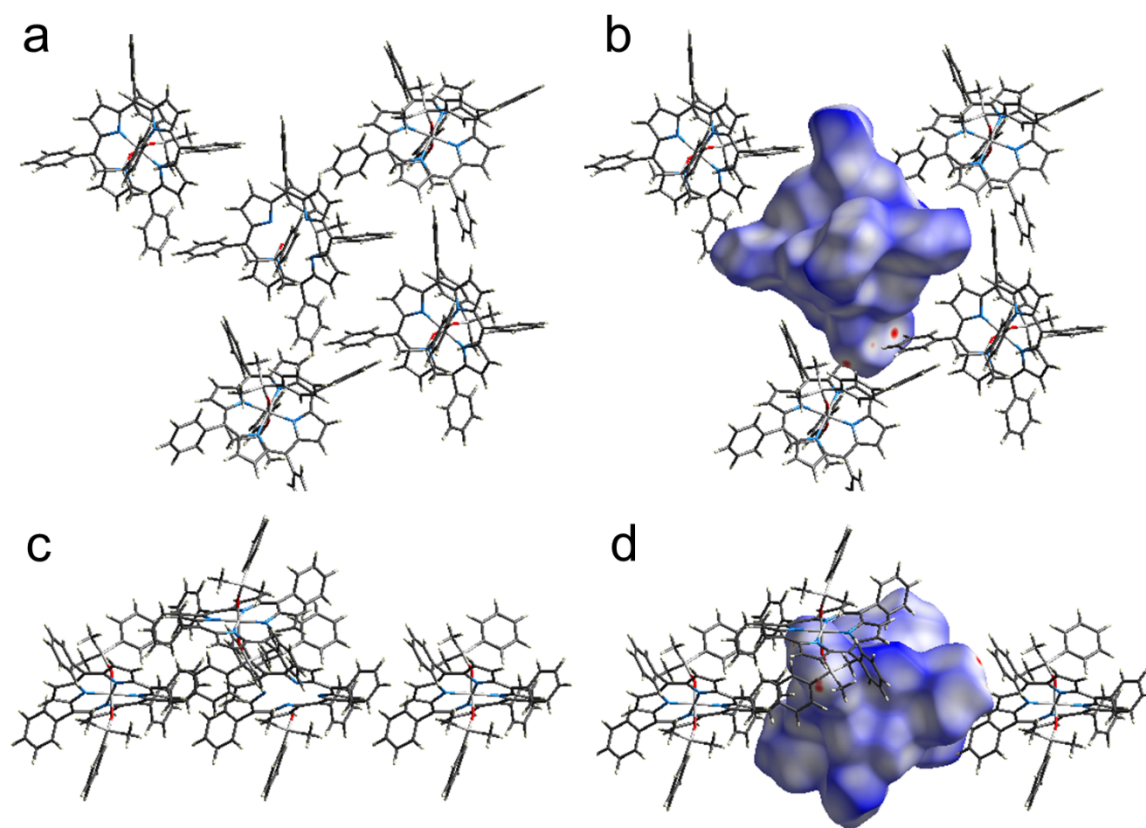


**Figure S56.** Hirshfeld surface of **1f**, showing the most significant close contacts, as well as views of the surface along the crystallographic a) and b) *a*-axis, and c) and d) *b*-axis.

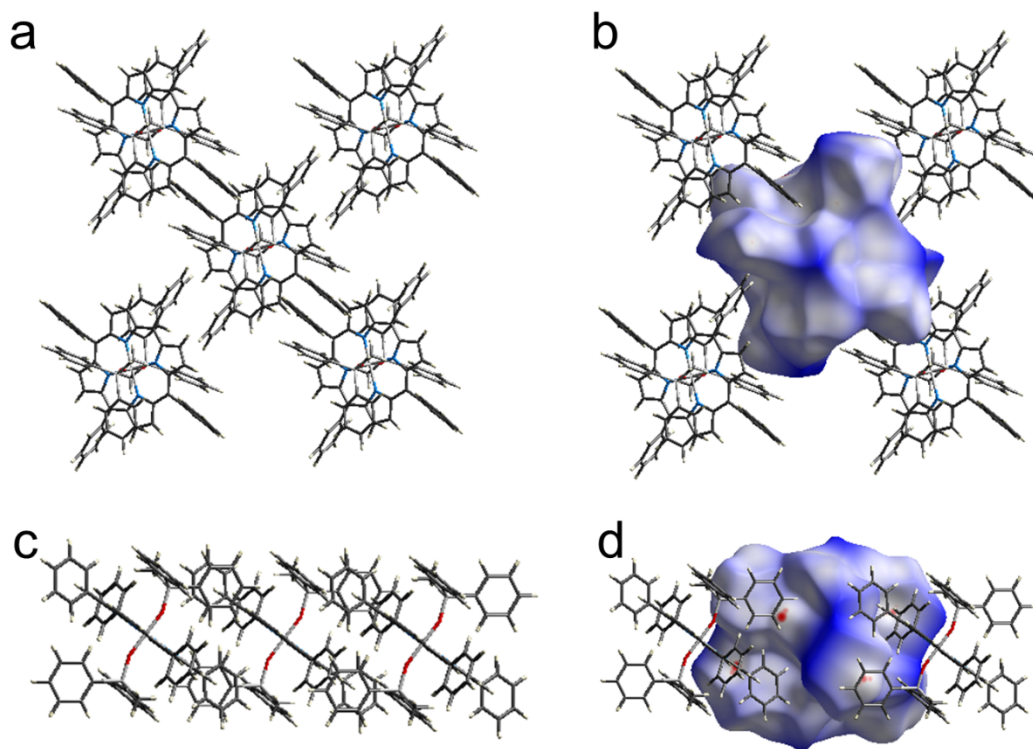


**Figure S57.** Hirshfeld surface of **1g**, showing the most significant close contacts, as well as views of the surface along the crystallographic a) and b) *a*-axis, and c) and d) *b*-axis.

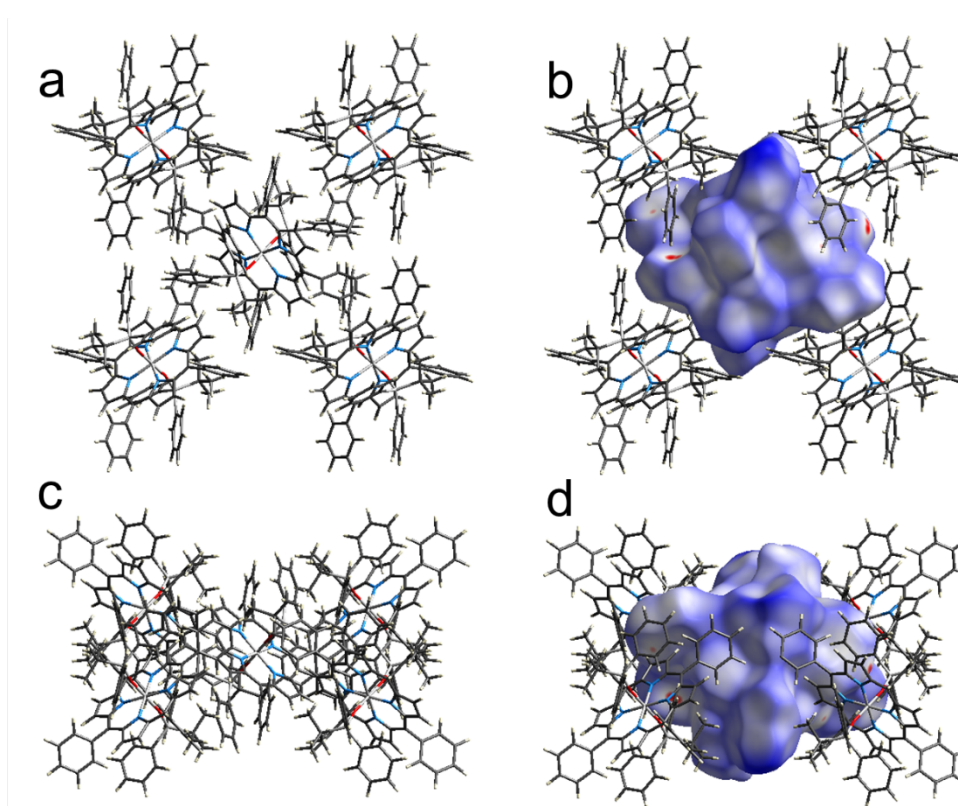


**Figure S58.** Hirshfeld surface of **1h**, showing the most significant close contacts, as well as views of the surface along the crystallographic a) and b) *a*-axis, and c) and d) *b*-axis.

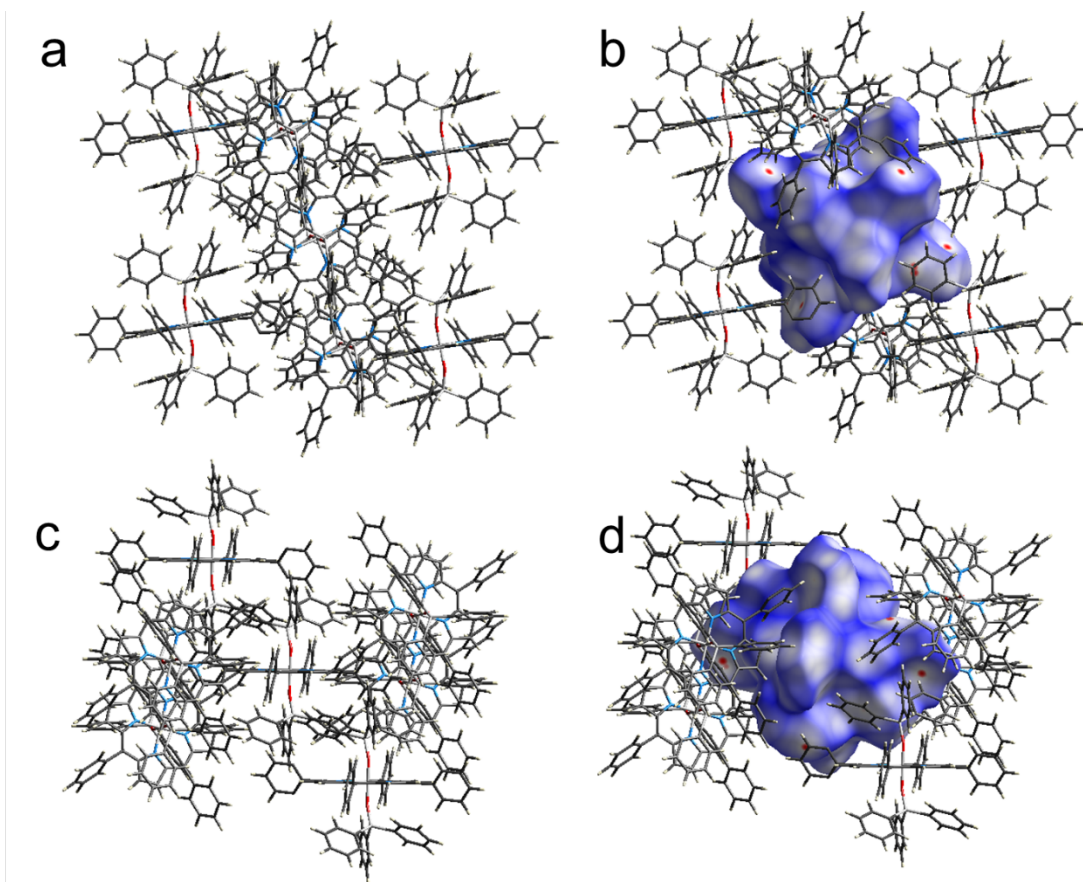


**Figure S59.** Hirshfeld surface of **1i'**, showing the most significant close contacts, as well as views of the surface along the crystallographic a) and b) *a*-axis, and c) and d) *b*-axis.

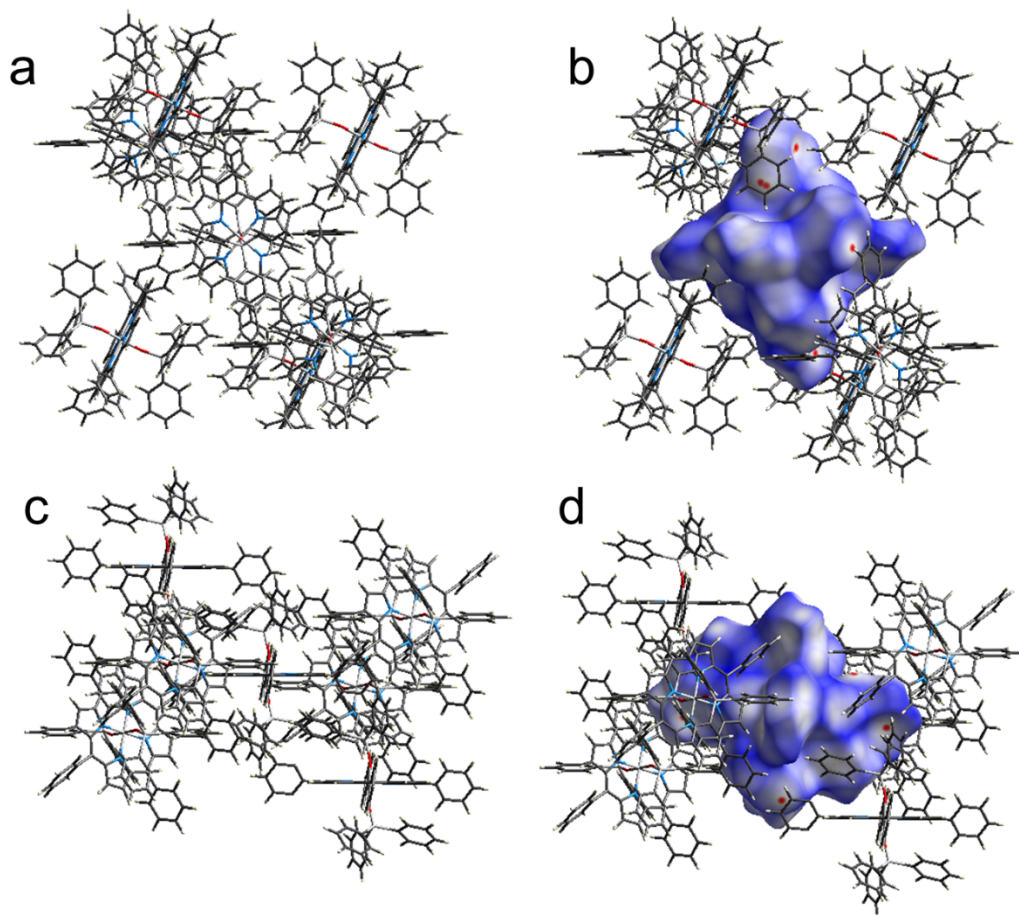


**Figure S60.** Hirshfeld surface of **1i''**, showing the most significant close contacts, as well as views of the surface along the crystallographic a) and b) *a*-axis, and c) and d) *b*-axis.

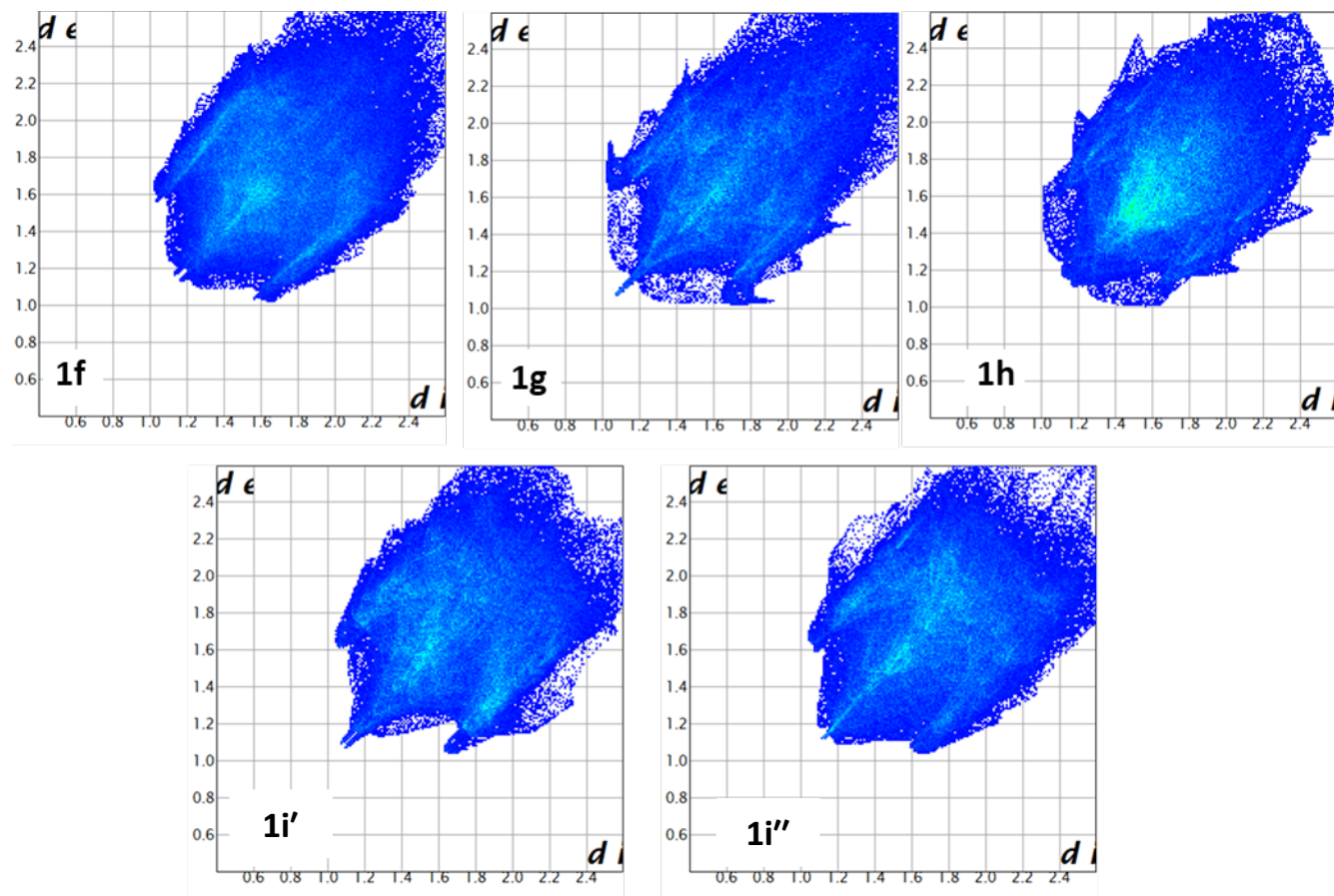


**Figure S61.** Calculated Hirshfeld fingerprints for the X-ray crystal structures of the aryl SOPS.

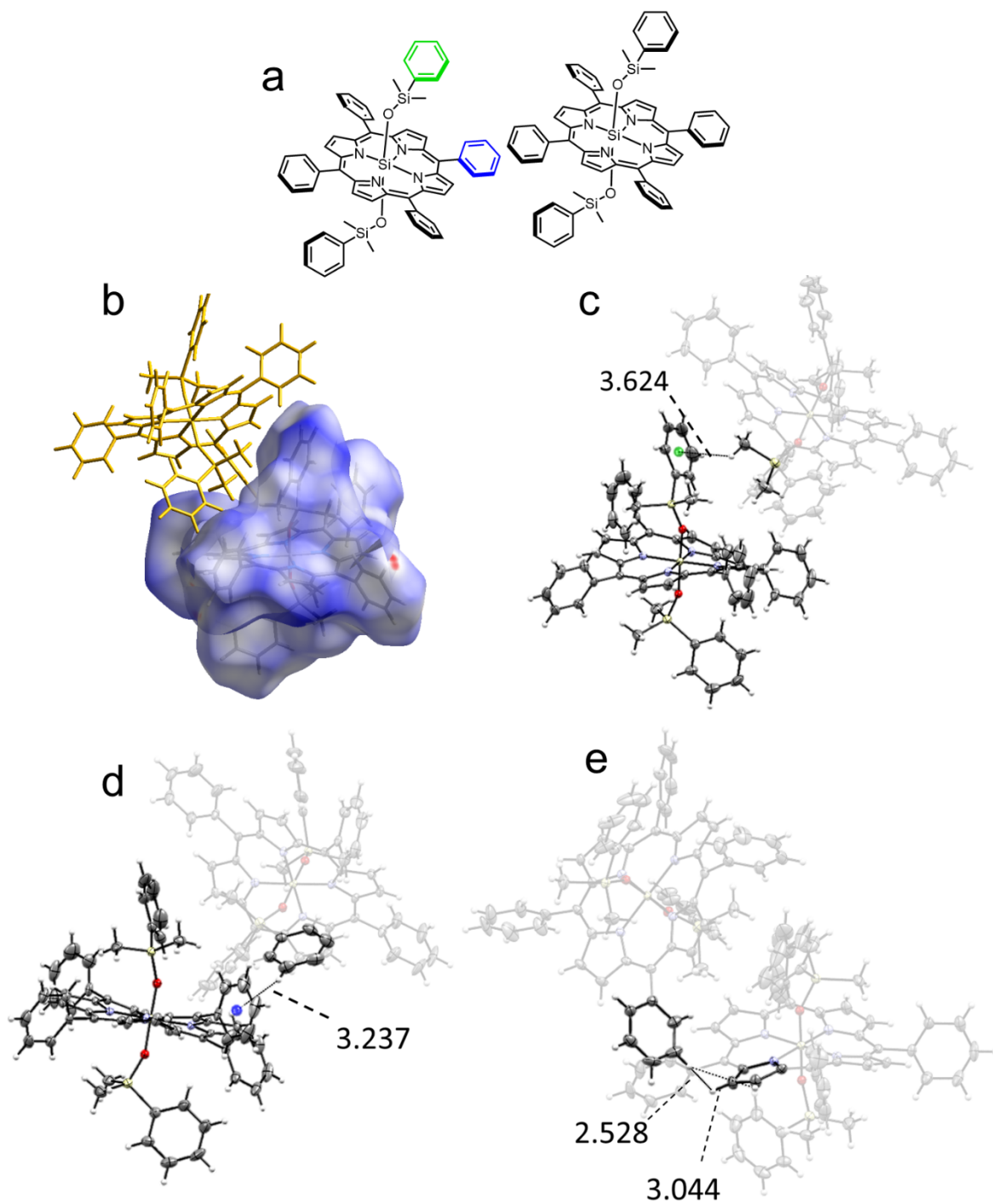


**Figure S62.** a) Structural formula of **1f** where centroids of rings are colored to match crystal structure centroids. b), c), d), and e) Intermolecular interactions of **1f** within/shorter than van der Waals radius ( $< 3.8 \text{ \AA}$ ). The **1f** structure determinant pair was found using crystal explorer using the Hirshfeld surface. The most dominant structure determinant pair is shown using Crystal Explorer with the Hirshfeld surface of the isolated molecule.



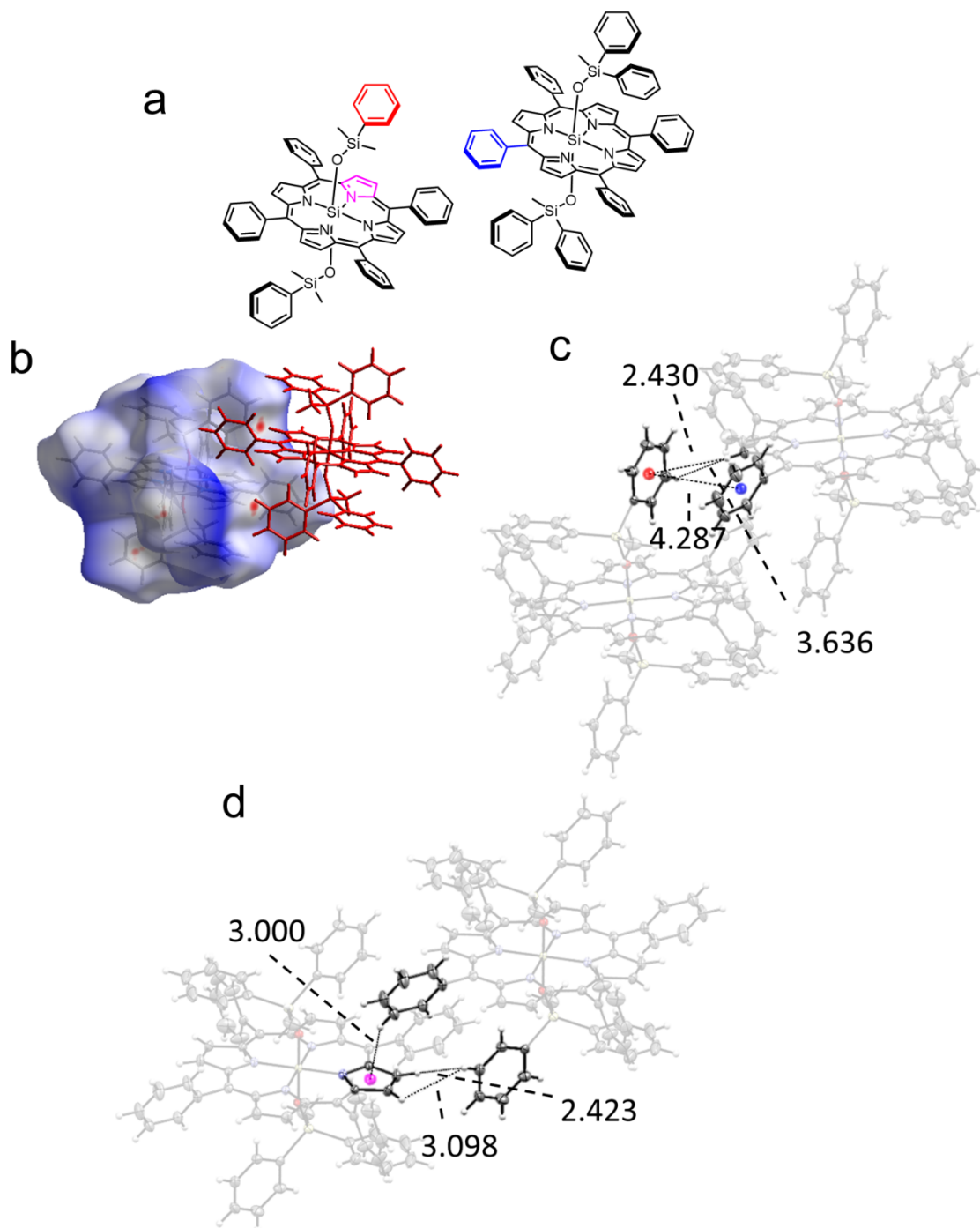


**Figure S63.** a) Structural formula of **1g** where centroids of rings are colored to match crystal structure centroids. b), c), and d) Intermolecular interactions of **1g** within/shorter than Vander Waals radius ( $< 3.8 \text{ \AA}$ ). The **1g** structure determinant pair was found using Crystal Explorer using the Hirshfeld surface. The most dominant structure determinant pair is shown using Crystal Explorer with the Hirshfeld surface of the isolated molecule.

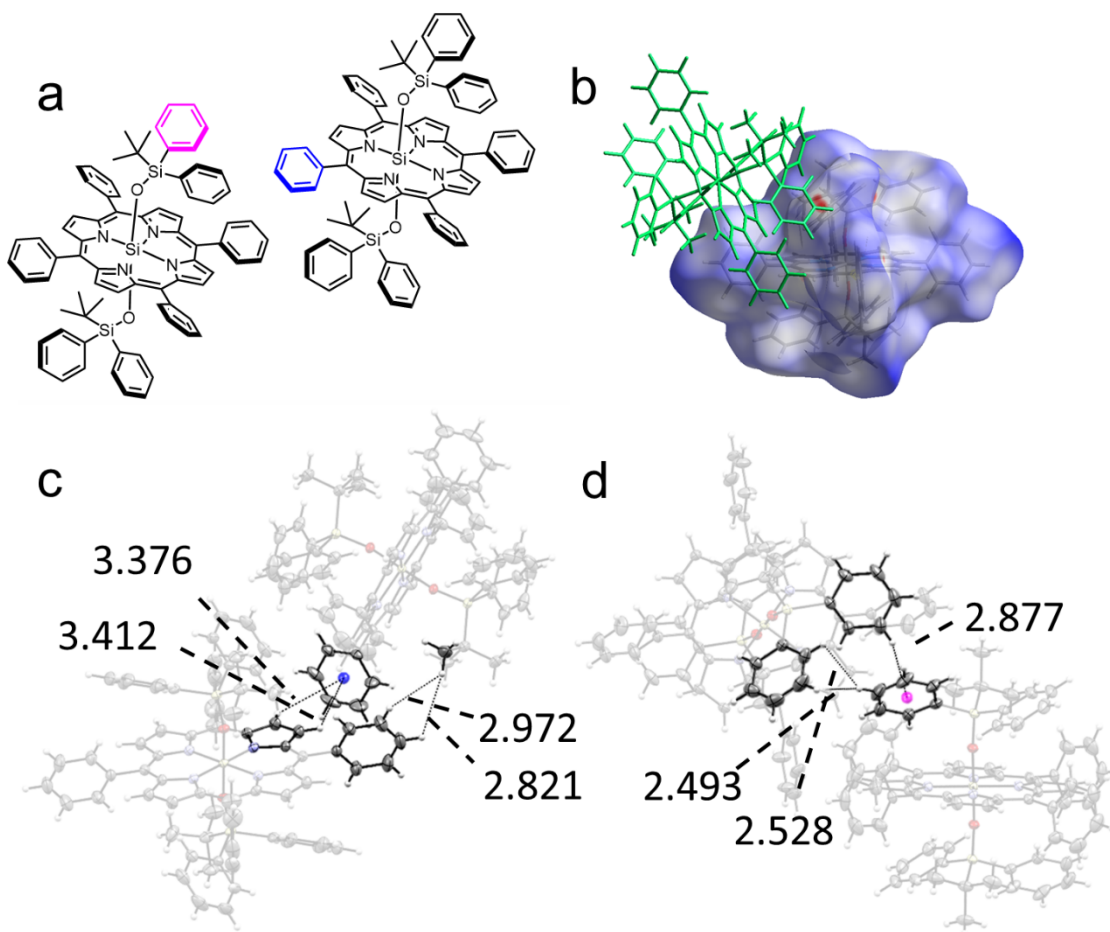


**Figure S64.** a) Structural formula of **1h** where centroids of rings are colored coded to match crystal structure centroids. b), c), and d) Intermolecular interactions of **1h** within/shorter than Vander Waals radius ( $< 3.8 \text{ \AA}$ ). The **1h** structure determinant pair was found using Crystal Explorer using the Hirshfeld surface. The most dominant structure determinant pair is shown using Crystal Explorer with the Hirshfeld surface of the isolated molecule.

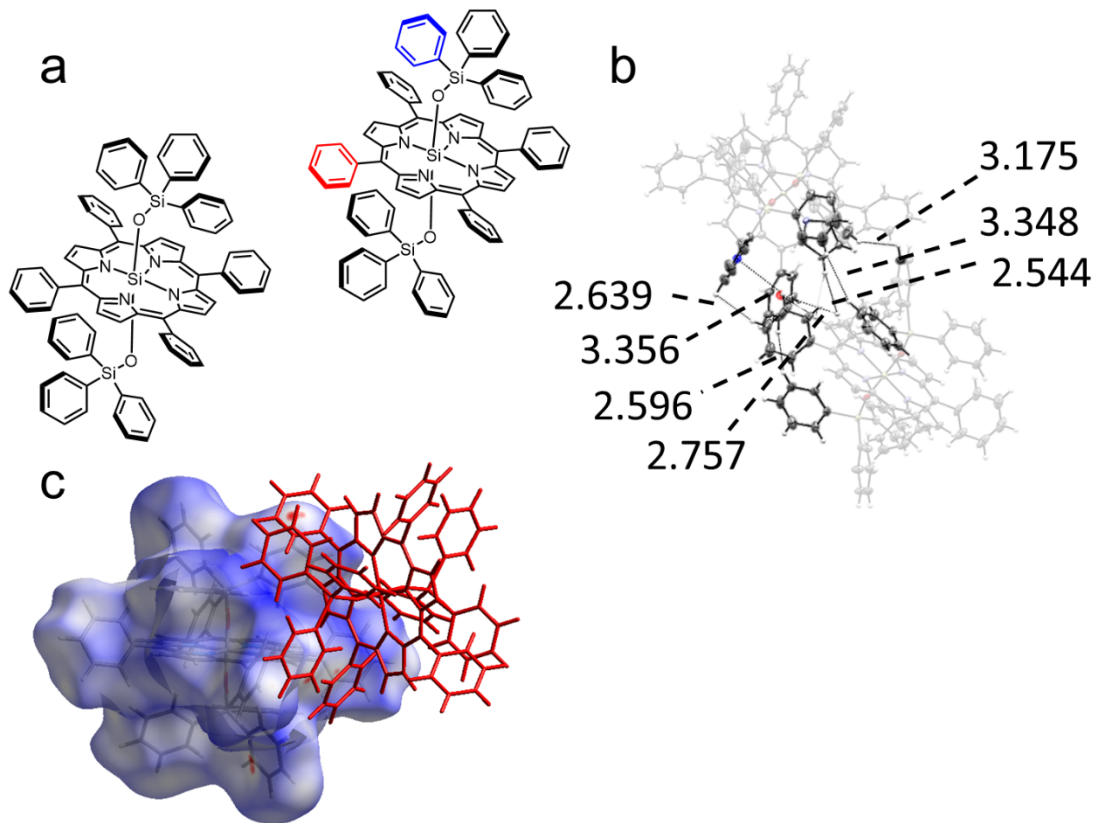


**Figure S65.** a) Structural formula of **1i** where centroids of rings are colored to match crystal structure centroids. b), c), and d) Intermolecular interactions of **1i/1i'** within/shorter than van der Waals radius (< 3.8 Å). The **1i'/1i''** structure determinant pair was found using Crystal Explorer using the Hirshfeld surface. The most dominant structure determinant pair is shown using Crystal Explorer with the Hirshfeld surface of the isolated molecule.

## 10. Calculation of Intermolecular Interaction Energies in the Solid State

We performed DFT calculations to quantify the interaction energies between neighboring molecules in the solid state using the CE-HF [HF/3-21G] theory and CE-B3LYP [B3LYP/6-31G(d,p)] energy model in CrystalExplorer17. Based on the X-ray crystal structure coordinates, a cluster was generated around a central molecule, extending to molecules that come within 3.8 Å of the central molecule at any point. As each of the crystal structures of **1f-h** have only one unique molecule in the unit cell ( $Z' = 1$ ), all of the surrounding molecules are related to the central molecule by a symmetry operation (labelled ‘Symmetry Op.’ in Tables S3–12). For the B3LYP [B3LYP/6-31G(d,p)] energy calculation, only the two most dominant structure determinant pairs were selected due to computational cost. Analysis was performed individually for the **1i/1i''** conformers present in the unit cell of the triphenyl derivative, generating a cluster of molecules around one of the conformers to model its local interactions. These energy calculations allow us to elucidate the total interaction energies ( $E_{\text{tot}}$ , in  $\text{kJ}\cdot\text{mol}^{-1}$ ) between neighboring molecules, based on the individual components for electrostatic ( $E_{\text{ele}}$ ), polarization ( $E_{\text{pol}}$ ), dispersion ( $E_{\text{dis}}$ ), and repulsion ( $E_{\text{rep}}$ ) energies. In each of the tables below, N indicates the number of molecules of a particular symmetry operation included in the cluster. R is the distance between the molecular centroids (mean atomic position) of the central molecule and the molecule generated by the given symmetry operation. A color code is given for each table entry, which matches the coloring of the relevant molecules in the corresponding cluster diagrams, Figures S66–70.

**Table S3.** Calculated intermolecular interaction energies (in  $\text{kJ}\cdot\text{mol}^{-1}$ ) for the solid-state structure of **1f** at CE-HF-321G theory.

	<b>N</b>	<b>Symmetry Op.</b>	<b>R/Å</b>	<b><math>E_{\text{ele}}</math></b>	<b><math>E_{\text{pol}}</math></b>	<b><math>E_{\text{dis}}</math></b>	<b><math>E_{\text{rep}}</math></b>	<b><math>E_{\text{tot}}</math></b>
	2	x, y, z	12.82	-13.1	-2.4	-47.8	26.1	-36.9
	2	x+1/2, -y+1/2, z+1/2	9.81	-4.9	-5.2	-98.8	39.6	-65.2
	2	x+1/2, -y+1/2, z+1/2	12.04	-8.5	-4.8	-75.5	30.8	-54.9
	2	-x+1/2, y+1/2, -z+1/2	13.07	-9.2	-2.7	-43.1	24.0	-30.5
	2	-x+1/2, y+1/2, -z+1/2	15.46	-4.5	-1.2	-18.9	6.1	-17.4
	1	-x, -y, -z	13.18	-11.2	-1.8	-37.0	15.4	-33.4
	1	-x, -y, -z	10.56	-7.0	-2.1	-69.0	22.4	-52.5
	1	-x, -y, -z	17.18	-2.6	-0.4	-8.6	2.7	-8.5

**Table S4.** Select calculated intermolecular interaction energies (in  $\text{kJ}\cdot\text{mol}^{-1}$ ) for the solid-state structure of **1f** at CE-B3LYP-631G (d,p) theory.

	<b>N</b>	<b>Symmetry Op.</b>	<b>R/Å</b>	<b><math>E_{\text{ele}}</math></b>	<b><math>E_{\text{pol}}</math></b>	<b><math>E_{\text{dis}}</math></b>	<b><math>E_{\text{rep}}</math></b>	<b><math>E_{\text{tot}}</math></b>
	2	x+1/2, -y+1/2, z+1/2	9.81	-9.6	-2.5	-98.8	50.6	-66.8
	2	x+1/2, -y+1/2, z+1/2	12.04	-9.7	-2.4	-75.5	39.4	-53.5

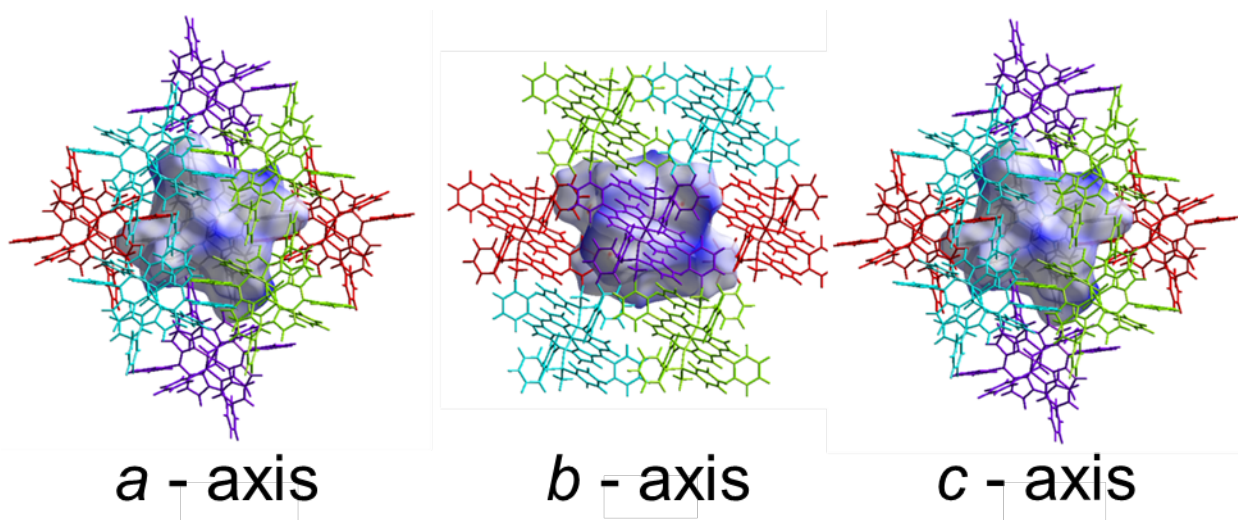


**Figure S66.** The cluster of molecules used to model intermolecular interaction energies of **1f** listed in Table S2 and Table S3. The central molecule is colored according to Hirshfeld surface and surrounding molecules are colored to match the color code in Table S3 and Table S4.

**Table S5.** Calculated intermolecular interaction energies (in  $\text{kJ}\cdot\text{mol}^{-1}$ ) for the solid-state structure of **1g** at CE-HF-321G theory.

	<b>N</b>	<b>Symmetry Op.</b>	<b>R/Å</b>	<b><math>E_{\text{ele}}</math></b>	<b><math>E_{\text{pol}}</math></b>	<b><math>E_{\text{dis}}</math></b>	<b><math>E_{\text{rep}}</math></b>	<b><math>E_{\text{tot}}</math></b>
	2	x, y, z	11.60	-9.2	-6.7	-109.0	47.1	-73.8
	4	-x+1/2, y+1/2, -z+1/2	13.01	-10.6	-3.6	-51.3	20.2	-43.0
	4	-x+1/2, y+1/2, -z+1/2	14.23	-0.2	-1.0	-19.1	6.8	-12.5
	2	x, y, z	12.57	-24.6	-7.3	-79.5	40.5	-68.6

**Table S6.** Select calculated intermolecular interaction energies (in  $\text{kJ}\cdot\text{mol}^{-1}$ ) for the solid-state structure of **1g** at CE-B3LYP-631G (d,p) theory.

	<b>N</b>	<b>Symmetry Op.</b>	<b>R/Å</b>	<b><math>E_{\text{ele}}</math></b>	<b><math>E_{\text{pol}}</math></b>	<b><math>E_{\text{dis}}</math></b>	<b><math>E_{\text{rep}}</math></b>	<b><math>E_{\text{tot}}</math></b>
	2	x, y, z	11.60	-13.9	-3.3	-109.0	60.2	-74.9
	4	-x+1/2, y+1/2, -z+1/2	13.01	-8.7	-1.7	-51.3	25.7	-39.3
	4	-x+1/2, y+1/2, -z+1/2	14.23	-1.9	-0.5	-19.1	9.2	-13.3
	2	x, y, z	12.57	-20.5	-3.5	-79.5	51.4	-61.7

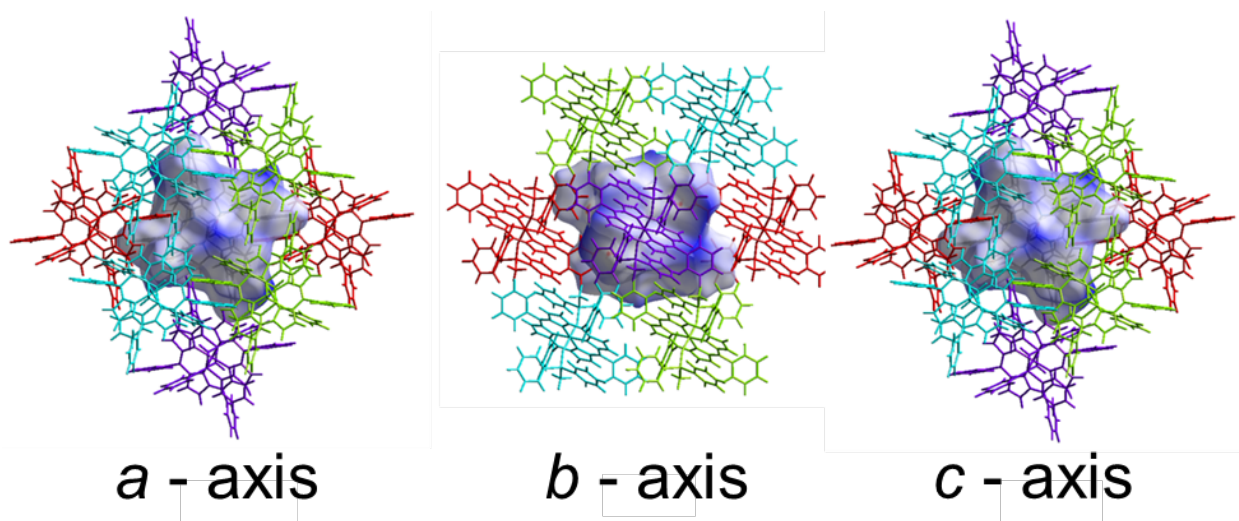


**Figure S67.** The cluster of molecules used to model intermolecular interaction energies of **1g** listed in Table S4 and Table S5. The central molecule is colored according to Hirshfeld surface and surrounding molecules are colored to match the color code in Table S5 and Table S6.

**Table S7.** Calculated intermolecular interaction energies (in  $\text{kJ}\cdot\text{mol}^{-1}$ ) for the solid-state structure of **1h** at CE-HF-321G theory

	<b>N</b>	<b>Symmetry Op.</b>	<b>R/Å</b>	<b><math>E_{\text{ele}}</math></b>	<b><math>E_{\text{pol}}</math></b>	<b><math>E_{\text{dis}}</math></b>	<b><math>E_{\text{rep}}</math></b>	<b><math>E_{\text{tot}}</math></b>
	4	$-y+3/4, x+1/4, z+1/4$	14.48	-6.2	-1.6	-31.5	15.0	-23.6
	2	$x, y, z$	12.34	-11.1	-3.0	-74.0	31.7	-54.2
	4	$y+3/4, -x+3/4, z+3/4$	11.55	-10.9	-4.7	-105.1	44.2	-73.0
	4	$-x+1/2, -y, z+1/2$	16.91	-3.1	-0.4	-10.5	5.0	-8.7
	2	$-x, -y+1/2, z$	15.75	-1.2	-0.3	-9.9	2.1	-8.6





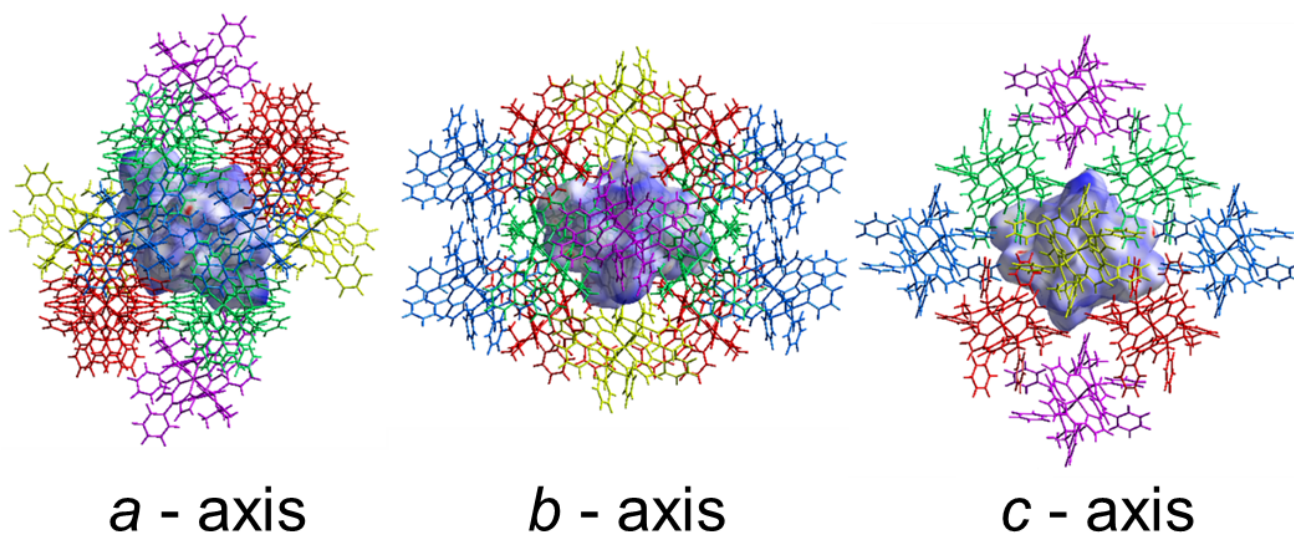



**Table S8.** Select calculated intermolecular interaction energies (in  $\text{kJ}\cdot\text{mol}^{-1}$ ) for the solid-state structure of **1h** at CE-B3LYP-631G (d,p) theory

	<b>N</b>	<b>Symmetry Op.</b>	<b>R/Å</b>	<b><math>E_{\text{ele}}</math></b>	<b><math>E_{\text{pol}}</math></b>	<b><math>E_{\text{dis}}</math></b>	<b><math>E_{\text{rep}}</math></b>	<b><math>E_{\text{tot}}</math></b>
	2	$x, y, z$	12.34	-10.7	-1.4	-74.0	39.2	-52.6
	4	$y+3/4, -x+3/4, z+3/4$	11.55	-13.5	-2.2	-105.1	55.5	-73.2





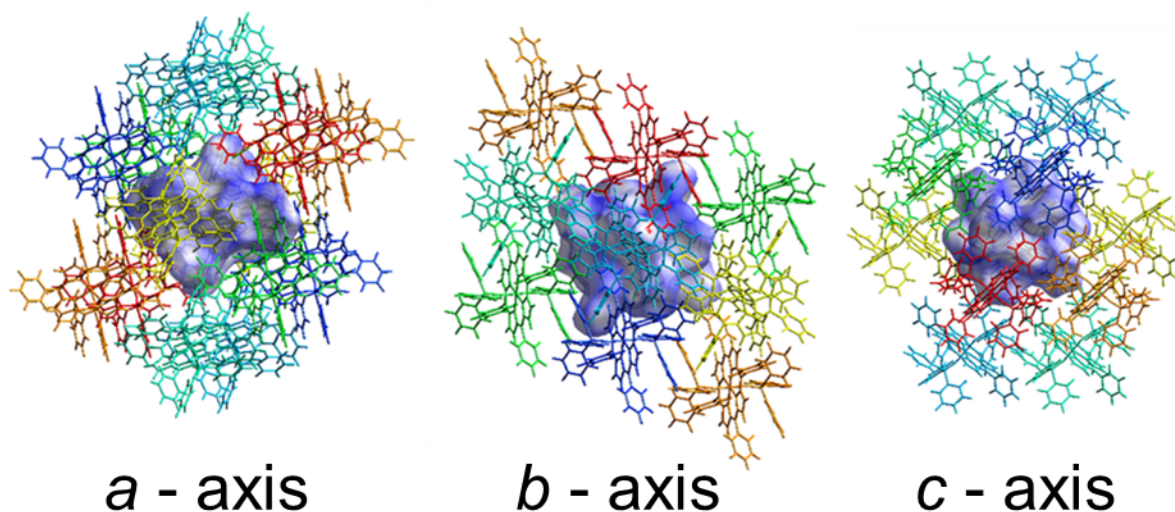
**Figure S68.** The cluster of molecules used to model intermolecular interaction energies of **1h** listed in Table S6 and Table S7. The central molecule is colored according to Hirshfeld surface and surrounding molecules are colored to match the color code in Table S7 and Table S8.

**Table S9.** Calculated intermolecular interaction energies (in  $\text{kJ}\cdot\text{mol}^{-1}$ ) for the solid-state structure of **1i'** at CE-HF-321G theory

	<b>N</b>	<b>Symmetry Op.</b>	<b>R/Å</b>	<b>E<sub>ele</sub></b>	<b>E<sub>pol</sub></b>	<b>E<sub>dis</sub></b>	<b>E<sub>rep</sub></b>	<b>E<sub>tot</sub></b>
	2	-	11.70	-25.6	-5.5	-107.3	52.1	-84.2
	2	-	17.02	-1.4	-0.5	-12.7	5.9	-8.4
	2	x, y, z	12.81	-22.2	-8.5	-100.5	43.5	-83.4
	2	-	17.66	-0.2	-0.2	-5.3	0.4	-4.8
	2	x, y, z	15.24	-8.6	-1.9	-32.9	16.7	-26.1
	2	x, y, z	14.85	-2.0	-2.4	-23.0	6.3	-19.2
	2	-	12.16	-12.8	-8.0	-74.9	28.7	-62.5

**Table S10.** Select calculated intermolecular interaction energies (in  $\text{kJ}\cdot\text{mol}^{-1}$ ) for the solid-state structure of **1i'** at CE-B3LYP-631G (d,p) theory








	<b>N</b>	<b>Symmetry Op.</b>	<b>R/Å</b>	<b>E<sub>ele</sub></b>	<b>E<sub>pol</sub></b>	<b>E<sub>dis</sub></b>	<b>E<sub>rep</sub></b>	<b>E<sub>tot</sub></b>
	2	-	11.70	-22.5	-2.6	-107.3	65.4	-78.7
	2	x, y, z	12.81	-19.6	-4.1	-100.5	56.0	-76.7





**Figure S69.** The cluster of molecules used to model intermolecular interaction energies for **1i** listed in Table S8 and Table S9. The central molecule is colored according to Hirshfeld surface and surrounding molecules are colored to match the color code in Table S9 and Table S10.



**Table S11.** Calculated intermolecular interaction energies (in  $\text{kJ}\cdot\text{mol}^{-1}$ ) for the solid-state structure of **1i''** at CE-HF-321G theory .

	N	Symmetry Op.	R/Å	E <sub>ele</sub>	E <sub>pol</sub>	E <sub>dis</sub>	E <sub>rep</sub>	E <sub>tot</sub>
	2	-	11.70	-25.6	-5.5	-107.3	52.1	-84.2
	2	-	17.02	-1.4	-0.5	-12.7	5.9	-8.4
	2	-	17.66	-0.2	-0.2	-5.3	0.4	-4.8
	2	-	13.06	-6.7	-3.4	-57.5	19.7	-44.9
	2	-	12.16	-12.8	-8.0	-74.9	28.7	-62.5
	2	x, y, z	12.81	-13.0	-3.2	-86.5	44.8	-57.0
	2	x, y, z	15.24	1.5	-0.5	-15.9	4.9	-9.1

**Table S12.** Select calculated intermolecular interaction energies (in  $\text{kJ}\cdot\text{mol}^{-1}$ ) for the solid-state structure of **1i''** at CE-B3LYP-631G (d,p) theory.

	N	Symmetry Op.	R/Å	E <sub>ele</sub>	E <sub>pol</sub>	E <sub>dis</sub>	E <sub>rep</sub>	E <sub>tot</sub>
	2	-	11.70	-22.5	-2.6	-107.3	65.4	-78.7
	2	x, y, z	12.81	-14.9	-1.5	-86.5	55.8	-57.8

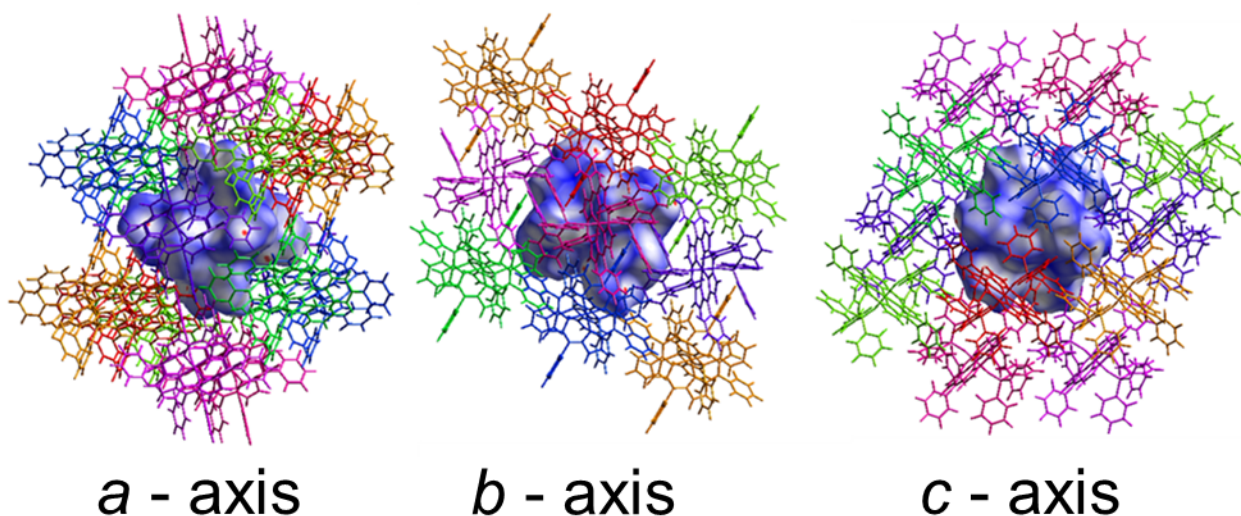


**Figure S70.** The cluster of molecules used to model intermolecular interaction energies for **1i'** listed in Table S10 and Table S11. The central molecule is colored according to Hirshfeld surface and surrounding molecules are colored to match the color code in Table S11 and Table S12.

## 11. Compound Identity Validation by Low Resolution Mass Spectra

In some cases we were unable to obtain high resolution mass spectra. For these compounds, we further characterize them by comparing zoomed isotopic distributions of the  $M^+$  peaks. These low resolution mass spectrometry (MS) results were acquired by AIMS Mass Spectrometry Laboratory at University of Toronto on a Waters GCT Premier instrument. The spectra shown were run in EI+ mode using the heated solids probe. The isotopic abundance pattern was computed using the Waters *MassLynx* software.

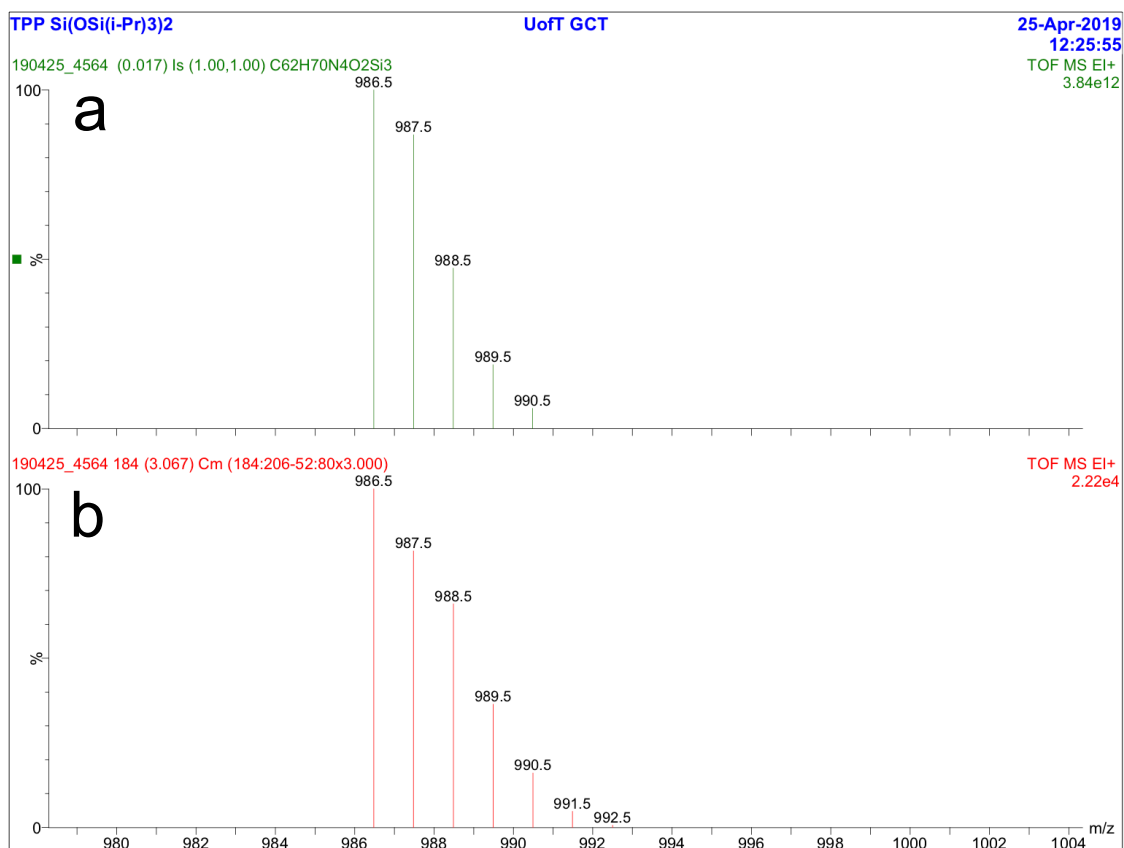


**Figure S71.** Characterization of **1b** using isotopic distribution in low resolution mass spectrometry. a) Predicted isotopic distribution and b) observed isotopic distribution.

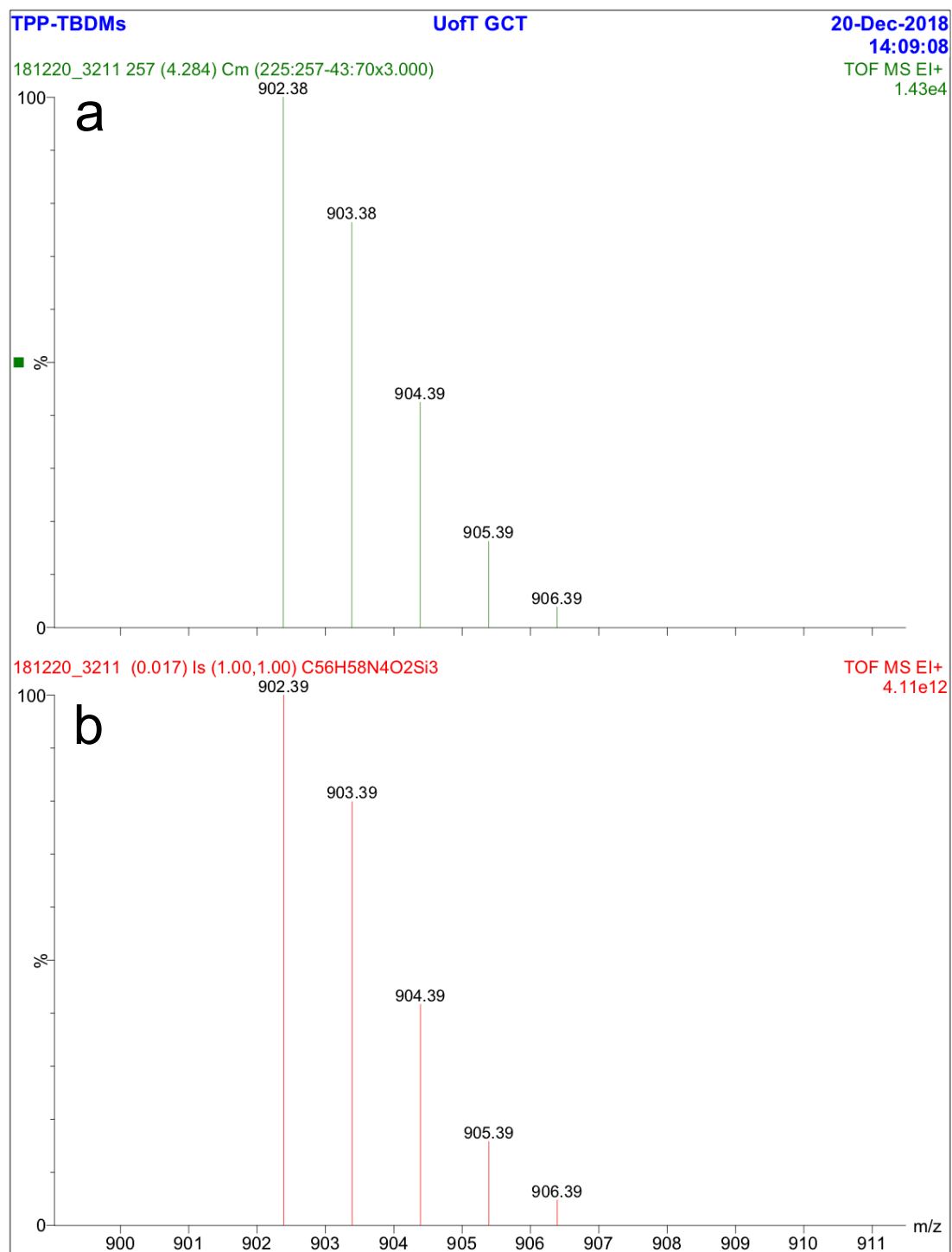


**Figure S72.** Characterization of **1c** using isotopic distribution in low resolution mass spectrometry. a) Predicted isotopic distribution and b) observed isotopic distribution.

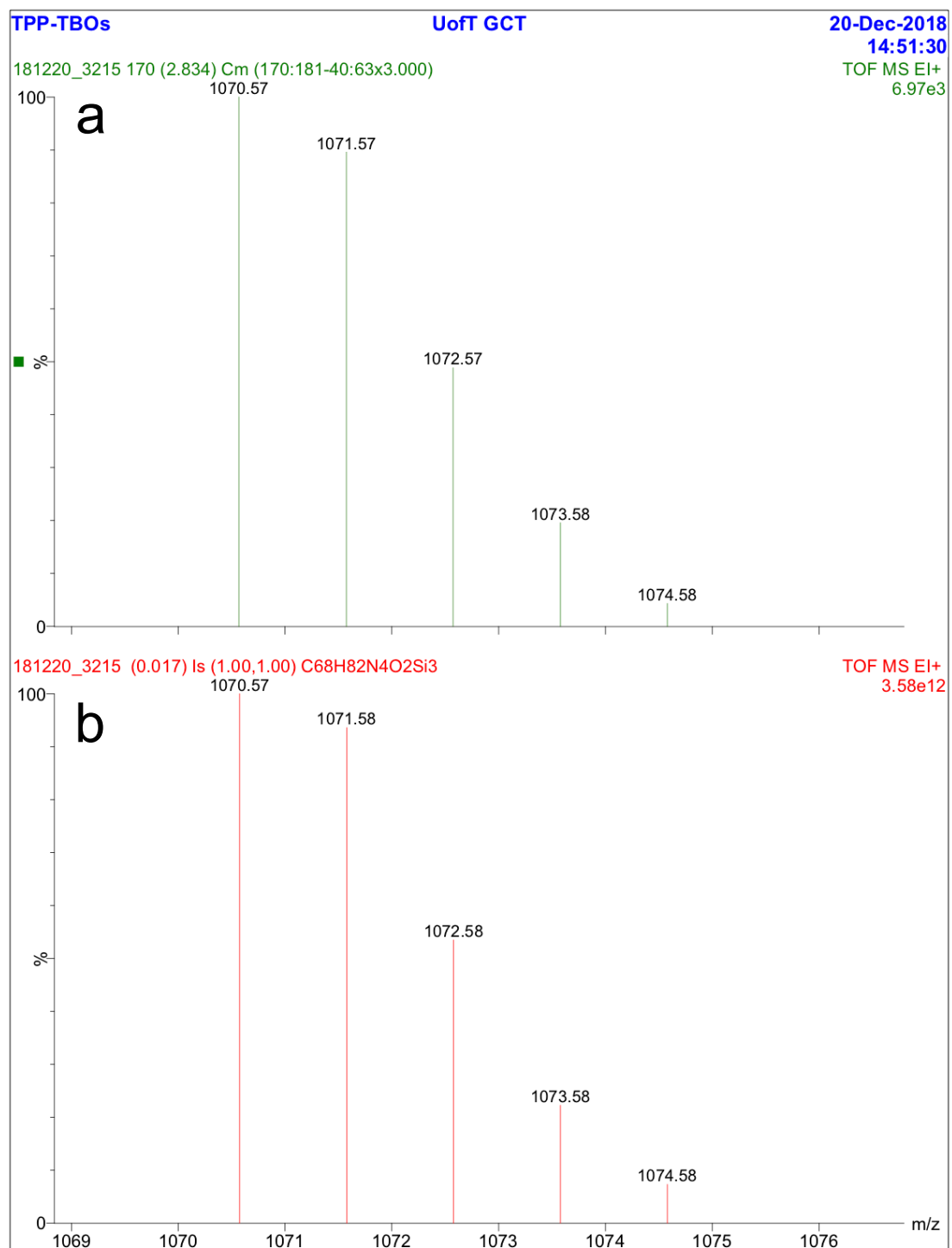


**Figure S73.** Characterization of **1d** using isotopic distribution in low resolution mass spectrometry. a) Predicted isotopic distribution and b) observed isotopic distribution.

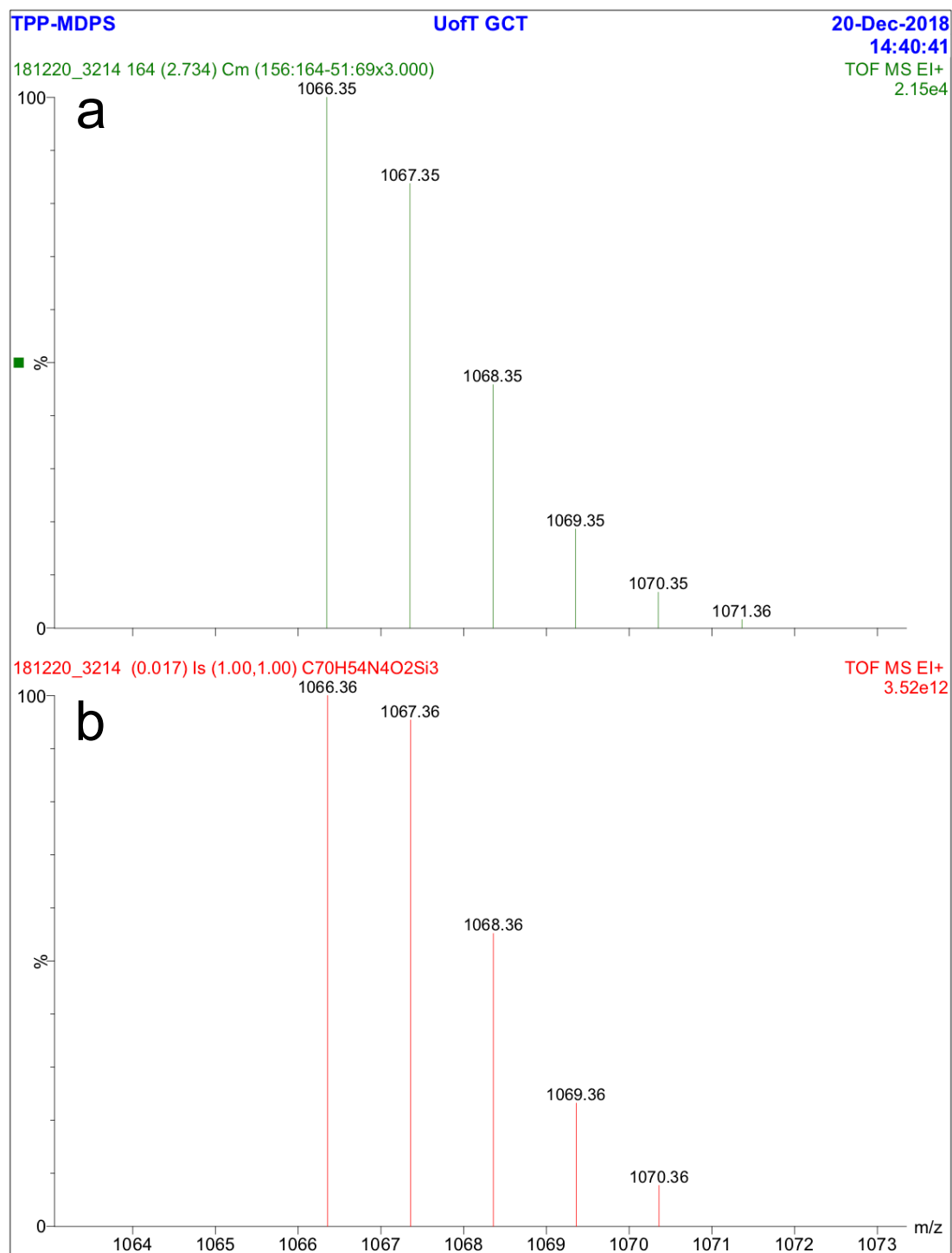


**Figure S74.** Characterization of **1g** using isotopic distribution in low resolution mass spectrometry. a) Predicted isotopic distribution and b) observed isotopic distribution.

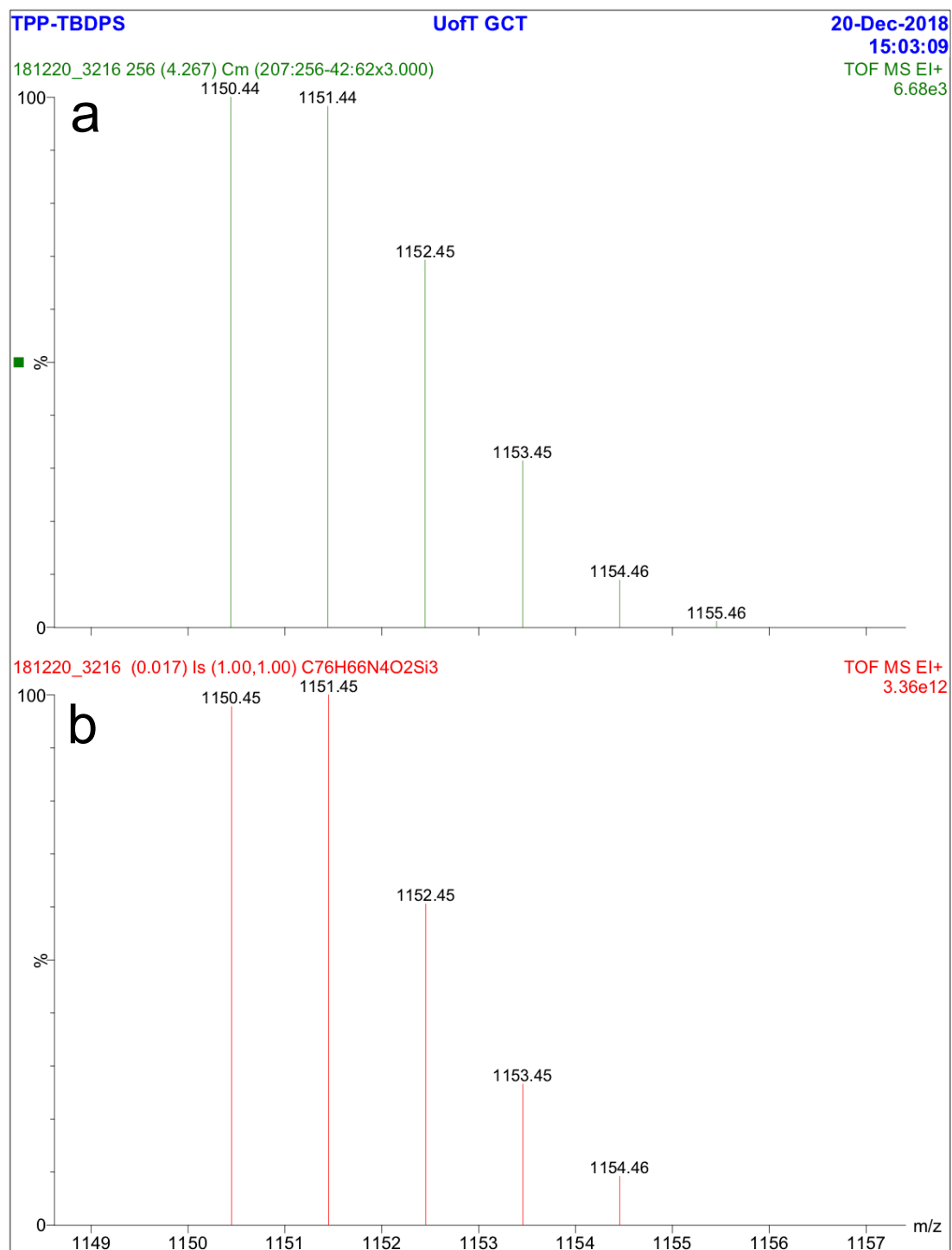


**Figure S75.** Characterization of **1h** using isotopic distribution in low resolution mass spectrometry. a) Predicted isotopic distribution and b) observed isotopic distribution.

## 12. References

- (1) a) Marsh, D.F.; Falvo, R.E.; Mink, L.M. Microscale synthesis and  $^1\text{H}$  NMR analysis of tetraphenylporphyrins. *J. Chem. Ed.* **1999**, *76*(2), 237-239. b) Mohajer, D.; Zakavi, S.; Rayati, S.; Zahedi, M.; Safari, N.; Khavasi, H.R.; Shahbazian, S. Unique 1:2 adduct formation of *meso*-tetraarylporphyrins and *meso*-tetraalkylporphyrins with  $\text{BF}_3$ : a spectroscopic and *ab initio* study. *New J. Chem.* **2004**, *28*(12), 1600-1607.
- (2) Ishida, S.; Yoshimura, K.; Matsumoto, H.; Kyushin, S. Selective Si–C Bond Cleavage on a Diorganosilicon Porphyrin Complex Bearing Different Axial Ligands *Chem. Lett.* **2009**, *38*(4), 362-363.
- (3) a) Kane, K.M.; Lorenz, C.R.; Heilman, D.M.; Lemke, F.R. Substituent Effects on the Spectroscopic Properties and Reactivity of Hexacoordinate Silicon(IV) Porphyrin Complexes *Inorg. Chem.* **1998**, *37*, 669-673 b) Liu, J.; Yang, X.; Sun, L. Axial anchoring designed silicon–porphyrin sensitizers for efficient dye-sensitized solar cells *Chem. Commun.* **2013**, *49*(100), 11785-11787.
- (4) Lam, T. L.; Tong, K. C.; Yang, C.; Kwong, W. L.; Guan, X.; Li, M. De; Kar-Yan Lo, V.; Lai-Fung Chan, S.; Lee Phillips, D.; Lok, C. N.; Che, C. M. Luminescent Ruffled Iridium(III) Porphyrin Complexes Containing N-Heterocyclic Carbene Ligands: Structures, Spectroscopies and Potent Antitumor Activities under Dark and Light Irradiation Conditions. *Chem. Sci.* **2019**, *10*(1), 293-309.
- (5) Bruker AXS Inc., Madison, Wisconsin, USA.
- (6) Sheldrick, G.M. SADABS. **1996**, University of Göttingen, Germany.
- (7) Sheldrick, G.M. (2014) SHELXT—Integrated space-group and crystal-structure determination *Acta Cryst.* **2014**, *A71*, 3-8.
- (8) Sheldrick, G. M. SHELXTL Version 2014/7
- (9) Spek, A.L. PLATON SQUEEZE: a tool for the calculation of the disordered solvent contribution to the calculated structure factors *Acta Cryst.* **2015**, *C71*, 9-18.
- (10) Frisch, M.J.; Trucks, G.W.; Schlegel, H.B.; Scuseria, G.E.; Robb, M.A.; Cheeseman, J.R.; Scalmani, G.; Barone, V.; Mennucci, B.; Petersson, G.A.; Nakatsuji, H.; Caricato, M.; Li, X.; Hratchian, H.P.; Izmaylov, A.F.; Bloino, J.; Zheng, G.; Sonnenberg, J.L.; Hada, M.; Ehara, M.; Toyota, K.; Fukuda, R.; Hasegawa, J.; Ishida, M.; Nakajima, T.; Honda, Y.; Kitao, O.; Nakai, H.; Vreven, T.; Montgomery, Jr., J.A.; Peralta, J.E.; Ogliaro, F.; Bearpark, M.; Heyd, J.J.;

Brothers, E.; Kudin, K.N.; Staroverov, V.N.; Kobayashi, R.; Normand, J.; Raghavachari, K.; Rendell, A.; Burant, J.C.; Iyengar, S.S.; Tomasi, J.; Cossi, M.; Rega, N.; Millam, J.M.; Klene, M.; Knox, J.E.; Cross, J.B.; Bakken, V.; Adamo, C.; Jaramillo, J.; Gomperts, R.; Stratmann, R.E.; Yazyev, O.; Austin, A.J.; Cammi, R.; Pomelli, C.; Ochterski, J.W.; Martin, R.L.; Morokuma, K.; Zakrzewski, V.G.; Voth, G.A.; Salvador, P.; Dannenberg, J.J.; Dapprich, S.; Daniels, A.D.; Farkas, O.; Foresman, J.B.; Ortiz, J.V.; Cioslowski, J.; Fox, D.J. Gaussian, Inc., Wallingford CT, **2009**.

- (11) Spackman, M. A.; Jayatilaka, D. Hirshfeld surface analysis *CrystEngComm*, **2009**, *11*, 19-31.
- (12) Turner, M. J.; McKinnon, J. J.; Wolff, S. K.; Grimwood, D. J.; Spackman, P. R.; Jayatilaka, D.; Spackman, M. A. *CrystalExplorer17* (**2017**). University of Western Australia.



PorSil SI final.pdf (18.18 MiB)

[view on ChemRxiv](#) • [download file](#)

---